NTNU
Norwegian University of
Science and Technology

Transfer-Free and Patterned Growth of Epitaxial Graphene on Insulator

For Applications in Novel Graphene-Based

Radiation Detectors

Håkon Ivarssønn Røst

Nanotechnology
Submission date: June 2018
Supervisor: Justin Wells, IFY

Abstract

A proposed radiation detector design utilizes graphene's strong conductivity response to small changes in electric field for sensing ionization products. The transport properties of graphene has shown great potential for the improvement of sensor technology by means of so-called proximity sensing, but its wide-scale application in commercial products has so far been limited by the inability to consistently reproduce high quality graphene on insulator.

In this project a hypothesized epitaxial growth mechanism for producing monolayer graphene on silicon dioxide was investigated. Graphene was grown epitaxially under ultrahigh vacuum conditions from 6H-SiC coated with a ruthenium catalyst layer. Several different thicknesses of graphene was attempted grown using different heat treatments and thicknesses of ruthenium. The growth process was characterized using X-ray photoelectron spectroscopy (XPS), X-ray absorbtion spectroscopy (XAS) and low-energy electron diffraction (LEED).

Using energy-resolved XPS, graphene was confirmed growing in thicknesses of $2-6$ monolayers near the surface of the samples. Angle-resolved XAS revealed the orientation of the planes to be parallel to the basal plane of their underlying substrates. The XPS indicated that the growth was mediated by the ruthenium layers reacting with silicon from the carbide crystal at temperatures around $700\,°C$, with significant graphitization occurring at $800\,°C$. All samples were successfully patterned with ruthenium by evaporation through a shadow mask, and graphene was confirmed growing in the patterned regions only using spatially resolved XPS and XAS.

Decoupling of the graphene from the underlying silicides was achieved by a stepwise intercalation of silicon and oxygen, leading to the eventual formation of insulating silicon oxides between the graphene layers and the growth substrate. The presence of additional silicon oxide layers was confirmed to be in the patterned regions only using spatially resolved XPS.

Integration of the grown graphene on insulator heterostructure into the proposed radiation detector design has so far not been realized. Further mapping of the graphene band structure and testing of its transport properties is still needed to fully confirm the graphene quality, and its potential for applications in novel graphene-based electronic devices.

Samandrag

Eit føreslått nytt strålingsdetektordesign basert på grafen utnyttar materialets endring i leiingseigenskapar ovanfor svake elektriske felt til å måle ionisering. Grafens transporteigenskapar har vist seg å ha stort potensiale for å forbetre eksisterande sensorteknologi gjennom "nærleiksmålingar", men så langt har ein ikkje kunne bruke materialet i kommersielle produkt i stor skala, grunna mangelen på gode måtar å produsere grafen på isolatormateriale med jamn kvalitet.

Gjennom dette prosjektet vart ein føreslått ny vekstmekanisme for epitaksielle enkeltlag med grafen på silisiumoksid undersøkt. Grafenet vart dyrka fram under ultrahøgt vakuum på overflatane av 6H-SiC-krystallar dekte med ein ruteniumkatalysator. Det vart forsøkt å dyrke fram fleire forskjellige grafentjukkleikar ved hjelp av forskjellige varmebehandlingar og mengder katalysator. Vekstprosessen vart undersøkt med røntgenfotoelektronspektroskopi (XPS), røntgenabsorpsjonsspektroskopi (XAS) og lågenergi-elektrondiffraksjon (LEED).

Nærværet av grafen i tjukkleikane to til seks enkeltlag vart bekrefta på overflatene til dei forskjellige prøvane ved hjelp av energioppløyst røntgenfotoelektronspektroskopi. Ved hjelp av vinkeloppløyst røntgenabsorpsjonsspektroskopi vart det vist av laga låg orientert parallelt med dei underliggjande vekstsubstrata. Røntgenfotoelektronspektroskopien avslørte også at grafenveksten hadde blitt midla fram frå silisiddanning, som følgje av ein reaksjon mellom ruteniumlaga og silisium frå den underliggjande krystallen. Reaksjonen hende ved rundt 700 °C, medan betydelege mengder grafen vart fyrst danna ved rundt 800 °C. Alle prøvane i prosjektet vart mønstra med rutenium ved hjelp av deponering gjennom ei skuggemaske, og romoppløyst XPS og XAS bekrefta at grafenveksten berre føregjekk i områda der metallet hadde dekt prøvane.

Grafenet vart så fråkopla dei underliggjande silisidlaga ved å stegvis føye inn silisium og oksygen. Dette førte til slutt til danning av eit isolerande silisiumoksidlag mellom grafenet og vekstsubstratet. Romoppløyst XPS vart også her brukt til å bekrefte at oksida berre vart danna i dei mønstra delane av prøvane.

I skrivande stund har dei framdyrka heterostrukturane av grafen på isolator endå ikkje blitt nytta i det føreslåtte strålingsdetektordesignet. For å bekrefte grafenkvaliteten, og slik også potensialet for bruk i grafenbaserte elektroniske komponentar, krevst det kartlegging av materialets bandstruktur, og vidare testing av dei tilhøyrande transporteigenskapane.

Preface

This thesis concludes my five years of study at the Norwegian University of Science and Technology (NTNU). It was written as the final requirement for the Master of Science (MSc) degree in Nanotechnology at the Department of Physics. The experimental work was performed at the Australian Synchrotron facility in Spring 2018, and all the results included have been obtained there. The work was based on initial measurements performed in November 2017 at ASTRID2 in Aarhus, Denmark.

The experimental results are entirely new, but certain parts of this thesis have been inspired by or reused from the author's "specialization project" (Fall 2017). These are mainly illustrations or theory sections deemed equally applicable to the new work. Note that all figures, unless otherwise stated, have been created by the author himself.

Acknowledgements

All the experimental work, analysis and writing were performed by the the author. That being said, there are several people that have contributed to the quality of the work presented. First and foremost, I would like to thank my supervisor Assoc. Prof. Justin W. Wells. Thank you for your patience, you guidance, for letting me in on two beam times, and for sharing your indispensable knowledge and enthusiasm for surface science. Dr. Alex K. Schenk also needs to be appreciated for helping me with the data processing, and teaching me everything he knows about core level analysis. Thanks to Dr. Rajesh K. Chellappan for acquiring the beam time in Australia, and letting me step up to the challenge and run the experiments when he could not go himself. Thanks to Dr. Simon Cooil for his useful input on epitaxial graphene growth, and to Dr. Anton Tadich and Dr. Bruce Cowie for keeping the SXR endstation running smoothly throughout our experiments.

Last but not least, thank you to my family, girlfriend and close friends for supporting me throughout my time in university. Trondhjems Studentersangforening (TSS), UKEkoret Pirum and Studentersamfundet should also to be appreciated for teaching me to play as hard as I work, and for thoroughly conditioning my liver over the last five years.

Håkon Ivarssønn Røst
June 2018
Trondheim

Contents

Contents

List of Figures

List of Tables

List of Abbreviations

AES	=	Auger Electron Spectroscopy
AEY	=	Auger Electron Yield
ARPES	=	Angle-Resolved Photoemission Spectroscopy
ATP	=	Atmospheric Temperature and Pressure
BM	=	Bending Magnet
CVD	=	Chemical Vapor Deposition
DOS	=	Density of States
EM	=	Electromagnetic
EXAFS	=	Extended X-ray Absorbtion Fine Structure
FET	=	Field-Effect Transistor
FLG	=	Few-Layer Graphene
FWHM	=	Full Width at Half-Maximum
GFET	=	Graphene-Based Field-Effect Transistor
GRD	=	Graphene-Based Radiation Detector
HOPG	=	Highly Ordered Pyrolytic Graphite
ID	=	Insertion Device
IMFP	=	Inelastic Mean-Free Path
LEED	=	Low Energy Electron Diffraction
LINAC	=	Linear Accelerator
LUMO	=	Lowest Unoccupied Molecular Orbital
MO	=	Molecular Orbital
NEXAFS	=	Near Edge X-ray Absorbtion Fine Structure
NTNU	=	Norwegian University of Science and Technology
PES	=	Photoelectron Spectroscopy
PEY	=	Partial Electron Yield
PMT	=	Photomultiplier Tube
RF	=	Radio Frequency
SEXAFS	=	Surface Extended X-ray Absorbtion Fine Structure
STS	=	Scanning Tunneling Spectroscopy
SXR	=	Soft X-ray (endstation)
TEM	=	Transmission Electron Microscopy
TEY	=	Titanium Sublimation Pump
UHV	=	Ultrahigh Vacuum
UPS	=	Ultraviolet Photoelectron Spectroscopy
UV	=	Ultraviolet
VBM	=	Valence Band Maximum
VLSI	=	Very-Large-Scale Integration
XAFS	=	X-ray Absorbtion Fine Structure
XAS	=	X-ray Absorbtion Spectroscopy
XPS	=	X-ray Photoelectron Spectroscopy

1. Introduction

Accurate and efficient recording and interpretation of physical signals is of vital importance in various applications of computerized technology. From medical imaging to materials inspection or the monitoring of fission chain reactions in nuclear power plants, the application of detectors and their associated sensory systems are both widespread and diverse. In an era where sensor technology is getting increasingly complex, equally sophisticated components that can accurately record such signals are in high demand. Ideal detectors need to match both the required speed, cost, efficiency, and energy- and spatial resolution of their intended market applications. The limitations of state-of-the-art detectors in such markets have hence made researchers look towards the incorporation of new and novel materials that can help overcome these challenges.

Following the first experimental isolation of graphene in 2004 [1], a range of potential applications of the new wonder material has been eyed by fundamental researchers and technology corporations alike. An innovative new take on the well-known ionization detector suggests the integration of sheets of graphene to amplify the signal from ionization by-products by means of a proximity sensing technique [2]. The design exploits the high sensitivity of graphene on local changes in electric field, causing a drastic change in its observed conductivity. The conductivity change may in turn be translated into an electrical signal that can be related back to the by-products of incoming radiation to an absorber material. Coupled with graphene's ultra-high charge mobility and low signal-to-noise ratio [3, 4], this makes the material an excellent candidate for high-speed and high sensitivity sensing of high energy ionizing radiation like e.g. gamma radiation, alpha particles or neutrons generated by fission.

Simulations have shown that even single photon absorption of γ radiation can be detected by means of a single graphene layer [5]. The proposed design separates the graphene from the body material absorbing the incoming radiation by a dielectric layer. This capacitive structure, when biased, can fully realize graphene's potential for proximity sensing as it is not electrically coupled to the conductive absorber. However, the large-scale implementation of the design requires precise and repeatable production of high-quality single-layer graphene on insulator.

A few of the most promising techniques for growing graphene include chemical decomposition on transition metal catalysts by chemical vapor deposition (CVD), and growth on silicon carbide (SiC). The CVD method benefits from its straightforward procedure and relatively low cost level, but requires high process temperatures above $1000\,°C$ and manual transfer of graphene from the catalyst in order to place it on an insulator. Epitaxial growth forms the graphene directly on top of the SiC substrate with known crystal orientation. However, similar high temperatures to those of CVD graphene is required, and the formation of an intermediate dielectric is still needed.

In this project, a proposed synthesis route that grows graphene on 6H-SiC(0001) surfaces using a ruthenium metal catalyst is studied. Subsequently, the formation of silicon dioxide beneath the top layer of graphene is attempted to displace it from the semiconduc-

tor substrate. The hypothesized growth mechanism is expected to provide a transfer-free way of forming graphene on top of a heterostructure consisting of dielectric and semi-conductor. The next couple of chapters present the theoretical background for both the growth process, the hypothesized graphene-based radiation detector (GRD) and the relevant experimental techniques that are used to characterize the growth. The different stages of the experimental growth under ultrahigh vacuum (UHV), and the in-situ monitoring of the process using X-ray photoelectron spectroscopy (XPS), X-ray absorbtion spectroscopy (XAS) and low-energy electron diffraction (LEED) is then described. In the final two chapters, the experimental results are presented, interpreted and discussed, before the overall success of the project is evaluated and suggestions for further work is given.

2. Theory of Graphene

The different allotropes of pure carbon existing in nature all exhibit unique properties. The sp^3-hybridized and covalently bonded carbon atoms of diamond has higher hardness and thermal conductivity than any other known material [6]. Fullerene compounds, especially those made up from the spherical C$_{60}$ molecule, exhibit exotic physical properties like nonlinear optical absorption and superconductivity in the alkali-doped form [7, 8]. Carbon nanotubes can act either metallic or semiconducting simply based their layer geometry, and have a Young's modulus between 270 and 950 GPa – up to 4.5× that of steel [8, 9]. The slightly more common graphite is a soft, semi-metallic and highly anisotropic layer structure, with its properties attributed to its sheets of sixfold carbon rings in a honeycomb structure that are weakly bonded to each other by Van der Waals forces.

Graphene is a single monolayer of graphite. It first theoretical description dates back as far as 1947, but at this time it was hypothesized too thermodynamically unstable to ever be experimentally observable [10]. In 2004, Novoselov and Geim successfully demonstrated that graphene can be exfoiliated from graphite by means of scotch tape [1]. Since its experimental discovery, the properties of graphene has proven it to be nothing short of a wonder material. The atomically thin carbon film hosts extraordinary mechanical stiffness and thermal conductivity [11, 12]. This project, however, is mainly concerned with its novel electronic properties and their potential applications to highly sensitive, high-speed and low-power electronic devices. The next few sections outline the physical and electronic structure of graphene. An overview of the working principles of graphene-based radiation sensors follows, before the Chapter rounds off by summarizing some experimentally demonstrated and hypothesized methods for manufacturing graphene.

2.1. Structural Properties of Graphene

Like graphite, the carbon atoms of graphene are distributed hexagonally in a honeycomb lattice as shown in figure 2.1a. All carbon atoms are covalently bonded to three neighboring ones and are hence all sp^2-hybridized with bonds separated by angle 120°. The remaining unbound electrons from the $2p_z$ orbitals are delocalized above and below the lattice forming π and π^* bonds, respectively.

As Figure 2.1a shows, the atoms at sites A and B do not have neighboring atoms in equivalent positions[1]. Hence the honeycomb lattice is not the Bravais lattice of the structure as positions A and B are inequivalent. However the sub-lattices that separately make up the positions of the A and B sites are indeed hexagonal Bravais lattices [13]. Hence the unit cell of graphene can be described using either Bravais lattices with two basis atoms at sites A and B. The unit cell of A is shown in Figure 2.1a, with primitive translation

---

[1]Atom A will have neighbors in directions north, south east and south west, while B has its neighbors to the south, north east and north west.
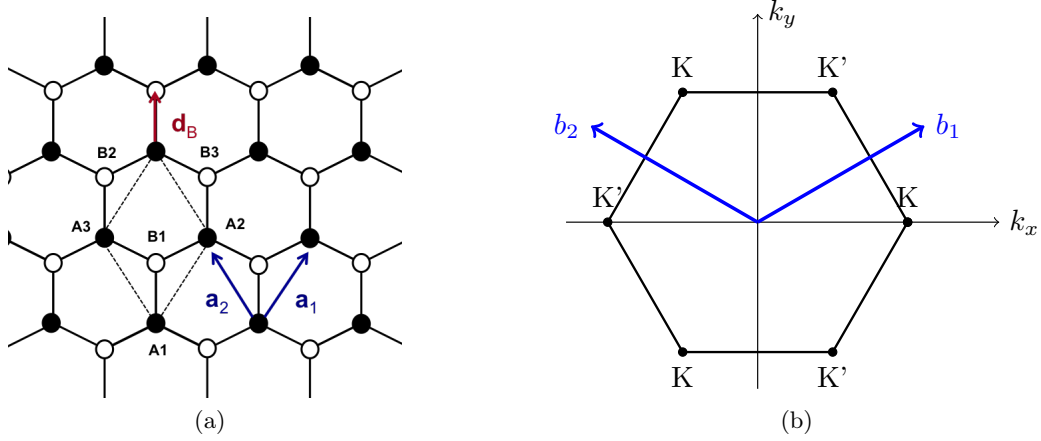
Figure 2.1.: **(a)** The primitive unit cell of graphene, described by lattice vectors $\mathbf{a}_1$ and $\mathbf{a}_2$. Each unit cell is populated with in total two carbon atoms, found at positions A and B **(b)** The first Brillouin zone of the reciprocal lattice of graphene. High symmetry points K' and K have been denoted.

vectors to the A positions given by

$$\mathbf{a}_1 = a\left(\frac{1}{2}, \frac{\sqrt{3}}{2}\right), \qquad \mathbf{a}_2 = a\left(-\frac{1}{2}, \frac{\sqrt{3}}{2}\right), \tag{2.1}$$

where $a = 2.46\,\text{Å}$ is the graphene lattice constant, and should not be confused with the magnitude of the vectors [14]. By geometry, the second carbon atom B in the unit cell is the positioned relative to A at $\mathbf{d}_B = a\left(0, \frac{\sqrt{3}}{3}\right)$ which equals a nearest neighbor spacing of $1.42\,\text{Å}$.

The reciprocal lattice for the hexagonal unit cell in Figure 2.1a is again hexagonal and rotated in-plane by 30° relative to the real space lattice. The primitive reciprocal lattice vectors are given by

$$\mathbf{b}_1 = a\left(1, \frac{\sqrt{3}}{3}\right), \qquad \mathbf{b}_2 = a\left(-1, \frac{\sqrt{3}}{3}\right). \tag{2.2}$$

Figure 2.1b shows the Brillouin zone of the honeycomb lattice together with the reciprocal lattice vectors $\mathbf{b}_1$ and $\mathbf{b}_2$. Also shown are the high symmetry points K and K' of the Brillouin zone where some of graphene's most interesting electronic behavior occurs, as will be shown in the next Section. Relative to the center point $\Gamma = 0$ of the zone, these are found at

$$K' = \frac{2\pi}{2}\left(\frac{2}{3}, 0\right), \qquad K = \frac{2\pi}{2}\left(-\frac{2}{3}, 0\right). \tag{2.3}$$

2.2. Electronic Properties of Graphene

As outlined by Grosso and Parravicini (Chpt. 6.5 on carbon-based materials in [14]), several of the basic properties of graphene can be understood from its underlying symmetry properties by means of a theoretical tight binding model. The following summarizes some of the main features of this analysis to the reader.

Derivation of Energy Dispersion Assume that the wave function of an electron for an isolated carbon atom i is ϕ_i with Hamiltonian $\hat{H}_i^0$. If this atom is placed at position A_1 in the honeycomb lattice (see Figure 2.1a), it will have three nearest neighbors[2] at $\mathbf{d}_B$, $\mathbf{d}_B - \mathbf{a}_1$ and $\mathbf{d}_B - \mathbf{a}_2$. All three will contribute to the potential felt by the electron at A_1. In the language og perturbation theory, the total Hamiltonian is

$$\hat{H}_A = \hat{H}_{A1}^0 + \hat{H}'_{A1} = \left[-\frac{\hbar^2}{2m}\nabla^2 + V(\mathbf{r}_A) \right] + \sum_{j=1}^{3} V(\mathbf{r}_A - \mathbf{d}_j), \qquad (2.4)$$

where the sum in the perturbing Hamiltonian runs over the above mentioned B positions $\mathbf{d}_j$ of the three nearest carbon atoms.

In order to determine the full wave function of the primitive unit cell, we would have to include a second atom B_1 at position $+\mathbf{d}_B$ relative to atom A_1. This atom B_1 will of course have its own Hamiltonian consisting of that of the isolated atom $\hat{H}_{B1}^0$ plus the perturbations from its three nn, being A_1 itself and the atoms at positions $\mathbf{a}_1$ and $\mathbf{a}_2$ relative to A_1. The total Hamiltonian of the unit cell is then $\hat{H}_{tot} = \hat{H}_{A1} + \hat{H}_{B1}$, and determining the energy dispersions of the bands requires solving the Schrödinger equation

$$\hat{H}_{tot}\psi_{\mathbf{k}} = \epsilon_{\mathbf{k}}\psi_{\mathbf{k}}, \qquad (2.5)$$

where $\psi_{\mathbf{k}}$ is the total wave function of the unit cell for a wave vector $\mathbf{k}$. The approach is now to construct a trial function consisting of the isolated wave functions for the electron according to the two Bravais lattices of atoms A_i and B_j. First, redefine the electron position to a global coordinate $\mathbf{r}$. If the Bravais lattice coincides with the sites of e.g. atoms A_i, the relative separation to a parent atom A_1 or B_1 in the isolated form is then $\mathbf{r}$ and $\mathbf{r} - \mathbf{d}_B$, respectively. Second, the wave function belonging to each Bravais lattice should be invariant under translation by a reciprocal lattice vector. This is satisfied if the wave functions $\psi_{\mathbf{k}}^{(A)}$ and $\psi_{\mathbf{k}}^{(B)}$ for the two Bravais lattices are described by Bloch waves. For the chosen coordinate system these are

$$\psi_{\mathbf{k}}^{(A)}(\mathbf{r}) = \frac{1}{\sqrt{N}}\sum_{\mathbf{R}_i} e^{i\mathbf{k}\cdot\mathbf{R}_i}\phi(\mathbf{r} - \mathbf{R}_j), \qquad \mathbf{R}_i = m\mathbf{a}_1 + n\mathbf{a}_2, \qquad (2.6)$$

$$\psi_{\mathbf{k}}^{(B)}(\mathbf{r}) = \frac{1}{\sqrt{N}}\sum_{\mathbf{R}_j} e^{i\mathbf{k}\cdot\mathbf{R}_j}\phi(\mathbf{r} - \mathbf{d}_B - \mathbf{R}_j), \qquad \mathbf{R}_j = m'\mathbf{a}'_1 + n'\mathbf{a}'_2, \qquad (2.7)$$

where m, n, m', n' are integers and $\mathbf{a}'_1, \mathbf{a}'_2$ are the primitive lattice vectors for the Bravais lattice of atoms B_j[3].

The proposed trial solution is a linear combination of $\psi_{\mathbf{k}}^{(A)}$ and $\psi_{\mathbf{k}}^{(B)}$ given by

$$\psi_{\mathbf{k}} = \alpha_{\mathbf{k}}\psi_{\mathbf{k}}^{(A)} + \beta_{\mathbf{k}}\psi_{\mathbf{k}}^{(B)}, \qquad (2.8)$$

where $\alpha_{\mathbf{k}}$ and $\beta_{\mathbf{k}}$ are complex functions of the wave vector $\mathbf{k}$. By time-independent perturbation theory the first order correction $\epsilon_{\mathbf{k}}^1$ to the energy is $\frac{\langle\psi_{\mathbf{k}}|\hat{H}'_A + \hat{H}'_B|\psi_{\mathbf{k}}\rangle}{\langle\psi_{\mathbf{k}}|\psi_{\mathbf{k}}\rangle}$ [15].

---

[2]from hereon denoted by "nn".

[3]These can be described using the lattice vectors of A_i by adding the offset $\mathbf{d}_B$: $\mathbf{a}'_1 = \mathbf{a}_1 + \mathbf{d}_B$ and $\mathbf{a}'_2 = \mathbf{a}_2 + \mathbf{d}_B$.

Plugging in equation 2.8 for $\psi_{\mathbf{k}}$ containing the two Bloch waves gives the matrix equation

$$\begin{pmatrix} H_{AA} & H_{AB} \\ H_{BA} & H_{BB} \end{pmatrix} \begin{pmatrix} \alpha \\ \beta \end{pmatrix} = \epsilon_{\mathbf{k}}^1 \begin{pmatrix} M_{AA} & M_{AB} \\ M_{BA} & M_{BB,} \end{pmatrix} \tag{2.9}$$

where $H_{ij} = \langle \psi_{\mathbf{k}}^{(i)} | \hat{H}' | \psi_{\mathbf{k}}^{(j)} \rangle$ are the elements of the perturbation matrix and elements $M_{ij} = \langle \psi_{\mathbf{k}}^{(i)} | \psi_{\mathbf{k}}^{(j)} \rangle$ represent the inner product of the overlap between wave functions $\psi_{\mathbf{k}}^{(i)}$ and $\psi_{\mathbf{k}}^{(j)}$. A non-trivial solution to this one requires non-zero weights α and β, or

$$\det[\mathcal{H} - \epsilon_{\mathbf{k}}^1 \mathcal{M}] = \begin{vmatrix} \epsilon_A - \epsilon_{\mathbf{k}}^1 & (H_{AB} - M_{AB}) \\ (H_{BA} - M_{BA}) & \epsilon_B - \epsilon_{\mathbf{k}}^1 \end{vmatrix} = 0. \tag{2.10}$$

Notice how only considering interactions from nn in H'_{ij} reduces matrix terms H_{AA} and H_{BB} to the perturbation energies ϵ_A and ϵ_B, respectively[4]. The inner product of normalized wave functions with itself is one, so $M_{ii} = \langle \psi^{(i)} | \psi^{(i)} \rangle = 1$.

From hereon, only the perturbations in orbitals $2p_z$ are considered, i.e. the contributions from orbitals $2s$, $2p_x$ and $2p_y$ are ignored in both $\psi_{\mathbf{k}}^{(A)}$, $\psi_{\mathbf{k}}^{(B)}$ and the total energy perturbation[5]. The off-diagonal element H_{AB} can be shown to equal

$$H_{AB} = -\gamma_0 F(\mathbf{k}) = -\gamma_0 \sum_{j=0} e^{i\mathbf{k}\cdot\mathbf{a}_j} = -\gamma_0 \left[1 + 2 \cos \frac{k_x a}{2} \exp\left(-i\frac{\sqrt{3}k_y a}{2} \right) \right], \tag{2.11}$$

where $\mathbf{a}_0 = 0$ is the position of the atom A_1 and the sum runs over the two primitive lattice vectors $\mathbf{a}_1$ and $\mathbf{a}_2$ since A_1's nearest neighbors are located at $\mathbf{d}_B - \mathbf{a}_1$ and $\mathbf{d}_B - \mathbf{a}_2$. the constant γ_0, called the inter-atomic matrix element, contains the inner product from H_{AB} given by $\langle \psi_{\mathbf{k}}^{(A)} | \hat{H}' | \psi_{\mathbf{k}}^{(B)} \rangle$. Similarly, M_{AB} can be written as $s_0 F(\mathbf{k})$, with s_0 denoting the inner product contribution from the overlap between $\psi_{\mathbf{k}}^{(A)}$ and $\psi_{\mathbf{k}}^{(B)}$. The remaining two matrix elements becomes $H_{BA} = -\gamma_0 F^*(\mathbf{k})$ and $M_{BA} = s_0 F^*(\mathbf{k})$. Plugging these into the secular equation 2.10 and solving for $\epsilon_{\mathbf{k}}^1$ yields

$$\epsilon^1(\mathbf{k}) = \frac{\epsilon_{2p} \pm \gamma_0 |F(\mathbf{k})|}{1 \mp s_0 |F(\mathbf{k})|}. \tag{2.12}$$

Here, $\epsilon_A = \epsilon_B$ have been renamed ϵ_{2p} to describe the constant energy offset from sp^2 hybridization and bonding seen by all atoms A_i and B_j. The assumption $s_0 \ll 1$ seems reasonable from the expected overlap of the wave functions from atoms A_i and B_j [13], and γ_0 is estimated numerically to $\sim 3\,\text{eV}$ [14]. A plot of the dispersion in eq. 2.12 with values $\gamma_0 = 3.033\,\text{eV}$, $s_0 = 0.129$, $a = 2.46\,\text{Å}$ and constant offset $\epsilon_{2p} = 0$ has been reproduced from literature [16], and is shown in Figure 2.2a. The expression has some quite extraordinary implications for the charge transport properties in the material, and will be discussed next.

---

[4]By symmetry arguments, these two should be equal.

[5]The reason for this is that these orbitals hybridize to form the σ bands involved in the bonding of carbon atoms to each other in the lateral plane. In terms of charge transport, which is the main concern in this project, these states are all occupied and do not contribute any states to the conduction band. However, the strong σ bonds are responsible for keeping the sturdy C-C bond construction together, leaving the unbound electrons in the π and π^* to migrate upon excitation [14].

Transport Properties near High Symmetry Points The phase factor $F(\mathbf{k})$ in eq. 2.12 show some interesting properties. The phase contribution is maximum at the Γ point where $\mathbf{k} = 0$. Moving to any of the six high symmetry points K' or K reveals a vanishing phase contribution to the dispersion, leaving only the constant offset ϵ_{2p} at the corners of the two-dimensional Brillouin zone. From eq. 2.12 this means the π and π^* bands are degenerate with zero bandgap at the high symmetry points. Graphene is hence a zero band gap material, or a semi-metal.

Near the neutrality points, the dispersion provided by the phase factor can be expanded as a first order Taylor series in the wave vector $\mathbf{k}'$ measured from K' or K [14]. The perturbation Hamiltonian then takes the form

$$\begin{vmatrix} 0 & v_F[\hbar k_x' - i\hbar k_y'] \\ v_F[\hbar k_x' + i\hbar k_y'] & 0 \end{vmatrix} = 0, \qquad v_F = \frac{\sqrt{3}}{2}\frac{a|\gamma_0|}{\hbar}, \tag{2.13}$$

where, v_F is the Fermi velocity of carbon, measured to be $\sim 1 \times 10^6 \ \mathrm{m\,s^{-1}}$ [17]. The dispersion in the expansion can be written

$$\epsilon(\mathbf{k}') = \pm\hbar|\mathbf{k}'|, \quad k = \sqrt{k_x^2 + k_y^2}, \tag{2.14}$$

taking a conical shape that is often referred to as a *Dirac cone*. This shape deviates from the usual parabolic dispersion observed for semiconductors near the boundary of the first Brillouin zone. Comparing the energy dispersion to the relativistic energy of particles given by $E = \sqrt{m^2c^4 + p^2c^2}$, and remembering the the other energy contributions are constant offsets, a linear behavior as proposed can only be achieved if the electrons carry *zero rest mass m*. This means electrons near the high symmetry points behave as relativistic particles according to the Dirac equation. The locations K' and K are hence often referred to as *Dirac points* in the Brillouin zone.

The relativistic behavior of electrons near the Dirac points is at the heart of several striking phenomena in the material like observed Klein tunneling and quantum Hall effect [18]. Graphene also exhibits extraordinary electron mobility: mobilities of $200\,000 \ \mathrm{cm^2\,V^{-1}\,s^{-1}}$ and $11\,000 \ \mathrm{cm^2\,V^{-1}\,s^{-1}}$ have been reported for suspended graphene and epitaxially grown graphene on 4H-SiC, respectively [19, 20]. This can be partially explained from the zero rest mass, but also little scattering with optical phonons at room temperature compared to what is observed in conventional semiconductor materials like GaAs [21].

The final property that will be discussed is the sensitivity of graphene mobility to the presence of an external electric field. Figure 2.2b shows a simplified model of the occupied states in the band structure of graphene near a Dirac point. The Fermi level, illustrated by the opaque gray disk, lies exactly at the neutrality point where the two bands meet. The density of states $\rho(E_F)$ at the Fermi level is hence zero, and all states in the valence band below are occupied with electrons (green). Applying an external potential $V(\mathbf{r})$ will shift the energies of the band by energy $\Delta E = -eV(\mathbf{r})$ relative to the Fermi energy, and this has profound effects on the filling of available energy states, as the Figure shows. For a positive potential the Fermi level of the perturbed bands is now situated inside the upper band, much like what is seen for metallic compounds [22]. A multitude of unoccupied energy states are available for the electrons with minuscule energy separation δE from the Fermi level, so electrons will be readily excited from thermal energy $\sim k_B T$ even at low temperatures. This has profound impact on the charge carrier concentration
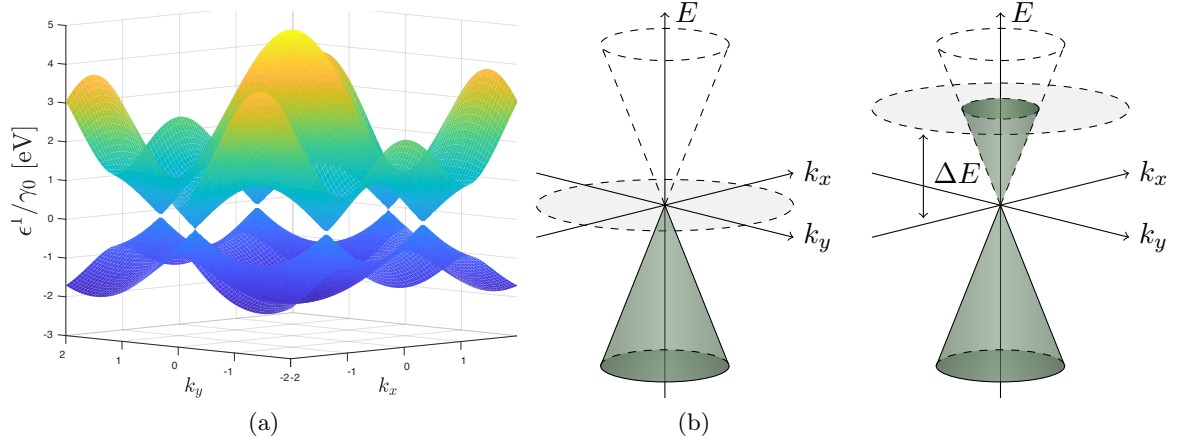
Figure 2.2.: **(a)** Band structure of graphene calculated according to eq. 2.12. The two bands meet at six degenerate points K' and K, called *Dirac points*, at the corners of the hexagonal Brillouin zone **(b)** A simplified figure showing how the occupied density of near a Dirac point changes with an external electric field. The bias shifts the bands relative to the Fermi level E_F (gray disk) by ΔE, enabling the electrons near E_F to be excited into the unoccupied states of the upper band.

of electrons n, which has demonstrated values up to $\sim 10^{13} \text{cm}^{-2}$ [1]. This again will have great impact also the conductivity of the material, given by

$$\sigma = e[n\mu_e + p\mu_h] \approx en\mu_e, \tag{2.15}$$

where e is elementary charge, and n, μ_e, p, μ_h are the carrier density and mobility of electrons and holes, respectively. The measured resistivity $\rho = 1/\sigma$ changes by several kΩ as the external voltage V_g is increased to $100\,\text{V}$, even for temperatures as low as $T = 70\,\text{K}$ [1]. The effect is observable also for negative potentials relative to the graphene, where the energy bands are shifted upwards relative to the Fermi level. Electrons can now occupy the vacant energy states up to the Dirac point, generating holes in the valence band that enable hole conductivity. Equation 2.15 will then be dominated by hole carriers p instead of electrons.

This pronounced *ambipolar field effect* means the majority carriers of graphene can be tuned with the sign of the applied potential. An associated sign change can also be seen in the Hall coefficient R_H around zero potential, with the conductivity vs. voltage curve is roughly symmetric around the zero potential point (see Figure 2.3a). This abrupt change in conductivity with changes in external bias is the property field-effect transistors (FETs) and radiation sensors based on graphene seek to exploit.

2.3. Working Principles of Graphene-Based Radiation Sensors

The previous Section reviewed some of the novel properties of graphene, with an emphasis on its band structure and electronic transport behavior. This Section applies the insight to the proposed design of graphene-based radiation sensors, seeking to elaborate on how graphene can help improve performance compared to current state-of-the-art sensors available on the market. Following the text on radiation detection by Knoll [23], a quick review of how current sensors work, along with their main advantages and disadvantages is first given to ease the comparison with graphene-based devices.

Conventional Detector Designs   Most current state-of-the-art detectors are either *Ionization-based detectors* or *Scintillator detector*. Both seek to measure and quantify the by-products of an incoming radiation composed of particles or electromagnetic waves.
Ionization detectors consist of a so-called active medium, usually a gas mixture, in the presence of an external electric field from an opposing anode and cathode. Incoming radiation ionizes the atoms of the active medium, allowing charge carriers to drift in the potential towards either electrode. The current of this charge drift is hence measured to quantify the ionization process. Its signal strength will be dependent on the applied voltage, which governs whether only initial ionization products or by-products from avalanche multiplication reach the detector. Ionization detectors benefit from their simple design and working principle, allowing the detection of any radiation that can cause ionization of the active medium. The type of radiation detected can hence be tuned by the composition of the active volume. Their main disadvantage is that they rely on the drift of carriers from the active volume to the detector, limiting their response speed and causing significant dead time between detectable events. Ionization detectors are widely used to detect particle radiation such as alpha particles or neutrons.

Scintillator detectors detect ionizing radiation by the light emitted from exciting a *scintillator material*. The scintillator, usually an inorganic crystal or an organic liquid or plastic, emits photons upon de-excitation that are characteristic in terms of intensity and wavelength to the incoming radiation. This light is then captured by a detector to determine the type, energy and intensity of the radiation sensed by the scintillator. Good scintillators should convert the energy of the incoming radiation to detectable light with high efficiency, and be transparent to the wavelength(s) of its own emitted light from de-excitation to allow minimal signal attenuation and hence good light collection. The most commonly used detector is the photomultiplier tube (PMT). Scintillator detection has the advantage of higher operating speeds and less dead time compared to ionization detectors, but are also less suitable for the detection of neutrons.

Graphene-Based Radiation Detector   The graphene-based radiation detector (GRD) is a modification of the ionization detector, with proposed differences that seek to reduce or eliminate the shortcomings of the original design and sensing mechanism. Originally proposed by Foxe *et al.* [5], the design utilizes the abrupt changes in graphene conductivity with local electric field (explained in section 2.2) to detect ionization products from the incoming radiation. Figure 2.3b illustrates the suggested sensor design. The bulk component is a heterostructure consisting of an atomically thin graphene layer, placed on

an insulating buffer layer and coupled to a semiconductor absorber material. A minimum of four metal electrodes contact the graphene: a set of source and drain to run a current through the conductive sheet material, and at least two contacts to measure the voltage drop across the device. A voltage V_G is applied between the back gate of the absorber and one of the mentioned electrodes to tune the conductivity of the channel. The simple structure resembles a graphene-based field-effect transistor (GFET) with the graphene acting as the source-drain channel, the absorber body as the gate electrode and the insulator as the gate dielectric.

The slightly different GRD aims to *indirectly* sense ionization products in the absorber from the induced change in electric field through the heterostructure by the charge carrier generation. Incoming radiation interacting with the absorber will generate electron-hole pairs that drift across the structure in the presence of the electric field from V_G. Depending on the gate polarity, either electrons or holes will accumulate at the semiconductor-dielectric interface. The presence of additional charges will alter the local electric field in proximity to the graphene, shifting its energy states relative to the Fermi level E_F. This leads to an induced charge carrier density, which for electrons is

$$n = \frac{\epsilon_0 \epsilon_r V_G}{et},$$
(2.16)

where ϵ_0 is the vacuum permittivity, ϵ_r is the relative permittivity of the dielectric, t is its thickness and e is elementary charge [1]. The same is of course true for hole carriers as well, by flipping the polarity of V_G and substituting p for n as the majority charge carrier concentration.

The energy resolution of a detector is ultimately set by its noise level, which determines what magnitude of signal can be distinguished from the background. This sensor configuration, where sensing of the additional charge carriers is by proximity field effects instead the ionization product reaching the cathode/anode, is hypothesized to work for even single event radiation detection [5]. This is backed by graphene's exceptionally low noise characteristics that has allowed even the detection of single atom adsorption for chemical detectors [4]. Together with the earlier mentioned sensitivity to minuscule changes in electric field, the graphene layer can hence function as a high-gain preamplifier of the fluctuations in electric potential by the generated ionization products.

Like with the ionization detector, the type of radiation detected is dependent on the absorber medium, and can hence be selected by changing the type of semiconductor used. The proposed design uses undoped semiconductor absorbers to increase the relative change in electric field detected from each interaction event compared to a medium with higher charge carrier density. The field lines from the applied bias V_G serves the purpose of funneling the ionization products in the absorber to the region directly underneath the graphene. From equation 2.16 this not only increases the detected signal from each charge, it also makes the field response independent on where in the absorber the ionized charges where produced. Hence the change in graphene conductivity will be dependent only on the amount of charge produced, seeking to sense all energy dissipation from the incoming radiation [5].

Finally, GRD have the potential of high-speed operation far exceeding its conventional semiconductor counterparts. Dual-gated GFETs have been shown to exhibit cutoff frequencies up to 300 GHz [24, 25]. However, their predicted superiority and widespread application to sensor systems has so far been limited by the difficulties of manufacturing

(a)   (b)
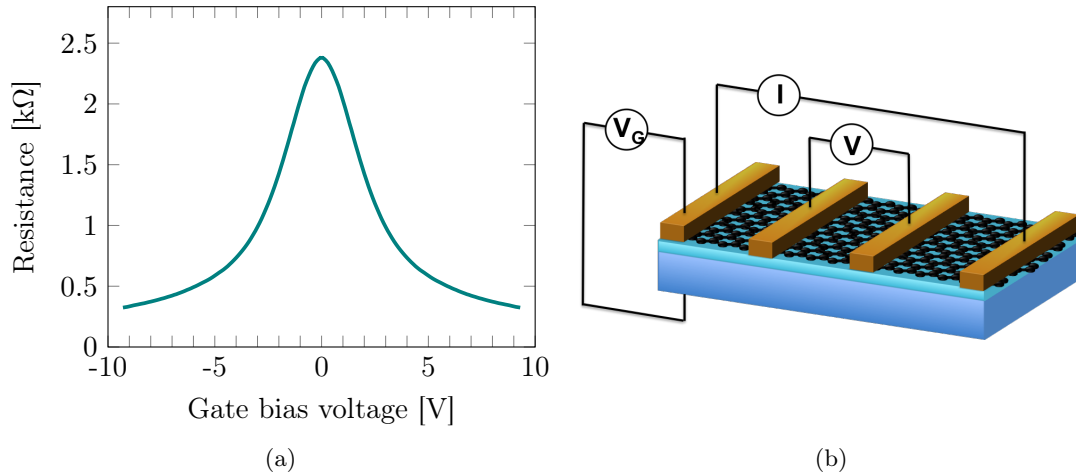
Figure 2.3.: **(a)** A sketch showing the typical resistance vs. applied bias voltage behavior for monolayer graphene. The ambipolar nature of the graphene is evident from its roughly symmetric decay in observed resistance for both positive and negative gate voltages relative to the zero point. Based on experimental data from a heterostructure of graphene sandwiched between two layers of hexagonal boron nitride (hBN), as recorded by Øystein Dahl. Reproduced and adapted with permission. **(b)** A schematic of the proposed graphene-based radiation detector (GRD) design. The body of the device is a heterostructure of undoped semiconductor (bottom) and single-layer graphene (top) separated by a dielectric layer. A bias voltage V_G is supplied between the absorber body and the graphene layer to drift ionization charges in the absorber towards the dielectric interface. A current I is run through the graphene, and the voltage drop along the channel V is measured to determine the resistivity of the graphene that fluctuates with the electric field from the ionization charges.

pristine single-layer graphene on insulator with excellent quality and repeatability. The next section discusses some widely used methods for graphene growth and heterostructure formation with insulator materials, along with a new method hypothesized to overcome the difficulties of graphene transfer. The latter is at the heart of this project, and its proposed manufacturing steps will thus be discussed in detail.

2.4. Fabrication of Graphene on Insulator

The first isolation of graphene experimentally by Novoselov and Geim in 2004 [1] sparked more than heavy research into the properties of the new and stellar 2D material alone. Along with the unveiling of its unique features and promising applications in electronics followed an extensive area of research related to the production of high quality sheets of graphene.

To realize its full potential as a low-noise, high-mobility 2D conductor, graphene needs to be placed on a relatively poor conductor or insulator. This is to allow any charge transfer by the structure mainly through the graphene layer, so that the current-carrying system is effectively 2D and exhibits sheet conductivity. Running current through a het-

erostructure of graphene on any reasonable conductor will cause 3D conductivity, where the noise level and transfer properties of the system are set by both materials. Hence the potential benefits of using graphene cannot be fully exploited. The first probing of graphene's electronic properties was therefore done by exfoliating the material mechanically from graphite and placing it on a layer of SiO_2. Today, this is still the benchmark method for producing high quality graphene in terms of electrical performance. However, the crystallites produced are limited to a size of $< 1\,mm$, and their size and orientation upon exfoiliation and transfer will vary. This makes the method less suitable for large-scale production in device fabrication [3].

A second and commonly employed technique is to grow graphene from gaseous hydrocarbons on a catalyst metal in chemical vapor deposition (CVD). Typically, a gas mixture of H_2 and CH_4, C_2H_6 or C_3H_8 is flowed through a quartz tube at $\sim 1000\,°C$ over a single crystal surface of Cu^6 that promotes de-hydrogenation of the gas and deposition of carbon onto the catalyst [3]. Since the decomposition is triggered by the catalytic properties of the metal surface, the reaction terminates upon the formation of a single sp^2-hybridized carbon layer. The target is then subsequently removed, either by chemical decomposition [27] or evaporation [28].
CVD-grown graphene benefits from its straightforward and inexpensive production method. The size of the graphene sheet produced is determined by the size of the catalyst surface, and can hence be large compared to what is achievable by exfoiliation. Bae *et al.* have demonstrated production of 30" graphene sheets using the CVD method [27]. By keeping the number of nucleation sites low, grain sizes of $\sim 5\,mm$ can be routinely achieved [29]. Despite its apparent advantages, CVD graphene like the exfoliated form suffers from needing to be manually transferred onto an insulating substrate following its formation on the catalyst. Contamination from the catalyst can also degrade the performance of the graphene after removal. Finally, the high process temperature makes CVD growth of graphene incompatible with many runs in very-large-scale integration (VLSI) for integrated circuit manufacturing like e.g. the CMOS process. These usually incorporate Al for wiring, which melts at $660\,°C$ [30].

A third option that seeks to overcome the setbacks of the transfer process is to grow graphene epitaxially from a carbon-rich substrate. An extensively studied synthesis route is the thermal decomposition of SiC, which offers the possibility to grow homogeneous layers of high quality graphene directly on top of the underlying semiconductor crystal [31]. The material, consisting of tetragonally bonded Si to C in stochiometrically equal amounts, exists in various polymorphs where particularly one stacking sequence offers high quality crystallinity. The most common forms employed are 3C-SiC, 4H-SiC and 6H-SiC, where C and H stand for cubic and hexagonal, respectively, and the number indicates the amount of tetragons stacked within one unit cell [32]. The structure of 6H-SiC is shown in Figure 2.4.
The synthesis of graphene on SiC is achieved by thermally decomposing the crystal in vacuum or under atmospheric pressure. Heating a sample to $\sim 1400\,°C$ triggers sublimation of the Si atoms, leaving behind carbon on the surface that rearranges into graphitic layers [3]. When grown on the Si face (0001) of either 4H-SiC or 6H-SiC, a non-conducting and complex interfacial layer of orientation $(6\sqrt{3} \times 6\sqrt{3})R30°$ is formed between the graphitic layers and the SiC [33]. The layer is partially bonded to the underlying substrate and

---

[6]The effect has also been demonstrated for other catalyst metals such as Pt, Ni Ru and Au [26].
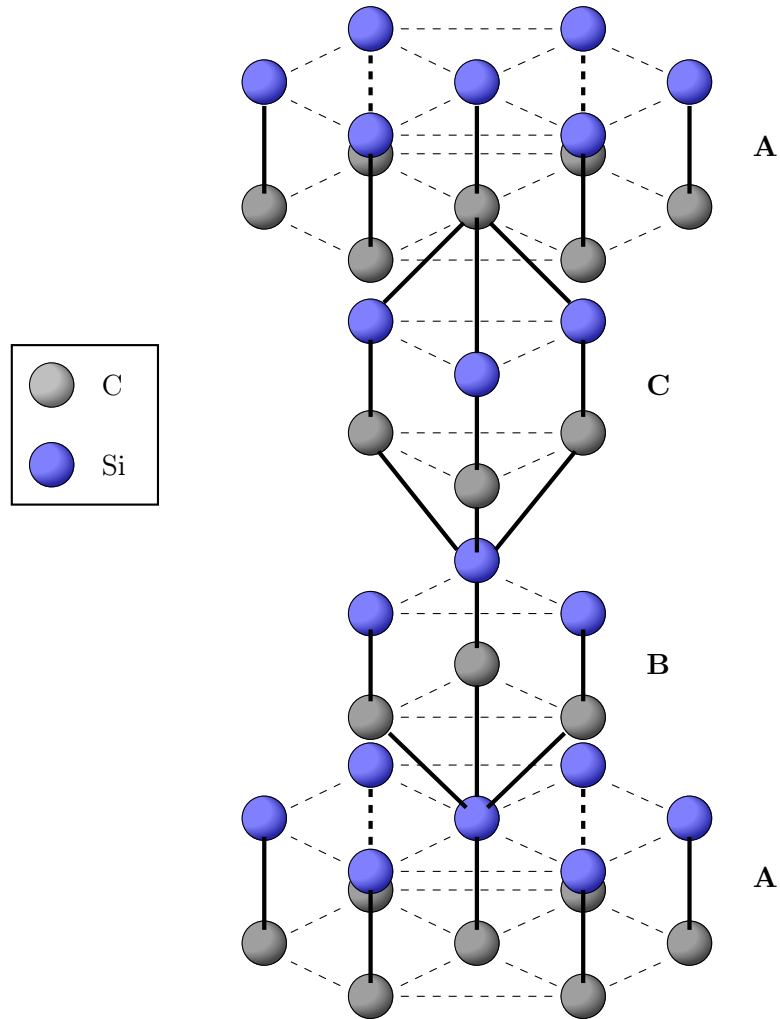
Figure 2.4.: A schematic of the first four layers of Si-C tetrahedrons in the 6H-SiC structure. The complete unit cell of the polymorph contains in total six layers stacked in sequence ABCACB.

does hence not behave like graphene. However, it provides a orientation template for the growth of the subsequent graphitic layers and a non-interacting interface. A monolayer of graphene grown on this buffer layer covalently bonded to SiC(0001) should then in principle behave like a free-standing graphene layer [3, 34]. Although it eliminates the need to transfer graphene onto an insulating layer, graphene growth from thermal decomposition of SiC is a delicate process that requires stringent control of processing parameters and the anneal time to grow an accurate number of layers [35]. Furthermore, the high processing temperature is both impractical and incompatible with VLSI processes as mentioned for the CVD growth method.

Mediated Growth from SiC with a Metal Catalyst Several sources have reported mediated growth of graphene on SiC using a catalyst metal [36–40]. This approach relies on the reaction of Si with the metal layer upon heating rather than sublimation to trigger the re-hybridization of carbon into the sp^2 from. The reaction can be summarized as

$$\text{SiC} \quad + \quad \text{M} \quad \xrightarrow{\Delta H} \quad \text{M}_x\text{Si}_y \quad + \quad \text{C}_{\text{gra}}, \tag{2.17}$$

where M is the particular metal catalyst used, ΔH is heat and x and y are stoichiometric coefficients. Equation 2.17 shows how the reaction involves the formation of an interlayer silicide between the graphene and the underlying SiC substrate. The heat is supplied to the sample either in vacuum or under atmospheric conditions, depending on the catalyst employed.

The reported mediated growth processes all hold the benefit of being able to graphitize bulk carbon at temperatures lower than 1000 °C. The iron-mediated growth by Cooil *et al.* [36] is particularly interesting, where graphene formation is shown at temperatures as low as 600 °C. This makes it compatible with conventional VLSI processes, and furthermore precise control over the thickness of graphene formed may be provided if the stoichiometry of the silicide is known. However, this stoichiometry has not been fully understood for the relevant catalyst metals. For high ratios of metal this leaves the possibility that the interlayer formed will be partly conductive. That case would render any conduction through the graphene irrelevant. In comparison, both exfoliated and CVD grown graphene hold the benefit of choosing the desired insulating substrate compared to the mediated growth mechanism.

Mediated Growth with Interlayer Oxide Formation A particularly interesting study by Lizzit *et al.* shows that graphene present on a silicide layer with transition metal ruthenium can be isolated by means of oxygen intercalation [41]. Annealing the Ru_xSi_y + C_{gra} heterostructure under a partial pressure of oxygen at temperature $T = 640\,\text{K}$ allows O_2 to intercalate below the graphene layer, where it subsequently reacts with the Si atoms in the silicide layer and displaces the Ru atoms. The result is a controlled growth of SiO_2 dielectric limited by the amount of Si present that lifts the graphene layer from the underlying substrate.

In the experiment graphene is first grown by CVD onto a ruthenium catalyst surface. It is then exposed to gaseous Si at $T = 720\,\text{K}$ that intercalates under the graphene layer and forms the ruthenium silicide layer before the final exposure to oxygen. This method holds several major advantages. The first CVD step allows graphene to be grown precisely with an orientation determined by the crystal structure of the Ru surface. More importantly, it allows the graphene to rest on a dielectric formed from the underlying structure in the final step, eliminating the need of manual transfer to a separate dielectric. Hence the final structure exhibits freestanding graphene of potentially pristine quality with known orientation resting on an insulating layer. However, for the sake designing a GRD as described in Section 2.3, the structure lacks the crucial component of an absorber body beneath the dielectric.

The proposed growth mechanism in this project combines the metal-mediated growth from SiC with the oxygen intercalation step demonstrated by Lizzit *et al.* and is shown in Figure 2.5. Ruthenium is used as the metal catalyst, having demonstrated silicide formation at temperatures $800 - 900$°C and evident signs of graphitization at ~ 1000 °C
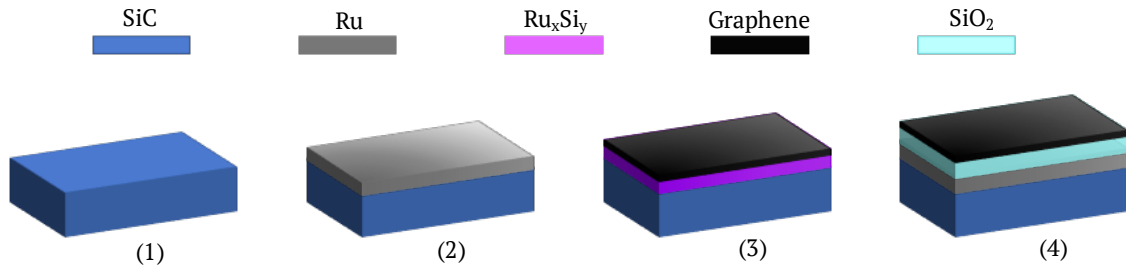
Figure 2.5.: A proposed growth mechanism for the formation of graphene on insulator. The mechanism combines the metal-mediated graphene growth reported by Cooil *et al.* with the intercalation of silicon and subsequently oxygen under the carbonic top layers reported by Lizzit *et al.* [36, 41]. This is expected to oxidize any silicon-rich layers and hence electrically decouple the graphene from the underlying substrate.

[40, 42]. Although ruthenium does not hold the same benefit of lower temperature silicide formation as iron [36], its silicide is known to demonstrate the desired displacement of graphene from reaction with oxygen [41]. Furthermore, it is hypothesized that signs of silicide formation and graphitization may be visible at lower temperatures if the resolution in the probing experiment is optimized. The next Chapter describes among else the principles of photoemission and how it can be used to study the chemical reactions occurring near the surface of a sample, making it a highly suitable technique for investigating silicide formation and the growth of graphene layers.

3. Techniques and Apparatus

3.1. Theory Behind Experimental Techniques

The first half of this Chapter explains the working principles and theory behind the characterization techniques that are used to study graphene in this project. It starts out with a discussion of the various forms of *photoemission spectroscopy* (PES), then proceeds to an explanation of *X-ray absorption spectroscopy* (XAS) and finally *low energy electron diffraction* (LEED). Interpretation and processing of data obtained by either techniques are explained accordingly.

The second half of the Chapter starts out by explaining how electromagnetic (EM) radiation can be generated for use in photoemission and X-ray absorption spectroscopy. The chapter ends by stating the importance of working under vacuum to achieve clean and controlled epitaxial growth. Relevant measures of cleanliness in vacuum and the most common apparatus used to achieve this is also included.

3.1.1. Photoemission Spectroscopy

In 1905, Albert Einstein published his famous paper in *Annalen der Physik* explaining the phenomenon known as the photoelectric effect by the quantization if light into discrete energy packets [43]. His main discovery, which later awarded him the Nobel Prize in Physics in 1921, was that incident electromagnetic radiation on a sample emits electrons of maximum kinetic energy

$$E_K = h\nu - \phi_S. \tag{3.1}$$

Here, $h\nu$ is the discrete photon energy of the incoming radiation, and ϕ_S is the energy barrier electrons need to overcome at the surface to escape the material, known as the material *work function*. Einstein's discovery formed the basis of the early work of quantum mechanics and the theoretical formulation of particle interaction, which today is at the center point of our understanding of how solid state materials behave. The techniques of photoemission spectroscopy utilizes the photoelectric effect to excite electrons from the surface layers of materials by irradiation of light with various wavelengths. The emitted electrons are in turn detected to probe the occupied electronic states in the material. The variety of information available from the photoemission process has made PES techniques a standard tool in surface science.

Technique Overview

PES can be used to determine the compositional structure and chemical states present in the uppermost layers of a sample. This in turn allows the user to characterize ongoing chemical reactions and the electronic band structure of the material.

In a typical PES experiment, the sample is irradiated with a precise wavelength of

monochromatic light to excite bound electrons through the sample surface. Note that the escaping electrons will not all carry the same kinetic energy, as eq. 3.1 suggests. Prior to excitation, the electrons exist in different atomic orbitals, bound by different potential energies to their parent nuclei, carrying different amounts of angular momentum and energy perturbations from bonding and the atomic fine structure. This translates to the different electrons holding different *binding energies* E_B, which changes the their observed kinetic energy in vacuum upon photoexcitation in eq. 3.1 into

$$E_K = h\nu - E_B - \phi_S. \tag{3.2}$$

The stated binding energy E_B is referenced to the Fermi level of the parent atomic specie. Characterization of a sample's electronic structure can hence be done by measuring the kinetic energy E_K of the excited photoelectrons. This is normally done by an electron analyzer of work function ϕ_A, placed in electrical contact to the sample at common ground potential. Connecting the two causes their Fermi levels to align, inducing an offset contact potential of $\phi_S - \phi_A$ to the measured kinetic energy of the photoelectrons

$$\begin{aligned} E_K &= h\nu - E_B - \phi_S + (\phi_S - \phi_A) \\ &= h\nu - E_B - \phi_A. \end{aligned} \tag{3.3}$$

Hence the kinetic energy of the incoming photoelectrons is measured relative to the vacuum level of the analyzer. The analyzer work function has to be known to correctly calibrate the binding energy scale of the received signal [44]. The detection of photoelectrons in PES experiments is illustrated in Figure 3.1. Notice from eq. 3.3 that a measurable photoemission signal from a given energy level will only be received if $h\nu > (E_B - \phi_A)$. Thus radiation of different photon energies is needed to generate a measurable signal from different atomic orbitals. The most common techniques employ either ultraviolet light or soft to hard X-rays to access the high energy electrons in the valence band, or high binding energy electrons in the inner shells, respectively. X-ray photoelectron spectroscopy (XPS) is perhaps the most common, where the sharply defined and highly characteristic core level energies are used as fingerprints for the elements present in their various perturbed forms. Ultraviolet photoelectron spectroscopy (UPS) obtains its information from the low binding energy electrons in the valance band, and is suitable for resolving the lateral dispersion of electron band structure.

Finally, note that despite the deep penetration depth of light in matter, PES techniques are all highly surface sensitive due to the strong interaction of electrons with matter. The inelastic scattering of photoelectrons leaving the material will be discussed later in the chapter.

The Photoemission Process

Various theoretical models with different levels of complexity have been developed in an attempt to describe the photoemission process[1]. The simplest and most commonly applied model to solid materials is outlined by Hüfner [46], who summarizes photoemission in three distinct steps:

---

[1]A detailed outline of the most common approaces can be found in the review article by Damascelli [45].
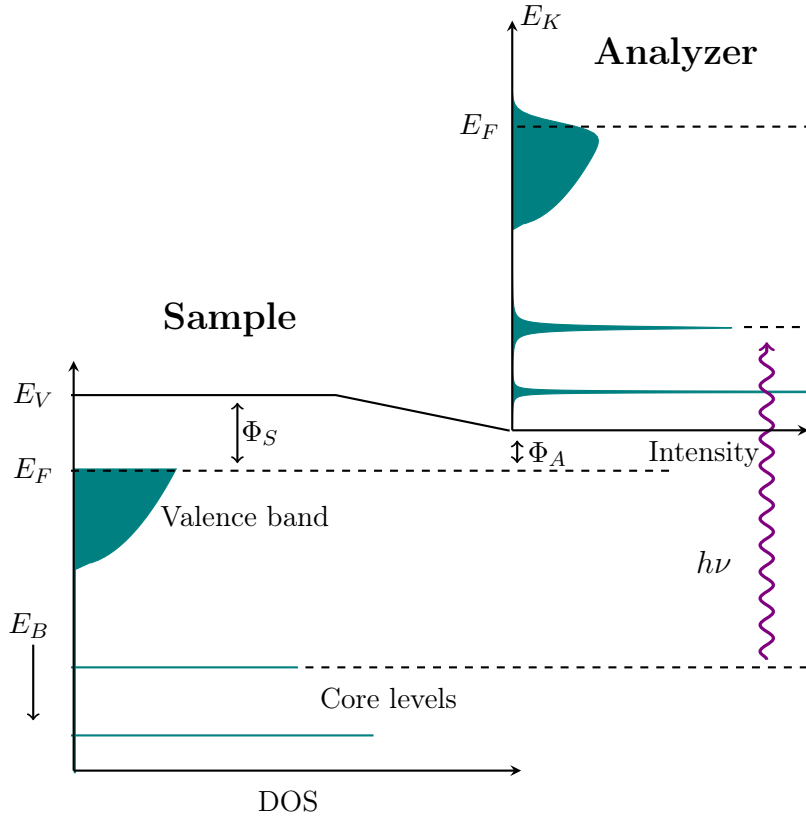
Figure 3.1.: Energy diagram for the photoemission process and signal detection. Electrons from either the core levels or valence band of a sample get excited by incoming photons of energy $h\nu$, and appear as broadened core level peaks or a Fermi-Dirac modulated density of states plot in the observed spectrum. The electrical contact between the energy detector and sample align their Fermi levels, so that the detected kinetic energy of the photoelectrons are described by eq. 3.3.

1. A photon is absorbed by an atom, exciting an electron and freeing it from its initial bound state

2. The delocalized electron travels through the sample towards the surface

3. The electron escapes through the surface into vacuum

Hüfner's model is conceptually simple, but oversimplifies the underlying physics from a quantum mechanical point of view. It is argued that treating all three steps as one gives a more accurate description of the photoemission process [45, 46]. However, the division into three separate parts can still be justified reasonably well, and holds the benefit of of being conceptually simpler than the *one-step model*. Hence the three-step model will be outlined here.

The first step involves the excitation of an electron from an (occupied) initial state to a free final state by the incoming radiation, i.e. a time-dependent electromagnetic field $\mathcal{E}(t)$. Assuming a small field strength $\mathcal{E}_0$ and negligible spatial variation across the atom, the

situation can be treated by time-dependent perturbation theory [47]. The rate at which electrons transition from an initial state $|\psi_i\rangle$ of binding energy E_B to an unoccupied final state $|\psi_f\rangle$ of energy $E_f = \hbar\omega - E_B$ is then given by *Fermi's golden rule* [47, 48]:

$$dW(E_B, \hbar\omega) = \frac{dP(E_B, \hbar\omega)}{dt} \propto |\langle\psi_f|H'(\mathbf{r})|\psi_i\rangle|^2 \rho(\hbar\omega - E_B)\delta\big(E_f - (\hbar\omega - E_B)\big), \quad (3.4)$$

where $\rho(\hbar\omega - E_B)$ is the density of energy states available at the final state (vacuum level), and $H'(\mathbf{r})$ is the spatial component of the perturbing Hamiltonian. The delta $\delta\big(E_f - (\hbar\omega - E_B)\big)$ expresses energy conservation: transitions can only occur when the photon energy matches the energy difference between the final and initial state.

In the second step, the now delocalized electron travels towards the surface of the material. As afore mentioned, the strong interaction between electrons and matter limits the distance electrons can travel without loosing energy in inelastic scattering processes. This in turn is responsible for the high surface sensitivity of PES techniques, and will be discussed in the next subsection.

In the third and final step, the electrons penetrate through the surface and escape into vacuum. Crossing the surface barrier involves overcoming the potential step ϕ_S that alters the momentum of the photoelectron in the direction normal to the surface plane. However, the in-plane lateral momentum is conserved and can be readily measured in angularly resolved photoemission experiments.

The Escape Depth of Photoelectrons

It is known that X-rays have the ability to travel deep into materials without any significant energy loss or associated attenuation of intensity [49]. When incident on a sample, the energy perturbation by the photons will excite photoelectrons to delocalized energy states throughout the material. All of these electrons may travel towards the surface, but merely a fraction reaches it without experiencing significant energy losses to inelastic scattering mechanisms with the surrounding matter. Ultimately, the depth into the sample from which direct photoemission signals can be received is determined by the *inelastic mean-free path* (IMFP) of electrons in the material they are traveling in. This is the average distance electrons are able to travel without loosing energy to e.g. electron-phonon scattering or Bremsstrahlung from charged particle interaction [46]. The focus of PES techniques is generally directed towards direct photoemission peaks, so the IMFP hence limits the depth from which the relevant line signals can be received.

The IMFP of a material is an empirical quantity, and no model can accurately predict the value for a given material. However, many materials show close resemblance to an overall trend in IMFP: a so-called *universal curve* [50], described by

$$\lambda_e[\text{nm}] = \frac{538a}{E_K^2} + 0.41a^{3/2}\sqrt{E_K}, \quad (3.5)$$

where E_K is the photoelectron kinetic energy in eV. The mean atomic spacing in the material a is roughly given by

$$a \approx \left(\frac{M}{\rho N_A}\right)^{1/3}, \quad (3.6)$$

where M is the atomic weight, ρ is the density of the material and N_A is Avogadro's number. A least-square approximation to the experimental IMFP values of various elements have been reproduced from [50], and is plotted in Figure 3.2a.

Equations 3.5 and 3.6 reveal a weak dependence on the atomic species compared to the strong dependence on the kinetic energy. This opens up for the possibility to tune the surface sensitivity of a PES experiment by changing the kinetic energy of the photoelectrons. Binding energies E_B and the analyzer work function ϕ_A will be set by the material under investigation and the experimental setup, so this can be achieved by changing the incident photon energy. Figure 3.2b illustrates how different information has been obtained about the valence band of a 6H-SiC sample by changing the photon energy from 60 to 100 eV. The higher photon energy 100 eV corresponds to a longer IMFP, revealing more distinct features of higher intensity all the way up to the Fermi energy, some of which were not visible for the more surface sensitive photon energy 60 eV. The difference is likely due to more bulk signal from Si shining through as the IMFP increases, while the more surface sensitive radiation displays a higher fraction of surface oxide signal.

In experiments where changing the incident photon energy is not possible, a frequently used trick is to change the experimental geometry so that the detector is at an angle θ_e to the surface normal. The distance photoelectrons can travel is still limited by λ_e, so the maximum sampling depth t_e is hence scaled according to

$$t_e \propto \lambda_e \cos \theta_e. \tag{3.7}$$

Photoelectron Cross-Sections

Quantification of PES signals from core level states requires the relative intensity of photoelectrons being excited from different energy states, i.e. orbitals, to be known. The amount of signal received from a given orbital will be determined by the probability of freeing an electron with the incoming photon energy. As outlined by Saxon [47], if the detector receiving the photoelectrons is placed at a solid angle $d\Omega$, the relative probability that an electron will emerge into the detector is given by

$$d\sigma = \frac{\text{rate of outgoing electrons to } d\Omega}{\text{rate of incoming photons}} = \frac{\mathbf{J}_{sc} \cdot d\mathbf{S}}{|\mathbf{J}_{inc}|} d\Omega, \tag{3.8}$$

where $\mathbf{J}_{sc}$ is the probability flux of the outgoing electron and $\mathbf{J}_{inc}$ is the probability flux of the incoming photon. $\mathbf{J}_{sc} \cdot d\mathbf{S}$ is then the probability of the particle passing through the area $d\mathbf{S}$ of the detector per unit time, while $d\sigma$ symbolizes the tiny cross-sectional are photons hit that will scatter electrons to the solid angle $d\Omega$. The probability per unit time that a particle is emitted to $d\Omega$ is then $dW = |\mathbf{J}_{inc}| d\sigma$, i.e. the cross-section that scatters to $d\Omega$ scaled by the incoming probability flux of photons.

Evidently, the rate of outgoing electrons from a given energy state hitting the detector can be described by the cross-sectional area $d\sigma$. Recall also that the rate of photoelectrons generated by incoming radiation of energy $h\nu$ to all spacial directions was given by Fermi's Golden Rule (3.4). It can be shown that the two are related by

$$d\sigma = \frac{dW}{|\mathbf{J}_{inc}|} \propto |\langle \psi_f | H'(\mathbf{r}) | \psi_i \rangle|^2 d\rho(\hbar\omega - E_B) \delta\big(E_f - (\hbar\omega - E_B)\big), \tag{3.9}$$

where $d\rho = \rho\frac{d\Omega}{4\pi}$ is the fraction of the total density of states available at $d\Omega$, assuming ρ is angularly invariant. $\langle\psi_f|H'(\mathbf{r})|\psi_i\rangle$ is again the spatial part of the perturbing Hamiltonian, often referred to as the *dipole term.* As it turns out, the chemical environment of the parent atom is relatively insignificant for the photoionization cross-section of any orbital [48]. Hence solving the inner product of the dipole term for a given transition, and integrating eq. 3.9 over all solid angles will provide a measure of the amount of photoelectrons emitted from a specific orbital in a solid.

Figure 3.3 plots the calculated photoionization cross-sections as a function of incident photon energy for some of the relevant orbitals in this experiment. The Figure shows that the photoionization cross-section of all orbitals is lower at higher photon energies than near the "threshold energy" needed for the excitation. Generally, this is the case for all elements, and can be explained from how the dipole element in eq. 3.9 decreases with higher kinetic energies for the freed electrons. A higher incoming photon energy means the outgoing electron will have a higher kinetic energy, and hence shorter de Broglie wavelength. This means ψ_f will oscillate (i.e. change sign) more rapidly in the localized region of ψ_i, decreasing the magnitude of the integral. Furthermore, heavier elements will have a higher cross-section for a given photon energy than lighter elements, due to their heavier cores and stronger electrostatic interaction with the core level electrons [48].

Typical Features of a PES Spectrum

As alluded to in the description of the photoemission process, the information inherent in PES spectra is both extensive and delicate. Careful considerations must be taken in order to appropriately quantify the physical phenomena of the underlying photoemission process and the experimental detection of photoelectrons. The measured signal in its simplest form will contain contributions from the intrinsic excitation process of the photoelectron, known as the *primary spectrum*, and the escape of the electron through the material and the surface, which adds the *secondary spectrum* [46]. The primary spectrum provides the chemical fingerprint of of the elements present, but not all of its features is directly related to the occupied density of states in the material. The following summarizes the most significant features of a typical PES spectrum, based on the introductory texts by Watts, Wolstenholme and Hofmann [53, 54].

Direct Photoemission Peaks   Subjecting a sample to incident X-rays will excite electrons from the orbitals of the atoms present if the incoming photon energy exceeds the binding energies E_B of the occupied states. These electrons may, with sufficient kinetic energy, cross the sample surface and eject into vacuum. A simplified schematic of the process is shown in Figure 3.4a. If no energy losses occur but what is needed to overcome the surface work function ϕ_S, the electron energy is given by eq. 3.2 and may hence be directly translated into the binding energy of the initial state. The intensity lines of direct photoemission from core levels can be used for identification and quantification of the elements present in the top layers of the sample. They are labeled according to the atomic orbital the electrons originate from, e.g. C $1s$, Si $2p$, Ru $3d$ etc.

Chemical Shifts   The observed binding energy of direct photoemission peaks are not only dependent on the binding energies of the parent atoms, but also on the chemical states they exist in. For instance, atoms bonding in stochiometries different from their pure

(a)

(b)
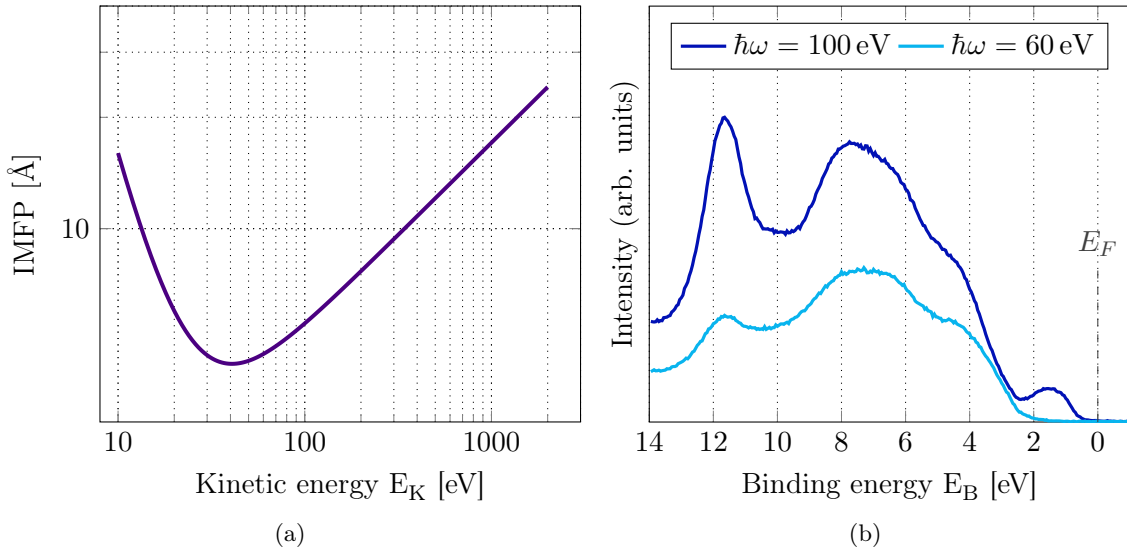
Figure 3.2.: **(a)** "Universal curve" for the inelastic mean free path of photoelectrons through a material as a function of their kinetic energies [50]. **(b)** The measured valence band spectra of an untreated Si face of 6H-SiC at photon energies $60\,\text{eV}$ and $100\,\text{eV}$. The resolution of features near the Fermi level E_F for the higher photon energy is attributed to a higher fraction of bulk signal received due to the higher IMFP.
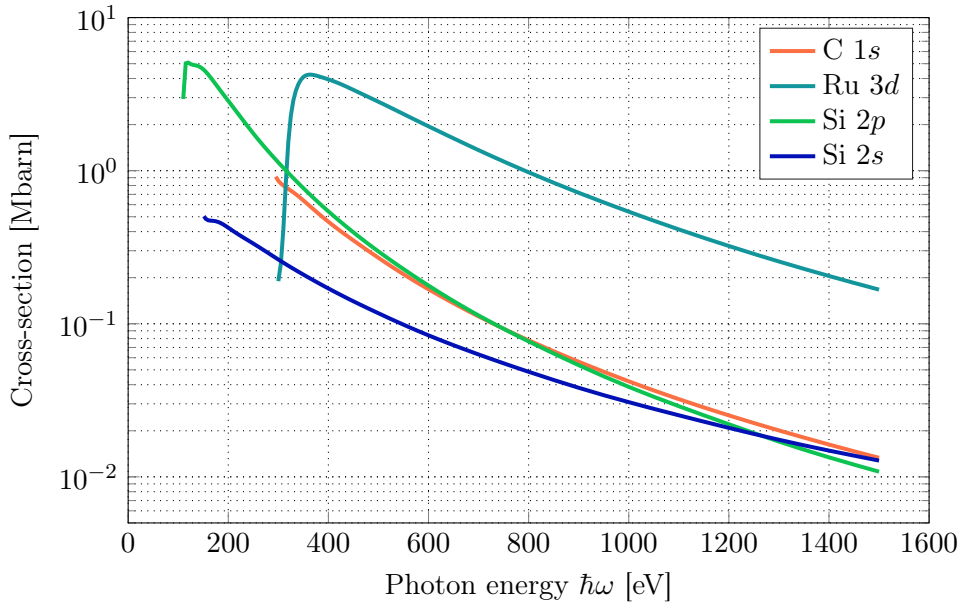
Figure 3.3.: Photoionization cross-sections for orbitals C $1s$, Si $2s$, Si $2p$ and Ru $3d$, as calculated in the dipole length approximation [51, 52].

element form will experience changes in their effective charge potentials if the bonding atoms involved differ in terms of electronegativity. This in turn causes shifts in the observed binding energies that can be translated into what chemical bonds, and hence compounds, are present in the sample. The intensities of the shifted core level peaks can also be used to quantify the amount of atoms in one chemical state relative to another.

In general, an atom bonding to another more electronegative one will see an increase in the binding energy of its core levels. This is due to the reduced screening of the potential from its nucleus as charge is being removed, increasing the Coulomb interaction with the remaining inner shell electrons. These positive binding energy shifts are particularly pronounced in metals exposed to atmospheric environments, due to their frequent bonding with more electronegative oxygen. The energy shifts in occupied states due to bonding is often referred to as an *initial state effect*, as the perturbation is present prior to the photoionization caused by incident radiation. Another prominent initial state effect is the surface core level shift, caused by the different bonding environment of surface atoms as compared to those in the bulk.

Chemical shifts can also be caused by the relaxation of atoms to minimize their energies following the promotion of a photoelectron. Examples are newly formed photoholes being eliminated by electrons rearranging from lower binding energy states or the polarization of surrounding ions. Such relaxations are known as *final state effects* as they occur as a consequence of and following the photoexcitation process. Final state effects tend to change the kinetic energy of the outgoing photoelectron, hence affecting the observed binding energy in eq. 3.2. In most cases, however, chemical shifts are assumed to originate primarily from initial state effects. Other notable causes of binding energy shifts are surface charging for non-conducting samples and doping effects in semiconducting samples.

Spin-Orbit Splitting   So-called *spin-orbit splitting* occurs in PES spectra where heavier elements exhibiting prominent relativistic effects are present. The effect can be observed as a splitting of core level signals originating from degenerate orbitals of the same non-zero angular momentum ($l \neq 0$) into two separate intensity peaks. Electrons in such orbitals carry both spin $s \pm 1/2$ and an angular momentum l around the nucleus of the atom. This angular motion causes the electrons to experience a magnetic field $\mathcal{B}$ from the core that is moving relative to their different respective rest frames. The field exerts a torque on the magnetic dipole moment of the spinning electron, causing it to align either parallel or anti-parallel to the field direction [15]. The anti-parallel alignment is more energetically favorable than the parallel one, so the original energy level of total angular momentum $\mathbf{J} = \mathbf{L} + \mathbf{S}$ splits into two separate energy levels corresponding to $j = l \pm 1/2$.

The observed peaks in a photoemission spectrum will have an energy splitting that increases with the weight of the nucleus, and scales inversely with quantum number $j = l + s$. The observed peaks will also have a set ratio of cumulative intensity area between the spin up and spin down state, set by the relative degeneracy of states between $j = l \pm s$. The degeneracy for a given total angular momentum j is $2j + 1$, giving a ratio between the area of the spin up and spin down state by

$$r = \frac{2(l+s)+1}{2(l-s)+1}.$$
(3.10)
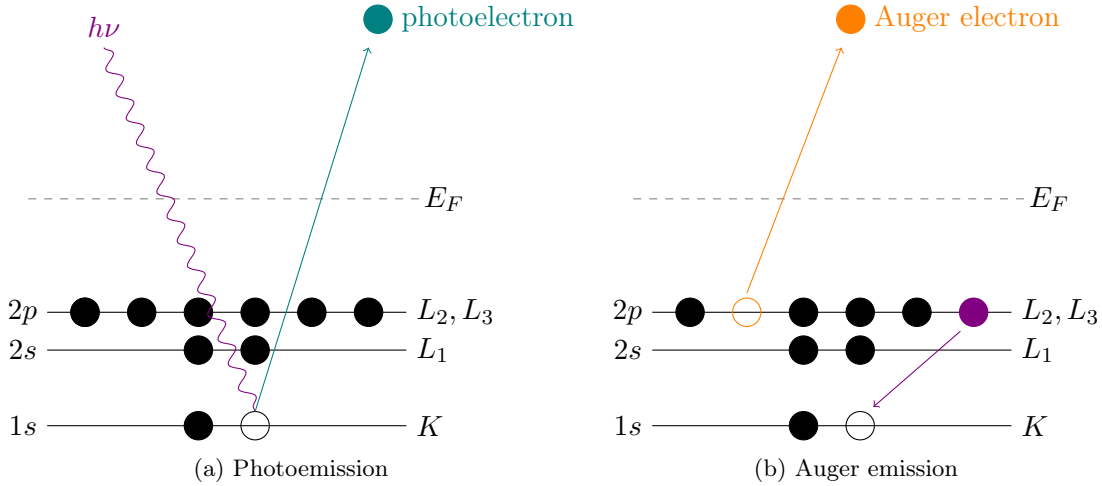
Figure 3.4.: A simplified graphical representation of the Auger process. **(a)** A core level electron is excited by an incoming photon. **(b)** A lower binding energy core level electron is relaxed to eliminate the hole from the photoexcitation, causing a second core level electron to be emitted.

Said differently, angular momentum states occupied by more electrons will give higher intensity peaks in the measured photoemission spectrum. The area ratios for orbitals p, d and f are given in Table A.2 in Appendix A.1.

Auger Emission Peaks   *Auger emission* can occur as a direct consequence of the photoemission process in Figure 3.4a. Following the emission, the atom quickly rearranges its electrons to eliminate the photohole in the core level. The transition of another electron of lower binding energy into the empty state will dissipate energy, either in the form of an emitted photon or by kicking out a second electron known as an *Auger electron*. These appear as Auger emission peaks along with the direct photoemission peaks in a PES spectrum. The Auger process is illustrated in Figure 3.4b.

Since the excitation is caused by a transition between two defined energy states in the atom, the Auger electron's energy is independent of the photon energy of the source

$$E_{K,A} = (E_{B1} - E_{B2}) - E_{B3} - \phi_S, \qquad (3.11)$$

where $(E_{B1} - E_{B2})$ is the energy difference between the initial and final state of the relaxing electron, E_{B3} is the binding energy of the Auger electron and ϕ_S is the work function as before. A direct consequence of this is that Auger peaks can be distinguished from primary photoelectron peaks in a photoemission spectrum. By changing the kinetic energy of the incoming photons, the photoemission peaks will shift relative to the energy change but the Auger peaks will not. In experiments where changing the photon energy is easy, this is often done to single out the core level peaks from the Auger peaks of the secondary spectrum [48].

As opposed to photoemission peaks, Auger peaks are labeled using X-ray notation. Each peak is assigned three letters, where the first two denote the transition of the relaxation step and the last letter denotes the energy level the Auger electron is emitted from. For

instance, Si KLL would be the peak of an Auger electron emitted from the L-shell ($n = 2$) of Si, caused by another electron relaxing to shell K (n=1) from shell L. The nomenclature of X-ray and orbital notation is summarized in Table A.1 of Appendix A.1.

Plasmon Losses   Upon photoexcitation, the excited electron passing through the material towards the surface is prone to inelastic scattering processes with the constituent particles of the surrounding matter. One common loss process is *plasmon creation*, where the photoelectron excites one or several collective oscillations in the surrounding electron gas. These oscillating dipoles have finite excitation energies, oscillating with frequencies characteristic of the material they exist in. For a plasmon excited in the bulk of a material, the first order excitation with the characteristic plasmon frequency ω_P is given by

$$\hbar\omega_P = \Big(\frac{\hbar^2 n e^2}{m_e \epsilon_0}\Big)^{1/2}, \tag{3.12}$$

where $\hbar$ is the reduced Planck constant, e is elementary charge, n is the density of conducting electrons, m_e is the effective electron mass and ϵ_0 is the permittivity in vacuum [48]. In addition, the photoelectron may excite so-called *surface plasmons* upon crossing the surface barrier into vacuum. The plasmon frequency of surface oscillations is related to that of the bulk by $\omega_{SP} = \omega_P/\sqrt{2}$. In an observed photoemission spectrum, plasmon losses from core level electrons will appear as duplicate peaks with higher binding energies, i.e. lower kinetic energies. The bulk plasmon peaks will appear separated from direct photoemission peaks by energies $\hbar\omega_P$, $2\hbar\omega_P$, $3\hbar\omega_P$..., or for surface plasmons $\hbar\omega_{SP}$, $2\hbar\omega_{SP}$, $3\hbar\omega_{SP}$ etc.

Satellites and Ghost Peaks   *Satellite peaks* will be present in the photoemission spectrum if not perfectly monochromatic X-ray radiation is used for the photoexcitation. They occur due to excitations from minor components of the X-rays generated with different energies than the main component. The existence of these minor components are easy to understand from the way X-rays are generated in a standard Coolidge tube [49]. The acceleration of electrons towards a specific anode material kicks out core electrons and creates holes in the inner shells that are eliminated by the relaxation of higher energy electrons. These relaxations emit photons of wavelengths set by the energy difference of the transition. Although the aim is to generate photons with one specific transition energy, other transitions will occur, resulting in photons of different wavelength and energy. Hence one wavelength will be dominating, but others will also be present and incident on the sample in a photoemission experiment. The peaks generated from other transition energies are called satellite peaks. These can generate intensity lines from the same transitions in the material as the primary X-ray transition energy, but with lower intensity and different kinetic energies according to eq. 3.3. Although eliminating satellites from PES spectra is difficult, they can often be attributed to specific transitions in the anode material used, and hence assessed during analysis.

Ghost peaks can arise from unexpected X-ray wavelengths irradiating the sample. These originate from e.g. "crosstalk" in twin anode guns, where misalignment of the anode materials generate some radiation simultaneously from both. In most cases, ghost peaks can be eliminated by adjusting the X-ray equipment.

Background Spectrum Photoelectrons that have undergone one or multiple inelastic scattering processes upon leaving the material reach the photodetector with lower kinetic energy than those generated from direct photoemission. These electrons will tail up behind direct emission lines in the kinetic energy vs. intensity spectrum, providing little or or no information about their initial states in the sample under investigation. Along with the white noise of electrons reaching the photodetector inside the analysis chamber, they make up the background of a photoemission spectrum.

Ultraviolet Photoemission Spectroscopy

Ultraviolet photoelectron spectroscopy (UPS) uses electromagnetic radiation in the ultra-violet regime instead of X-rays to probe the electronic states of the surface layers in a sample. The longer wavelength and hence lower energy of the incoming photons means the core level states are no longer accessible for photoemission. UPS rather aims to excite electrons from lower binding energy orbitals. For photons in the ultraviolet regime this typically corresponds to populated states the valence band of the atoms. The obtained spectra is a convoluted plot of the density of occupied electronic states in the valence band, which is determined by the band structures of the atoms under investigation. This allows UPS spectra to be used for distinguishing between different bonding structures of surface layer materials [54].

Although soft X-rays can in fact be used to probe some valence band features, UPS benefits from having higher photoemission cross-sections for valence band electrons due to their lower photon energy. This makes the resolution of valence band data from UPS better than what is obtainable by X-rays in most cases[2] [46]. UPS is hence suitable for the probing of band structures in *angle-resolved photoemission spectroscopy* (ARPES). Also, the production of UV light is in many cases easier than generating X-rays [55].

The mapping of a sample's valence band structure by UPS can provide valuable additional information to the elemental analysis obtained from XPS. As the valence electrons are often heavily involved in bonding with adjacent atoms, the valence band spectrum provides information on the electronic properties of species in the surface layers. For instance, a distinct difference is observable between the UPS spectra of metallic samples and semiconductors or insulators. For metals the observed intensity will be high up to a kinetic energy roughly equal to the incoming photon energy. Here it drops rapidly to zero, signaling that the sample has states occupied all the way up the Fermi level, as is expected for metals[3]. In comparison, the intensity of the valence band spectra for semiconductors and insulators vanishes with an observable separation relative to $E_k = h\nu \approx E_F$. This is because their Fermi levels exist inside the band gap of the material, and states are only occupied up to the top of the valence band.

Detecting Photoelectrons

The discussion so far has largely focused on the generation of photoelectrons and the intrinsic properties of their excitation processes that lead to observable features in photoemission spectra. However, to perform any PES analysis whatsoever one needs to be

---

[2]the use of high intensity synchrotron radiation is an exception.

[3]Remember that the binding energy is defined relative to the Fermi level, so an intensity drop at $E_K \approx h\nu$ signals $E_B \approx 0$ and hence metallic bonding if ϕ_A is corrected for.

27
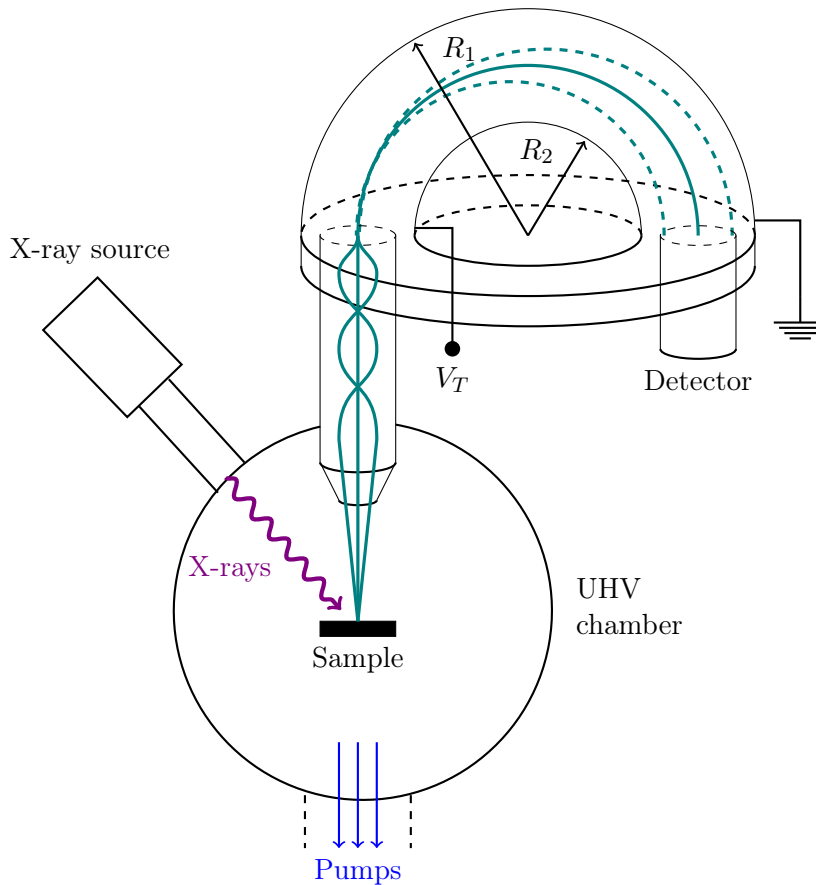
Figure 3.5.: Overview of the main components of a typical photoemission spectroscopy setup. Excited photoelectrons are focused through a set of electromagnetic lenses, selecting their kinetic energy as they enter a hemispherical analyzer using a retarding voltage. A bias voltage V_T is applied between the two concentric hemispheres of the analyzer, dispersing the beam of incoming electrons. A detector of finite slit size at the other end accepts and counts electrons with a kinetic energy equal to the pass energy E_{pass} of the system, as given in eq. 3.13.

able to detect and distinguish outgoing photoelectrons based on their kinetic energy or momentum. The most common detection systems mainly consist of three components: (i) a set of optics that collects and focuses outgoing photoelectrons, (ii) an analyzer that separates them by their kinetic energy and finally (iii) a detector that collects and counts the number of incoming electrons. This subsection outlines the operation of a commonly used detection system known as a *concentric hemispherical analyzer* (CHA) as described by SPECS [56]. The performance of CHAs and their effect on the spectral resolution are also discussed.

A typical photoemission setup using a hemispherical analyzer can be seen in Figure 3.5. The CHA consists of two concentric hemispheres with different radii R_1 and R_2. A potential difference V_T is applied between the two, establishing a radial electric field that will deflect incoming electrons. Photoelectrons with different linear momentum will

experience different degrees of deflection from the field. Hence the analyzer disperses the electron beam into paths of different radii towards the detector. The finite width of the exit slit at the other end of the hemispherical limits what radial paths are accepted into the detector, and hence the kinetic energy of the incoming electrons. This energy is referred to as the *pass energy* E_{pass} of the system, and is given by:

$$E_{pass} = -qV_T \cdot \left[\frac{R_1 R_2}{R_1^2 - R_2^2} \right], \tag{3.13}$$

where q is the electron charge.

In photoemission the potential difference between the concentric hemispheres are usually kept constant, and the energy of incoming photoelectrons is selected by varying the retarding potential of the lens system. This is known as a *fixed analyzer transmission mode*, and is preferential as the energy resolution of the analyzer depends on the pass energy according to

$$\frac{\Delta E_{an}}{E_{pass}} = \frac{S_1 + S_2}{4R_0} + \frac{\alpha^2}{4}, \tag{3.14}$$

where S_1 and S_2 are the entrance and exit slit widths in the energy-dispersive direction, respectively, R_0 is the mean of R_1 and R_2, and α is the detector's half angle of acceptance.

Equation 3.14 suggests that smaller pass energies yields better resolution for the experiment. However, lower pass energies also tend to worsen the signal-to-background ratio, as the integral signal intensity for measured photoelectrons originating from a given core level is roughly proportional to the square of the pass energy:

$$I \approx \frac{E_{pass}^2}{E_k}. \tag{3.15}$$

Essentially, there is a trade-off between signal intensity and energy resolution. Hence the choice of pass energy largely depends on what features need to be resolved in order to receive the necessary information about the physical system. Survey scans typically run with high pass energies, sacrificing resolution for high signal intensities. Core level XPS scans tend to run with lower pass energies and several scans for noise averaging, aiming to resolve more subtle spectral features. Different photon sources that can deliver different radiation flux intensities will also generally run with different pass energies: the most obvious example would be X-ray lab sources versus synchrotron radiation (this will be further discussed in Chapter 3.2).

Line width and Intensity of Core Level Signals

The direct line signal received from a specific energy state will be prone to several broadening mechanisms. The finite lifetime of the excited state, i.e. the generation of an excited electron and a core hole, adds Lorentzian broadening to the line signal [46]. For a core hole with mean lifetime τ, the *intrinsic* or *natural* line width 2α, is given by the *energy-time uncertainty principle* [57]:

$$2\alpha = \frac{\hbar}{\tau} = \frac{6.58 \times 10^{-16} \text{eV} \cdot \text{s}}{\tau \, [\text{s}]}, \tag{3.16}$$

where $\hbar$ is the reduced Planck constant. For a given element, the core hole lifetime 2α will typically be larger for orbitals closer to the nucleus, as these can be readily filled

by surrounding electrons from higher energy states. Similarly, for a given core level (e.g. $2s$) 2α will increase with increasing atomic number Z, as heavier atoms will have higher densities of valence electrons that can fill the photohole [58].

In addition to the Lorentzian profile from intrinsic lifetime broadening, thermal Doppler broadening from the outgoing electrons, the line shape of the incoming X-rays and the transmission properties of the spectrometer will induce a Gaussian profile [56, 59]. The thermal broadening will in many cases be negligible, and therefore the main Gaussian contributions are determined by the performance of the experimental instrumentation. These broadenings can be combined into one Gaussian profile with a full width at half-maximum (FWHM) of [56, 60]:

$$FWHM_G = \left[(\Delta E_{an})^2 + (\Delta E_{\hbar\omega})^2\right]^{1/2} = 2\sqrt{2\ln 2} \cdot \sigma_G, \qquad (3.17)$$

where σ_G is the Gaussian standard deviation. The Gaussian profile should in turn be *convoluted* with the Lorentzian profile to give the fully broadened line shape of the core level signal. To a first approximation, the total FWHM of the signal can be described by a quadratic sum of the Gaussian and Lorentzian contributions [61]:

$$FWHM_{tot}^2 = (2\alpha)^2 + FWHM_G^2. \qquad (3.18)$$

The intensity of line signal received by the detector will not only depend on intrinsic properties of the sample like e.g. photoionization cross-sections, inelastic mean free paths and atomic densities, but also the performance of the ionization source and the detector, and the overall geometry of the experiment. For core level studies, it is customary to fix the relative geometry of the sample, detector and ionization source at every stage in an experiment. This tends to reduce the number of variables affecting the line intensity. The detector is often aligned with the surface normal ($\theta = 0$ in eq. 3.7) of the sample in so-called *normal emission mode*. Fixing the angle of irradiation also eliminates any geometric factors from the photon flux intensity between consecutive scans. For the simple case of a homogeneous sample consisting of an element A, the intensity of the background-subtracted line signal I_A from photoelectrons with energy E_K is then given by [54]:

$$I_A = F(\hbar\omega) \cdot \sigma_A \cdot n_A \cdot W_A(\varphi, l) \cdot \lambda_A(E_K) \cdot T(E_K). \qquad (3.19)$$

Here, $F(\hbar\omega)$ [$cm^{-2}\,s^{-1}$] is the photon energy-dependent flux of the source at a fixed angle relative to the surface normal, σ_A [cm^2] is the photoionization cross-section, n_A [nm^{-3}] is the atomic number density, λ_A [nm] is the inelastic mean free path, $T(E_K) \approx E_K^{-0.5}$ [eV] is the intensity/energy response of the spectrometer, and the coefficient $W_A(\varphi, l)$ describes the angular intensity distribution of photoelectrons excited by unpolarized X-rays. The latter term for a given sub-shell (atomic number n) depends on the angular momentum number l, and the angle φ between the incoming beam of photons and the entrance slit of the analyzer. This angle is typically set to be 54.7°, where $W_A(\varphi, l) \approx 1$ for any specie and can be neglected.

Equation 3.19 Is only accurate for simple and homogeneous systems consisting of mono-atomic species. However, it is still surprisingly powerful for non-homogeneous systems where the material specific factors deviate only slightly from σ_A and n_A of a closely related homogeneous system. It is also useful for determining the relative concentration of different species in the same sample, e.g. Si and C in an SiC substrate [53]. When

comparing core level signals taken at $\varphi = 54.7°$ from different orbitals in the same sample that are excited to the same kinetic energy, i.e. roughly the same IMFP according to the universal curve (eq. 3.5), the ratio of equation 3.19 for species A and B can be taken and manipulated to give

$$\frac{n_A}{n_B} = \frac{I_{A,i}}{I_{B,j}} \cdot \frac{\sigma_{B,j} \cdot F(\hbar\omega_{B,j})}{\sigma_{A,i} \cdot F(\hbar\omega_{A,i})}, \tag{3.20}$$

where $\hbar\omega_{A,i}$ and $\hbar\omega_{B,j}$ are the photon energies needed to excite electrons from orbitals i and j in species A and B to the same kinetic energy, respectively.

Quantitative XPS Analysis

Quantitative analysis of XPS spectra requires accurate measurements of intensity lines from core level signals corresponding to the different chemical states of the elements present. The determination of these intensities is in practice done by assigning the appropriate area under a peak to a signal of photoelectrons from a given energy state. The measured signals are, as previously described, a mixture of signals from the intrinsic excitation process and the inelastic scattering process as the photoelectron leaves the material. Furthermore, different chemical environments for atoms of the same element in the sample give rise to energy perturbations for the core level electrons. Hence the signal from one specific element will be the sum of the lines from each chemical state present, as well as the added features from intrinsic excitations and inelastic scattering.

Each expected photoemission peak is commonly fitted by convolving the direct line signal with a Lorentzian and Gaussian component having spectral widths α and γ, respectively. As explained in the previous subsection, the Lorentzian component represents the lifetime broadening of the excited state, while the Gaussian component accounts for thermal and instrumental broadenings. The fully assembled signal is known as a *Voigt profile*

$$V(E - E_0; \alpha; \gamma) = L(E - E_0) \otimes G(E - E_0) = \int_{-\infty}^{\infty} L(E'; \alpha) G(E - E_0 - E'; \gamma) dE', \tag{3.21}$$

where E_0 is the position of the peak maximum in the spectrum. The Voigt profile has no analytical form, and from a practical point of view it is inconvenient to calculate the convolution integral in eq. 3.21 for every value of E numerically. Therefore, it is common practice to approximate the line shape by a *pseudo-Voigt*, which is simply a normalized sum of the Lorentzian and Gaussian component. The latter is described by equation 3.22, where $\mu \in [0, 1]$ controls the relative weight of the two components

$$\begin{aligned}
PV(\tilde{E}) &= (1 - \mu)G(\tilde{E}) + \mu L(\tilde{E}) \\
&= (1 - \mu)\sqrt{\frac{4\ln(2)}{\pi\tilde{\omega}^2}} \exp\left[-\left(\frac{4\ln(2)}{\tilde{\omega}^2}\right)\tilde{E}^2\right] + \mu\frac{2}{\pi}\frac{\tilde{\omega}}{\tilde{\omega}^2 + 4\tilde{E}^2},
\end{aligned} \tag{3.22}$$

where $E - E_0$ has been replaced by $\tilde{E}$ in eq. 3.22 to improve readability. The factor $\tilde{\omega}$ is the FWHM and is commonly replaced with α in the Lorentzian part and γ in the Gaussian part, or a rooted sum of squares of the two. The mixing factor μ is suggested by Thompson *et al.* as a third degree polynomial containing both α and γ [62], accurate

to 1.2% of the real Voigt profile [63]. The Pseudo-Voigt has proven to be a superior approximation to the Voigt compared to other numerical simplifications [64].

In the process of escaping the parent atom, electrons tend to experience additional losses when excited through the high density of states near the Fermi level. This effect is particularly pronounced in transition metals, where the narrow spacing of energy levels in the valence band facilitates the creation of new electron-hole pairs. This results in an asymmetric tail for the signal peak towards lower kinetic energies, rendering the symmetric Voigt a poor fit to the physical signal. Celebrated closed form analytical solutions have been provided by Doniach and Sunjic [65] and Mahan [66]. While these functions theoretically model the asymmetry to great precision, their application to quantitative analysis by numerical models can prove to be difficult. The line shape of the Doniach-Sunjic function fits metal core levels extremely well over an energy range equal to the signal bandwidth, but the intensity integral diverges for the asymmetric tail. Hence an arbitrary energy cutoff value must be applied to normalize the peak intensities. Moreover, it has been argued that Doniach-Sunjic fit is less suitable for materials with complex valence band structures near the Fermi edge [67]. The Mahan function provides a finite integral that fits asymmetric line shapes in an excellent manner, but requires two convolution procedures and hence higher computational effort than simpler numerical models. Schmid *et al.* suggests the use of a modified pseudo-Voigt function that replaces the FWHM in eq. 3.22 by a sigmoidal step function shifted by a parameter b relative to E_0. This function's performance compares reasonably well to that of the Mahan function, and requires much less computational power [59]. For this reason, the fitting of asymmetric line shapes in this project is done according to Schmid's modification of eq. 3.22, with the FWHM taken as the shifted Sigmoid function scaled by two times the rooted sum of squares of the Lorentzian and Gaussian widths

$$\omega_{(E')} = \frac{2\omega_0}{1 + \exp\left[-a(\tilde{E} - b)\right]}, \qquad \omega_0 = \sqrt{\alpha^2 + \gamma^2}. \tag{3.23}$$

Finally, each photoelectron signal will carry an associated background from the inelastic scattering of secondary electrons originating from the same energy level. This appears in the observed spectra around each core level peak as a "step" to a higher constant background intensity for kinetic energies lower than that of the peak signal maximum. The original work by Shirley proposed a now widely used iterative approach to subtracting this background [68]. Since then, careful analysis has revealed that this static approach of subtracting a background signal based on the intensity difference at two points has a tendency to overstate the underlying background [69]. An *active* approach that dynamically fits the background for each peak has several advantages over the static background approximation: most notably it does not understate the intensity of each fitted peak to the same extent. For the sake of reducing computational effort, the background fits in this report employ an error function approximation to the argued intensity step of each peak, fitted around their maximum intensity and scaled by their widths:

$$S(E; E_0, \omega_0) = \text{erf}\left[\frac{E_0 - E}{\omega_0}\right]. \tag{3.24}$$

Here, ω_0 is the familiar rooted sum of squares approximation to the FWHM and E_0 is the position of the peak maximum. The expression in eq. 3.24 will be modulated by a fraction of the assigned peak intensity, and used in conjugation with the constant offset

linear background noise of the detector y_0 to model the background of each line signal. A more elaborate explanation of the practical implementation of peak fits in this project is given in Section 4.4.2.

Layer Modeling

A different way of quantifying XPS spectra is to use the relative intensity of observed peaks to determine the thickness of overlying layers in a heterostructure of different compounds. This is particularly useful in experiments where the thickness of a deposited layer needs to be known in order to accurately asses any observed changes in later spectra. An obvious example would be e.g. the thickness of a deposited metal layer that subsequently reacts and forms new compounds with other species upon some physical treatment. This section derives a simple expression for the thickness of an overlayer on a substrate, assuming the IMFP λ and the cross-sections σ_i of the two materials are known.

By Beer-Lambert's law, the intensity of emitted photoelectrons that have traveled a distance d through the sample is

$$I(d) = I_0 e^{-d/\lambda}, \tag{3.25}$$

where I_0 is the intensity flux of outgoing electrons at the site of excitation. The number of electrons emitted into vacuum from a volume $A \cdot dx$ at depth x into the sample (assuming emission normal to the surface) is then

$$\phi = (A \cdot dx) I_{ph} n \sigma e^{-x/\lambda}, \tag{3.26}$$

where I_{ph} is the intensity of incoming photons and n is the atomic density of the layer. As X-ray attenuation is negligible over the distances similar to λ, the photon intensity can be assumed constant as a function of depth. The total flux of outgoing photoelectrons from an overlayer of thickness d is then

$$\phi_{tot} = AI_{ph} \int_0^d n'\sigma' e^{-x/\lambda'} dx = AI_{ph} n'\sigma'\lambda'\left(1 - e^{-d/\lambda'}\right). \tag{3.27}$$

A similar expression can be found for the photoelectron flux from the underlying substrate layer[4]. The intensity ratio of photoelectrons emitted from the overlayer to that of the substrate is then

$$\frac{I'}{I_s} = \frac{n'\sigma'\lambda'}{n_s\sigma_s\lambda_s} \cdot \frac{1 - e^{-d/\lambda'}}{e^{-d/\lambda_s}}, \tag{3.28}$$

where the overlayer and substrate have cross-sections σ' and σ_s, respectively. If the two layers are assumed to have roughly the same atomic density and IMFPs, equation 3.28 can be simplified to an expression for the overlayer thickness d given by

$$d = \lambda \ln\left[1 + \frac{I'\sigma_s}{I_s\sigma'}\right]. \tag{3.29}$$

---

[4]Here, the integral would run from $-\infty$ to x in the given coordinate system.
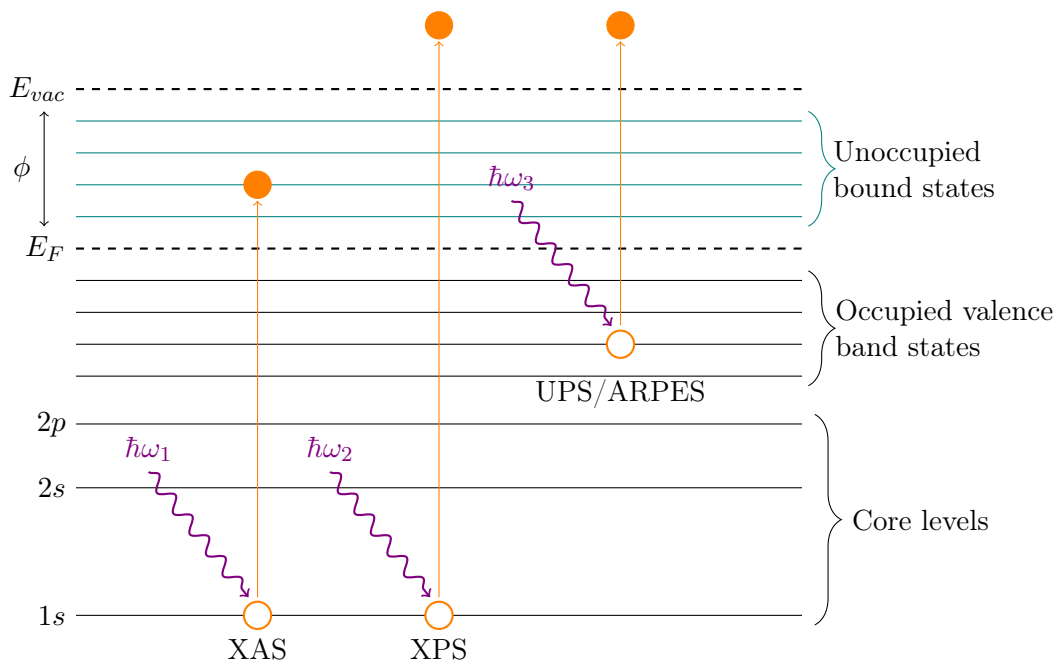
Figure 3.6.: Schematic showing the difference between photoexcitations in XPS, UPS, ARPES and XAS. Notice how bound electrons in the XAS case are excited to unoccupied final states above the Fermi level E_F that are still bound to the parent atom, i.e. below the vacuum level E_{vac}. The energy separations indicated the figure are not to scale.

3.1.2. X-Ray Absorbtion Spectroscopy

X-ray absorbtion spectroscopy (XAS) is used to probe the intra-molecular and extra-molecular bonding, separation and orientation of molecules or functional groups on surfaces or in solids [70]. Similar to the various PES techniques discussed, XAS relies on the absorption of incoming electromagnetic radiation to excite photoelectrons from occupied states in a material. However, XAS techniques seeks to promote electrons not to the continuum of states above the vacuum level, but rather to the set of unoccupied bound states above the Fermi level. This process is sketched in Figure 3.6, where it is apparent how XAS transitions distinguish themselves from photoexcitations in e.g. XPS, UPS or ARPES.

XAS techniques monitor the absorption of incoming electromagnetic radiation by the relevant atomic species, normally being the sub-components of specific molecules of interest, as a function of photon energy. For this reason, all XAS experiments rely on having a tunable source of coherent and monochromatic radiation, and require the continuous spectrum of energies that is only available from a synchrotron source (See Section 3.2.3 for an overview of how these work). This Section discusses the typical features of an XAS spectrum, explains the theoretical basis of the X-ray absorbtion mechanism, what structural information can be retrieved through near edge absorbtion fine structure (NEXAFS) experiments, and finally how XAS can be measured experimentally.
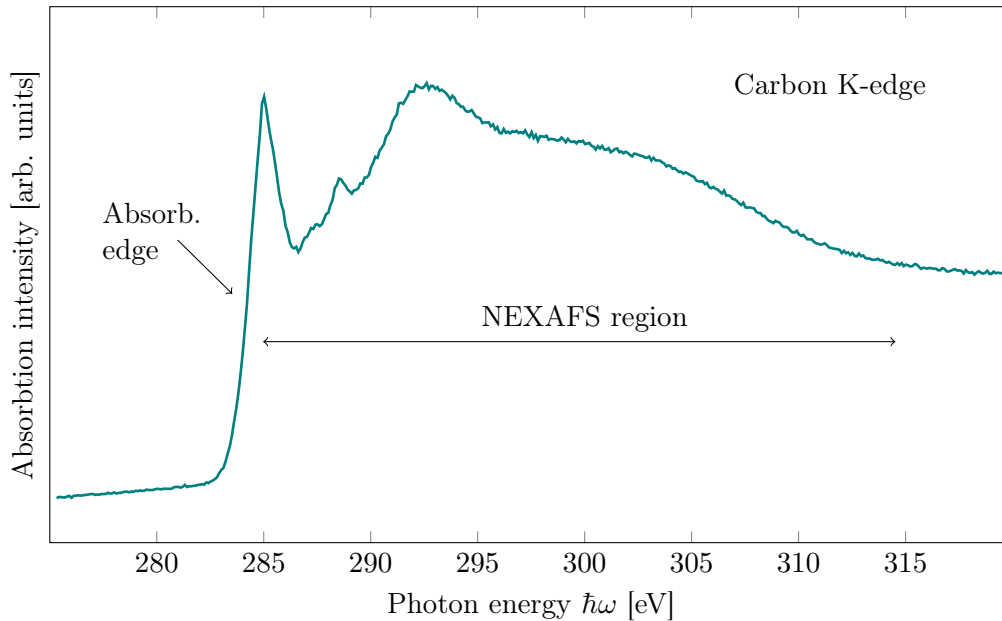
Figure 3.7.: X-ray absorption in the vicinity of the carbon K-edge ($284 - 285\,\text{eV}$ [70, 71]) for a sample of graphitic carbon on a few nanometers of silicon dioxide. Several strong resonances that can be related to specific discrete energy transitions from the 1s core level are visible in the near energy region beyond the absorption edge.

Features of an X-Ray Absorbtion Spectrum

XAS techniques utilize the tunability of synchrotron radiation to reveal features of the absorbtion spectrum that can be directly related to the spatial and electronic structure of a material. The incident photons are scanned across an energy range in the vicinity of the minimum energy needed for a transition from a specific core level to an unoccupied state above the Fermi level. As the photon energy crosses this minimum energy, excitation suddenly becomes possible and the absorbtion cross-section in eq. 3.31 increases dramatically. This can be seen as an intensity step in an absorbtion spectrum, commonly referred to as an *absorbtion edge* [48]. The photon energy at which this edge is observed will be directly related to the binding energy of the specific core level in the atomic specie under investigation. For that reason, these edges are named K-edges, L-edges and so forth using X-ray nomenclature, based on what core level orbital they are related to[5]. A typical X-ray absorbtion spectrum in the vicinity of a carbon K-edge is shown in Figure 3.7.

At photon energies beyond the edge, other features known as the *X-ray absorbtion fine structure* (XAFS) become visible. These are resonant peaks that can be related to the electronic and geometric environment surrounding the absorbing atoms. Features close to the edge (within $30 - 50\,\text{eV}$) are referred to as near edge XAFS, or NEXAFS, while those at energies further away are known as extended or surface extended XAFS (EXAFS or SEXAFS) depending on whether the focus is bulk or surface level features [70]. Beyond the edge there is also a roll-off in absorbtion intensity with higher photon energy. This

---

[5]See Appendix A.1 for an explanation of X-ray orbital notation.

can be explained from the decreasing magnitude of the dipole element and hence also the absorbtion cross-section with increasing energy E_f in the final state (see Fig. 3.3).

Theoretical Description of Photon Absorbtion in XAS

The treatment of excitations in XAS experiments is very similar to that of photoexcitation in PES: the main difference is that excited electrons are still bound to their parent atom or molecule, and never crosses the potential barrier into vacuum. Hence the energy of the electron in the final state is simply a function of the photon energy $\hbar\omega$ and the binding energy $E_{B,i}$ of the initial state

$$E_f = \hbar\omega - E_{B,i}. \tag{3.30}$$

Compared to the expression in eq. 3.2, the surface work function ϕ_S is evidently missing as the electron is never fully ionized. The energy of the final state should not be confused with the similar spelling of the Fermi energy E_F.

The excitation energies $\hbar\omega$ used are typically sufficient to excite the core level electrons of a specie into the unoccupied *antibonding* orbitals of its molecular wave function. These excited orbitals are found at higher energies than the occupied, or *bonding*, molecular orbitals of the structure in its relaxed state. For a given specie, its molecular orbitals (MOs) can be described by linear combinations of the valence orbitals associated with its constituent atoms. The MOs are normally classified by symmetry according to the inter-atomic axis or plane of the molecule, with the most common two groups being σ and π orbitals [72]. The σ orbitals are rotationally *symmetric* with respect to the internuclear axis. Conversely, π orbitals are *asymmetric* with respect to rotation around the internuclear axis, i.e. a phase change gets introduced. Based on these features, σ orbitals can be obtained from both spherically symmetric s orbitals and p orbitals that are parallel to the axis of rotation, while π bands will contain mainly p orbitals orthogonal to the internuclear axis, or plane of the molecule[6]. Excited states are denoted with an asterisk, so that e.g. an antibonding π state will be referred to as π^* [70, 72].

The rate of electrons transitioning from an initial state $|\psi_i\rangle$ to a final state $|\psi_f\rangle$ is again described by Fermi's golden rule (see Section 3.1.1). For excitation light that is linearly polarized along a direction $\hat{\mathbf{e}}$, the absorbtion cross-section is proportional to

$$\sigma_x \propto |\langle\psi_f|\hat{H}(\mathbf{r})|\psi_i\rangle|^2\rho(E_f) \propto |\hat{\mathbf{e}} \cdot \langle\psi_f|\mathbf{r}|\psi_i\rangle|^2\rho(E_f), \tag{3.31}$$

where $\rho(E_f)$ again is the density of states at final energy E_f, and $\langle\psi_f|\mathbf{r}|\psi_i\rangle$ is the dipole matrix element of the perturbation. According to eq. 3.31, the cross-section and thus the intensity of absorbtion for a given transition will be directly proportional to the magnitude of the dipole element squared. For transitions from the $1s$ core level, it can be shown that the matrix element points in the same direction as the net p orbital component of the linear combination making up the excited final state orbital [70]. This behavior can be understood intuitively from the overall conservation of angular momentum for the electron-photon system. As the photon gets absorbed, its spin 1 needs to be accounted for. This requires a change of quantum numbers $\Delta l = \pm 1$ and $\Delta m = \{-1, 0, 1\}$ for the

---

[6]For diatomic molecules, it is common practice to assign the z axis is along the internuclear axis. By this convention, σ orbitals can be formed from p_z and spherically symmetric s orbitals, while atomic p_x and p_y orbitals make up the π orbitals.

excited electron as dictated by the dipole selection rule[7]. If the photoelectron is excited from a $1s$ ground state of $l = 0$, it can only transition into an empty MO with p-like character. Both σ and π bonds contain linear combinations of atomic p-orbitals, and so transitions will have maximum absorbtion cross-section in the spatial directions of the p-components that make up the final σ^* or π^* states.

As it turns out, there is a one-to-one relation between the spatial orientation of such molecular orbitals and the molecular geometry. For instance, chemical species containing aromatic rings like e.g. benzene or graphene form a lowest unoccupied molecular orbital (LUMO) of π^* character that is oriented perpendicular to the plane of the molecule [73, 74]. Said differently, the local spatial symmetry of a final orbital state will determine whether a transition into it is allowed or not by the selection rules of the excitation.

The dot product with the polarization direction $\hat{\mathbf{e}}$ further suggests an angular dependence for the absorption of incoming X-rays. Specifically, one should expect to see the strongest absorption resonances when the polarization of the photon electric field is parallel to the spatial direction $\mathbf{O}$ giving maximum amplitude for the matrix element. The intensity of transition (and hence absorbtion) assumes the simple form

$$I_{if} \propto |\hat{\mathbf{e}} \cdot \mathbf{O}|^2 \propto \cos^2 \delta, \tag{3.32}$$

where δ is the angle between the direction of the electric field and the maximum amplitude direction of the final state orbital [70]. For different final states with different p-wave directionality, e.g. the σ^* and π^* states of aromatic molecules, changing the orientation of the incoming radiation relative to the molecular plane should then shift the rate of transition to the different final states. This can be seen as a change of absorption intensity between the peaks of the near edge fine structure corresponding to the different antibonding final states.

Determining Molecular Orientation from Near Edge X-Ray Absorbtion Fine Structure (NEXAFS)

Near edge X-ray absorbtion fine structure measurements aim to probe the resonance structure near the K $(1s)$ absorbtion edge of different atomic species, bonded in either the surface layers or bulk of a sample [70]. The technique is capable of detecting the presence and length of specific inter-atomic bonds from their antibonding resonance peaks [70, 75]. Another common use of the NEXAFS technique[8] is to determine the orientation of adsorbate molecules relative to a substrate. By varying the polar angles for the incoming synchrotron radiation relative to the sample surface, the angular dependence of the absorbtion cross-section can be exploited to reveal the spatial orientation of antibonding molecular orbitals belonging to the adsorbates. If the orientation of these orbitals relative to the geometry of their parent molecule is known, the molecular orientation on the surface can be determined from the angles where specific absorbtion intensity resonances are achieved [76].

In angular dependent NEXAFS, synchrotron radiation of known spatial polarization is incident on a sample surface covered with known adsorbed or chemisorbed species.

---

[7]See appendix A.2 for an overview of atomic selection rules and a schematic of the allowed transitions between Bohr levels $n = 1$ to $n = 4$.

[8]An alternative name that is used interchangeably is X-ray absorbtion near edge structure (XANES). In this thesis, the acronym NEXAFS will be used exclusively.
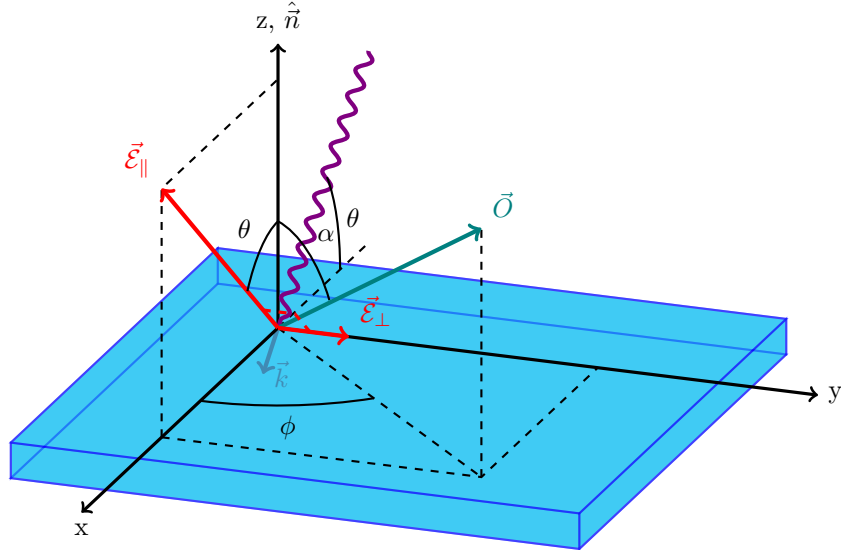
Figure 3.8.: Coordinate system defining the orientation of the **O** excitation vector of a π^* or σ^* state relative to the substrate and the polarization vectors $\mathcal{E}_\parallel$ and $\mathcal{E}_\perp$ of an incoming excitation photon. The relevant angles α, θ and ϕ from eqs. 3.33 and 3.35 have also been denoted.

The absorbtion spectrum near the K-edge is then recorded consecutively with varying angle of irradiation θ relative to the sample plane. This process is illustrated in Figure 3.8. Synchrotron light in the (x, z) plane is incident on a sample with surface normal directed along the z axis. The light for NEXAFS normally has two transverse electric field components $\mathcal{E}_\parallel$ and $\mathcal{E}_\perp$. The polarization is oriented so that the dominant component $\mathcal{E}_\parallel$ also lies in the (x, z) plane, and $\mathcal{E}_\perp$ along the y axis. Component $\mathcal{E}_\parallel$ subtends an angle θ to the surface normal, equal by geometry to the angle of incidence for the collimated beam. The vector **O** represents the direction of a specific p-wave excitation where the dipole matrix element is large, e.g. the p orbital direction of a σ^* or π^* state for excitations from the $1s$ core level. It is situated at angle α relative to the surface normal $\hat{\mathbf{n}}$, with its projection onto the surface plane at azimuthal angle ϕ.

For the given coordinate system, the angle δ from equation 3.32 between the dominant field vector $\mathcal{E}_\parallel$ and the p orbital direction **O** can be expressed as a function of angles θ, α and ϕ. As outlined by Stöhr and Outka [76], the resonance intensity of absorbtion associated with $\mathcal{E}_\parallel$ will then have angular dependence

$$
\begin{aligned}
I_\parallel = A\big[&\cos^2\theta\cos^2\alpha + \sin^2\theta\sin^2\alpha\cos^2\phi \\
&+ 2\sin\alpha\cos\alpha\sin\theta\cos\theta\cos\phi\big],
\end{aligned} \tag{3.33}
$$

where A is the angle-integrated cross-section. The angular dependence of the resonance intensity for $\mathcal{E}_\perp$ is given by

$$
I_\perp = A\big[\sin^2\alpha\sin^2\phi \big]. \tag{3.34}
$$

For adsorbate molecules with threefold rotational symmetry or higher in the azimuthal plane, as seen in e.g. molecules with aromatic rings, the dependence on ϕ vanishes. The

two resonance intensities then simplify to

$$I_\parallel = A\Big[\cos^2\theta\cos^2\alpha + \frac{1}{2}\sin^2\theta\sin^2\alpha\Big], \qquad (3.35)$$

$$I_\perp = \frac{1}{2}A\sin^2\alpha. \qquad (3.36)$$

Equation 3.36 states that beyond the K-edge, $\mathcal{E}_\perp$ will contribute a constant intensity to the background that only depends on the angle between **O** and the surface normal. Any variations in the observed absorption intensity for a given photon energy will be due to the dominant polarization of the beam when the angle of incidence θ is adjusted. Hence by measuring the absorption intensity at various angles θ over the same photon energy range, the magnitude of each orbital-specific resonance feature will increase as $\mathcal{E}_\parallel$ aligns with its respective **O** vector. Maximum intensity will be reached when $\delta \to 0$ and $\theta \to \alpha$. If the spatial orientation of the **O** vector belonging to the final orbital relative to the molecular geometry is known, then the NEXAFS spectrum with the maximum resonance intensity can provide a direct measure of the molecular adsorbate orientation. Based on the optimal incidence angle θ relative to the underlying substrate, the direction spatial **O** will be known and hence also the spatial orientation of the adsorbate.

Detecting XAS Signals

As illustrated in Figure 3.6, excitations in XAS differ from those of PES in that the photoelectrons are promoted to unoccupied, yet bound states of the material. This poses certain restrictions to the way one is able to detect the absorption of incoming photons. In PES, full ionization is achieved and so the electrons promoted to vacuum can be captured and counted by the detector. The number of electrons received is directly proportional to the number of photons absorbed. For XAS, this is simply not possible as the photoelectrons will never escape the material nor reach the detector, and thus cannot be counted directly. The idea is therefore to measure a different physical signal proportional to the X-ray absorption cross-section σ_x, so that the flux of incoming radiation is measured indirectly. For a given specie, the number of absorbed photons per unit time in the small adsorbate concentration limit is roughly

$$N_{abs} \approx I_0 A_0 \sigma_x(\hbar\omega)\rho, \qquad (3.37)$$

where I_0 [photons/(s cm^2)] is the incident photon flux density, A_0 [cm^2] is the surface area exposed to the beam[9], $\sigma_x(\hbar\omega)$ [Mb/atom] is photon energy-dependent and ρ [atoms/cm^2] is the atomic area density [70]. The cue is that the number of electron-hole pairs generated by the photoexcitation can be directly related to N_{abs}. Hence detecting by-products from the subsequent core hole annihilation associated with the relaxation of excited atomic species will provide a direct measure of the probability to excite core electrons to anti-bonding states by X-ray absorption.

As discussed in Section 3.1.1, secondary de-excitation will generate either a fluorescent photon or an Auger electron. The common ways to measure X-ray absorption are hence from the yield of fluorescent radiation or secondary Auger electrons. Note that the relative

---

[9]This beam spot area will, of course, be dependent on the angle of the incoming X-rays relative to the surface.

yield of these two emission processes is strongly related to the atomic number Z of the excited parent atom. For low-Z atoms like e.g. C, N or O, the Auger decay is faster than the fluorescent process and hence dominates [77]. The detection of Auger electrons is also highly surface sensitive due to the short inelastic mean free path of the escaping photoelectrons. This makes *electron yield detection* ideal for studying lighter chemical species near the a sample surface. As the XAS work of this thesis mainly focuses on detecting carbonic allotropes in surface layers, only the principles of electron yield detection will be explained.

Despite the inherent surface sensitivity of Auger electron emission, the detection of photon absorption by chemisorbed surface species are not without experimental and instrumental challenges. The concentration of such species are generally quite small, and requires a high intensity flux of incoming photons to achieve reasonable count rates. Although limited by the IMFP of the photoelectrons, signal from the underlying substrate will also increase with higher photon intensity flux. The signal received will hence be the absorption signal of Auger electrons from the surface layers, superimposed on a background of all other electrons excited from the substrate that reach the detector. For K-shell excitation, maximizing the signal of Auger electrons resulting from de-excitation relative to the background intensity is therefore desired to better resolve characteristic fine structure features from the atomic species of the adsorbates.

As explained in Section 3.1.1, Auger peaks result from de-excitation transitions characteristic to the electronic structure of the parent atoms. Hence the energy of emitted Auger electrons is independent of the incoming photon energy, and different atomic species will have Auger peaks at different kinetic energies. The intensity for a specific peak, however, will change with photon energy because of the changing absorption cross-section. It is therefore common to select a narrow window of accepted energies that is centered around a characteristic Auger energy E_A using an electron energy analyzer. This will help filter out intensity features in the kinetic energy spectrum that are not related to the Auger transition, hence maximizing the signal corresponding to photon absorption and promotion to unoccupied bound states in the surface layer species. This form of detection is known as *Auger electron yield* (AEY). The signal intensity from an *adsorbate* layer with atomic area density ρ^A and K-shell absorption cross-section $\sigma_x^A(\hbar\omega)$ into a solid angle Ω is given by

$$I_a^A = \frac{\Omega}{4\pi}\kappa_a^A N_{abs}^A = \frac{\Omega}{4\pi}\kappa_a^A I_0 A_0 \sigma_x^A(\hbar\omega)\rho^A, \tag{3.38}$$

with κ_a^A being the yield factor for the Auger emission process [70]. Here, the fraction of X-rays absorbed in the adsorbate layer is assumed to be small, i.e. $\sigma_x^A(\hbar\omega)\rho^A \ll 1$. In this limit the intensity of Auger electrons received is directly proportional to the absorption cross section, and hence also the number of electrons promoted to antibonding states by a constant factor (see eq. 3.37).

A second, simpler detection mode known as *partial electron yield* (PEY) restricts the energy window of detection only on the lower end, allowing all photoelectrons with kinetic energy greater than the set pass energy E_p into the detector. For this reason, the count rates of the PEY mode are higher than for AEY. However, as all photoelectrons with kinetic energies higher than E_p are accepted, the overall background signal is bigger and the signal-to-background ratio reduced. The final and third detection mode is known as *total electron yield* (TEY), and collects photoelectrons of all energies emerging from

the sample. This mode has by far the highest count rates, but also the lowest signal-to-background ratio.

Finally, it is worth noting how photon energy-dependent features, most notably photoemission core signals, affect the electron yield intensity recorded by the detector. Evidently, these signals will drift to higher kinetic energies in a photoemission spectrum as the photon energy is increased (eq. 3.3). For detection modes AEY and PEY that each have a restricted window of accepted energies, such features may drift into the window at the lower energy end. This will distort the electron yield intensity received, appearing as features in the XAS spectrum that are not related to the fine structure of the absorption. Therefore, care must be taken in choosing the right energy bounds and range for the incoming photon energy. PEY offers some more flexibility than AEY, as all unrelated features existing within the energy window at the lowest achievable photon energy will be present for all higher photon energies as well. Hence these features merely contribute to the overall background. The range of photon energies used therefore only needs to be restricted by the point where new photoemission signals cross E_p and emerge in the spectrum.

3.1.3. Low-Energy Electron Diffraction

Low-energy electron diffraction (LEED) is a form of Bragg diffraction, utilizing the short IMFP of electrons ejected towards a sample to study its surface crystallinity. The incoming electrons are accelerated over a potential difference that gives them kinetic energy E_k, and hence de Broglie wavelengths given by

$$\lambda_e = \frac{h}{p_e} = \frac{h}{\sqrt{2m_e E_k}},$$
(3.39)

where m_e is the electron mass. For acceleration voltages of a few hundred eV, this wavelength corresponds roughly to common atomic spacings observed in most crystals. An incoming electron wave will scatter off adjacent atomic sites at the surface of a sample, and if elastic scattering is assumed for all electrons, the outgoing electron wave will experience constructive interference in the plane parallel to the sample surface if

$$\mathbf{k}_f^{||} - \mathbf{k}_i^{||} = \Delta \mathbf{k}^{||} = \mathbf{G},$$
(3.40)

where $\Delta \mathbf{k}^{||}$ is the change in the electron wave vector parallel to the surface upon scattering. $\mathbf{G}$ is a surface reciprocal lattice vector for the sample. This is known as the surface version of the Laue condition [48].

Figure 3.9a shows a schematic of a typical LEED setup. A sample is placed under UHV where an electron gun accelerates electrons towards the sample. The electrons scatter off the crystal surface and hit a fluorescent screen, where a two-dimensional interference pattern that satisfies the condition in eq. 3.40 can be seen. The UHV minimizes the interaction of incoming low-energy electrons with residual gas particles on the way to and from the scattering sample.

From the known geometry of the setup and magnitude $|\mathbf{k}_s| = |\mathbf{k}_i|$ of the elastically scattered electrons, the distance from the center of the viewport d_{hk} at which constructive interference can be observed is given by

$$d_{hk} = R \sin \Theta_{hk} = R \frac{\hbar}{\sqrt{2m_e E_k}} \cdot |h\mathbf{b}_1 + k\mathbf{b}_2|,$$
(3.41)
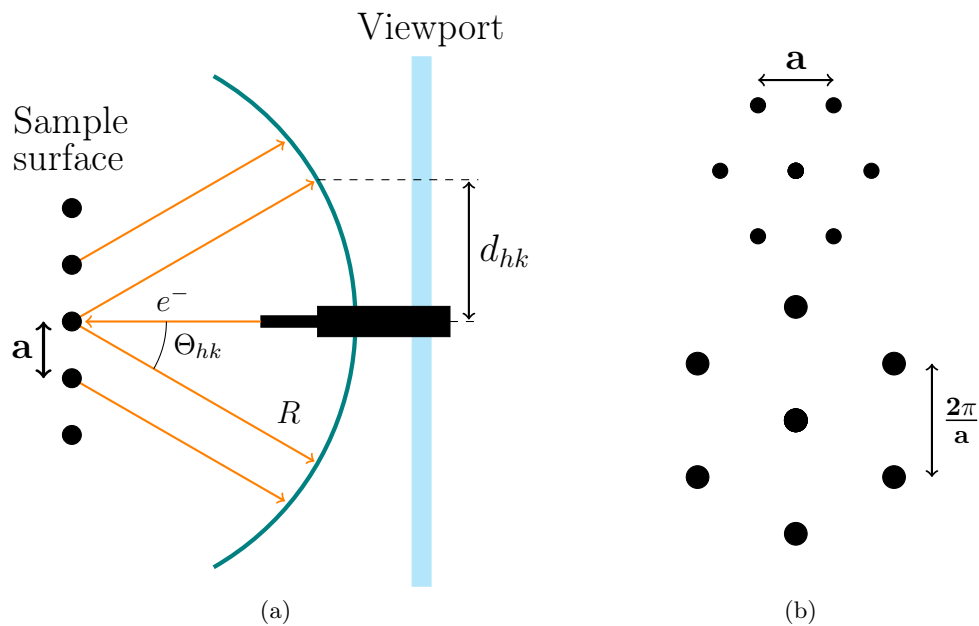
Figure 3.9.: (**a**) A sketch of a typical LEED setup, used to determine determine the reciprocal lattice of a sample surface. (**b**) Hexagonal 2D lattice (top) as is expected for graphene, and its reciprocal lattice, rotated by 30°.

where R is the radius of the screen and $\mathbf{G} = h\mathbf{b}_1 + k\mathbf{b}_2$ is the corresponding surface reciprocal lattice vector [48]. The magnitude of $\mathbf{G}$ can again be translated into the magnitude of the corresponding real space lattice vector $|\mathbf{a}|$ at the surface, given by [22]:

$$|\mathbf{G}| = \frac{2\pi}{|\mathbf{a}|}. \tag{3.42}$$

A good, distinct LEED pattern requires the sample under investigation to exhibit a highly ordered surface structure. LEED is hence commonly applied in surface science experiments to determine the crystalline quality of the surface layers. A pure inspection of the obtained pattern will give an immediate impression of the surface order and quality. Any subsequent changes in the topography from e.g. surface reconstruction or adsorbates will be revealed from a change in the order or sharpness of the observed pattern.

3.2. Generating Electromagnetic Radiation

Most of the experimental techniques discussed in the previous Sections rely on some form of photoexcitation by incoming electromagnetic radiation. The spectroscopic information generated often contains information that is directly dependent on the energy and intensity of the excitation source, with features needing ot be resolved with sub eV precision. Hence excitation sources where the user has stringent control of the wavelength, intensity and coherence of the incoming photons are required. This poses the need for ways to generate electromagnetic radiation with the desired wavelengths and spectral distribution in a consistent and controllable manner.

The following Sections describe three different ways to generate electromagnetic radiation. The first two rely on relatively simple equipment, and can be carried out in a small laboratory. The third an final one requires a large and sophisticated particle accelerator known as a *synchrotron*, but holds the benefit of higher precision and control over a wider range of photon energies than the lab-based sources.

3.2.1. X-Ray Tubes

The simplest and most common way to generate X-rays is by means of the "inverse photoelectric effect" in a so-called X-ray tube. In the typical setup, shown in Figure 3.10a, electrons are generated by thermal emission from a filament inside an evacuated cylinder. The cylinder also contains one or several target materials of typically aluminium or magnesium [54]. A high voltage is applied between the filament (cathode) and the target (anode), accelerating the thermally emitted electrons towards the target. Upon impact, three forms of radiation will be generated. First of all, electrons with most energies will be deflected and hence decelerated by the nuclei of the target material. This causes the emission of photons known as *Bremsstrahlung*[10] radiation to account for the loss in electron kinetic energy [49]. Second, electrons with sufficiently high energy can collide with core level electrons in the target atoms, kicking some of these out to leave vacancies in the inner shells. The subsequent relaxation of the atoms will then produce either *fluorescent radiation* of photons, or Auger electrons, both with energies characteristic of the electronic transition undertaken to fill the hole. Commonly, the incoming electrons are accelerated to an energy sufficient to generate holes in the $1s$ level. This gives rise to several distinct line energies of radiation, corresponding to the allowed transitions into the inner shell of the atomic specie. The two dominating line energies are known as the $K_{\alpha 1}$ and $K_{\alpha 2}$ energies, and arise for transitions from the $2p_{1/2}$ and $2p_{3/2}$ orbitals, respectively. Both transitions are sketched in Figure 3.10b. The energy separation of the two K-lines correspond to the spin-orbit splitting of the p orbitals, and for light elements with small separation they are often viewed as one line $K_{\alpha 12}$ [54]. The $K_{\alpha 12}$ energy line is several orders of magnitude more intense than the spectrum of Bremsstrahlung radiation [49]. This makes it an ideal source of excitation energy that additionally is highly monochromatic. The energy of the $K_{\alpha 12}$ line is $1253.6\,\mathrm{eV}$ and $1486.6\,\mathrm{eV}$ for Al and Mg, respectively [54].

In the typical setup known as a Coolidge tube[11], the filament and target are both kept under vacuum. This is mainly done for two reasons. First, the permittivity of electric field under vacuum is smaller than if gases were present, lowering the probability of electrostatic discharge (i.e. sparking). Second, the inelastic mean free path of the thermionic electron is increased at lower pressure, causing less interaction with residual gas particles in the tube and hence a more stable emission current. A constant water flow is typically circulated through the target material to absorb heat from the collisions and hence prevent the anode from melting [49]. Some X-ray tubes also contain monochromators to filter out specific wavelength from the narrow distribution of X-rays generated, albeit at the cost of radiation beam intensity.

---

[10]After the German word *bremsen* for brake.
[11]After its inventor William Coolidge.
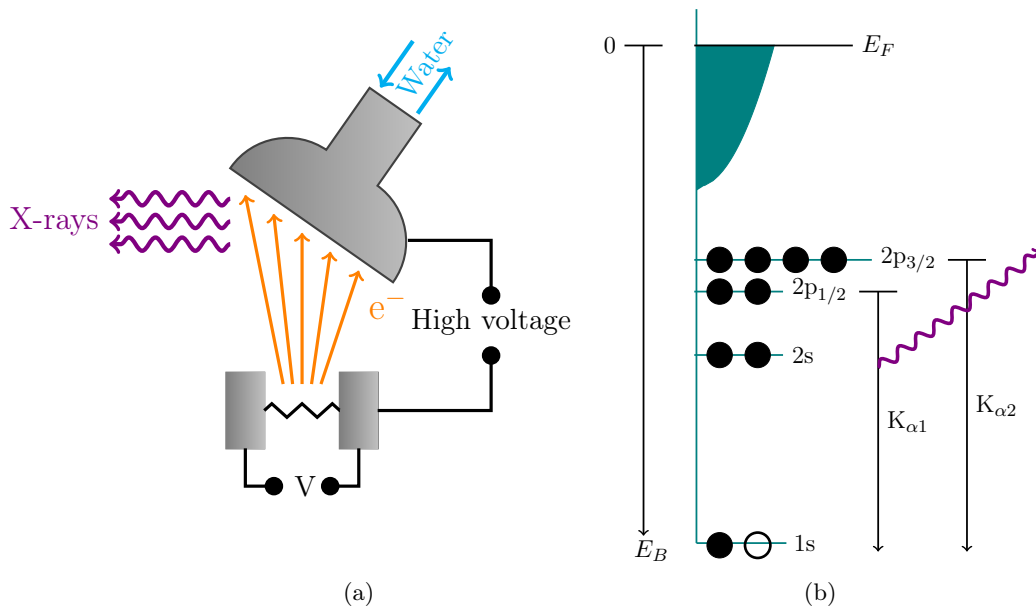
Figure 3.10.: **(a)** Schematic showing the interior of a typical Coolidge X-ray tube. Electrons are thermionically emitted from a filament (cathode) and accelerated towards a water-cooled target material (anode). The incoming high-energy electrons knock out core level electrons from the anode, causing the emission of X-rays as the target atoms de-excite **(b)** Sketch of the electron distribution in Al and Mg after ionization of a $1s$ electron. The two rightmost vertical arrows indicate the transitions than generate $K_{\alpha 1}$ and $K_{\alpha 2}$ line photons, respectively, upon relaxation.

3.2.2. Gas Discharge Lamp

While radiation in the soft X-ray regime ($250\,\text{eV}$ to $\sim 6\,\text{keV}$ [71]) is necessary to fully ionize core level electrons from most atomic species, ultraviolet (UV) radiation ($30\,\text{eV}$ to $250\,\text{eV}$ [71]) is suitable for probing the electronic structure of the more loosely bound valence states near the Fermi level. For lab-based experiments where synchrotron radiation is not available, the most common and easy way to produce UV radiation is by means of a gas discharge lamp [46]. This setup consists of a quartz capillary tube containing a noble gas, with one electrode at either end. Applying a high voltage across the tube accelerates any free electrons present towards the anode. These electrons gain kinetic energy and collide inelastically with the gas molecules in the tube, generating an ionized and excited gas mixture known as a *plasma*. The unstable and excited noble gas molecules will eventually de-excite, emitting photons of discrete energy (and wavelength) corresponding to the specific electronic transitions available in the gaseous specie. Discharge lamps commonly use helium gas with main emission line energies He-I and He-II at $21.2\,\text{eV}$ and $40.8\,\text{eV}$, respectively [53]. The part of the capillary facing the vacuum chamber has a small opening that allows a pressure gradient to be established across the tube and some amount of He

gas to leak inside the chamber. This will somewhat compromise the low pressure inside the analysis chamber, but also reduce the attenuation of the UV light beam prior to hitting the sample.

3.2.3. Synchrotron Radiation

In specific cases, radiation with higher intensity flux and less spectral broadening than what is achievable using conventional X-ray tubes might be needed to meet the resolution requirement of an experiment. As explained in Chapter 3.1.1, the photoionization source and hemispherical analyzer will introduce Gaussian broadenings to all detected line signals, where the amount of broadening is dependent on their design and performance. The broadening from the analyzer ΔE_{an} can be reduced by lowering the pass energy and reducing the sizes of the entrance and exit slits in the energy dispersive direction (see eq. 3.14). However, this will sacrifice some of the signal intensity as $I \propto E_{pass}^2$. The broadening from the photon source $\Delta E_{\hbar\omega}$ is intrinsic to the source design and can only be changed by upgrading our changing the source. Any spectral broadening can be accounted for by introducing a *monochromator* downstream from the source, but this will also greatly reduce the beam intensity flux.

For experiments that need high energy resolution, the solution is therefore often to use *synchrotron radiation*, which essentially is electromagnetic radiation generated from electrons accelerated to relativistic speeds. Modern synchrotron facilities are designed to generate photons of tunable energy from the far infrared to hard X-ray regime, with intensities many orders of magnitude greater than what is achievable from conventional lab sources [78]. This Subsection gives a concise explanation of the fundamentals of synchrotron radiation and how it is generated. Further information can be found in more advanced texts [49, 71, 78].

Synchrotron Rings

Synchrotron radiation is produced by circulating high-energy electrons or positrons at highly relativistic velocities in evacuated storage rings, often called *synchrotron rings*. This section summarizes the main components found along the storage ring, following the text by Willmott [78]. A schematic of a typical synchrotron facility is shown in Figure 3.11.

A beam of electrons, initially emitted from an electron gun[12], is accelerated to roughly $100\,\text{MeV}$ using a *linear accelerator* (LINAC). The electrons are then injected into a *booster ring* where they get further accelerated to the desired velocity before being injected into the main storage ring. Note that all electrons will eventually be lost due to inelastic collisions with residual gas particles in the system, and so new electrons are being supplied periodically to the storage ring to maintain the specified ring current[13].

Inside the storage ring, the beam of electrons is maintained on a closed path using *bending magnets* (BMs). These sit in the arced regions connecting the set of linear paths making up the ring. By applying a magnetic field normal to the velocity vector of the

---

[12]These electrons are most commonly generated by thermionic emission from a heated filament. See Section 3.2.1.

[13]New electrons are typically injected when the ring current drops to about $1 - 1/e \approx 70\%$ of the initial current [78].
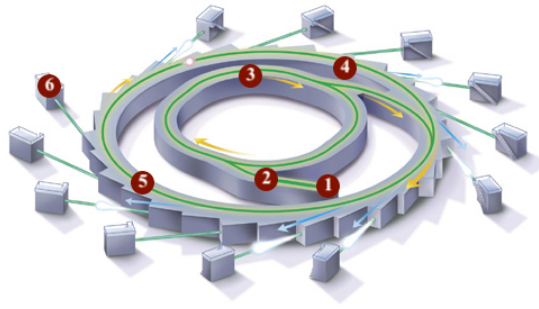
Figure 3.11.: A schematic showing the typical features of a synchrotron facility: an electron gun (1), a LINAC (2), a booster ring (3), a storage ring (4), RF unit/IDs (5) and beamlines leading to various endstations (6). Image courtesy of the Australian Synchrotron [79].

incoming electrons, the charged particles are deflected by the Lorentz force [80], keeping their trajectories along the path of the ring. When accelerated, charged particles will emit electromagnetic radiation [81]. For the deflection of relativistic electrons in a synchrotron, radiation will be emitted in a narrow cone tangent to the path of the particle [71]. The synchrotron radiation is then passed along a *beamline* running tangentially off the arcs where the bending magnets are situated. The beamline consists of several consecutive sections: a *front end* that defines the angular acceptance of incoming radiation and blocks the beam when needed, a set of *optics* and a monochromator that focuses the beam and selects the desired photon energy, and finally an *endstation* where experiments using high-intensity monochromatic photons take place.

A few other key components can be found along the straight sections of the storage ring. Typically, a radio frequency (RF) unit supplies the beam of electrons with enough energy to account for losses when generating synchrotron radiation. Various *insertion devices* (IDs) such as *wigglers* and *undulators* use periodic magnetic structures to cause angular excursions, resulting in a harmonic oscillation of the electrons transverse to the axial direction of the beam. This periodic acceleration will generate photons that are emitted with high intensity flux along the path of the straight sections towards the beamlines. The generation of synchrotron radiation by IDs and BMs are discussed next.

Generation of Electromagnetic Radiation in Synchrotrons

The electromagnetic radiation generated in a synchrotron can be crudely divided into two categories: radiation from the magnetic bending of the electron trajectories, and radiation generated by insertion devices, e.g. wigglers and undulators. The latter carries a higher intensity flux that is typically more useful for analysis than the bending magnet radiation. Nevertheless, the main concepts for both types will be briefly outlined as they are both instructive to help understand the principles and performance of synchrotrons. This discussion is mainly based on the concepts presented in the text by Attwood, and a more elaborate treatment including several proofs can be found there [71].

The high directionality and narrow conical shape characteristic of synchrotron radiation is essentially a manifestation of the Lorentz transformation when relativistic particles are accelerated. In the frame of reference for a point charge moving with average velocity
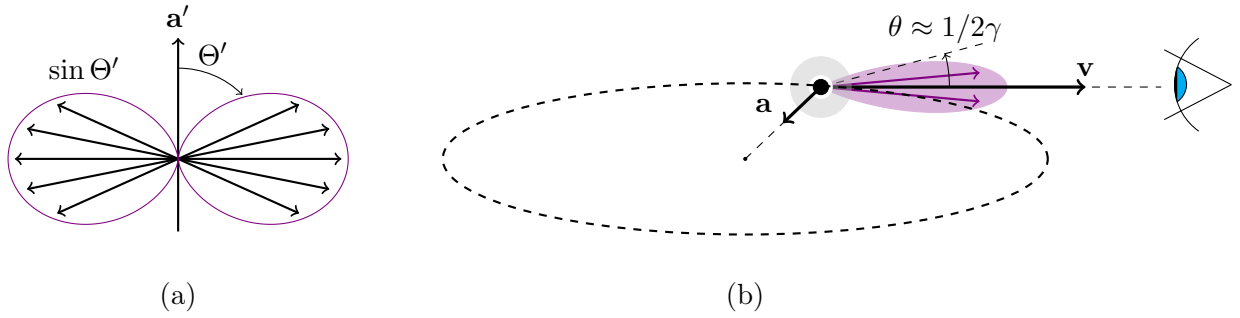
Figure 3.12.: (**a**) Illustration of the two-dimensional radiation pattern from a point charge accelerated by $\mathbf{a}'$. Note that there is no radiation in the direction of acceleration, as seen in the frame of reference moving with the instantaneous velocity of the charge (**b**) Radiation from an electron moving in a circular arc, as seen by an observer at rest (purple) and in the frame of reference of the traveling charge (shaded gray). Note how the toroidal radiation pattern around the electron appears as folded into a narrow cone with half angle $\theta = 1/2\gamma$ when the electron approaches an observer at rest in the laboratory frame of reference with $v \approx c$.

$\mathbf{v}'$, the power radiated by the particle into a solid angle $d\Omega'$ as the charge experiences an acceleration $\mathbf{a}'$ is known to be

$$\frac{dP}{d\Omega'} = \frac{e^2 |\mathbf{a}'| \sin^2 \Theta'}{16\pi^2 \epsilon_0 c^3}, \tag{3.43}$$

where c is the speed of light, ϵ_0 is the permittivity in vacuum, and Θ' is the angle between $\mathbf{a}'$ and the surface normal of the solid angle patch, i.e. the angle to the observation direction $\mathbf{k}'_0$. Equation 3.43 states that power is emitted in a donut shape $\propto \sin \Theta'$ about the direction of instantaneous acceleration $\hat{\mathbf{a}}'$, as illustrated in Figure 3.12a. However, in the reference frame of an observer at rest, the angular Lorentz transformation compresses the angular dispersion of radiation power as seen by the observer. When the relative motion between two frames of reference is highly relativistic, the angle θ from the direction of motion in the observer's reference frame is related to that in the particle reference frame by

$$\tan \theta = \frac{\sin \theta'}{\gamma(\beta + \cos \theta')}, \tag{3.44}$$

where θ' is the angle in the particle reference frame, $\beta \equiv v/c$, and γ is the Lorentz factor given by

$$\gamma \equiv \frac{1}{\sqrt{1-\beta}}. \tag{3.45}$$

Bending Magnet Radiation For the case of bending magnet radiation, the emission as seen by the observer appear as narrow a radiation cone in the forward direction whenever the velocity vector of the centripetally accelerated particle aligns with the observation direction (See figure 3.12b). In this case, the velocity v of the particle in the observer's

reference frame approaches c, i.e. $\beta \rightarrow 1$ and $\gamma \gg 1$. The result is that arbitrarily large emission angles θ' in the reference frame of the approaching electron is folded into a narrow cone with half angle $\theta = 1/2\gamma$ in the "forward direction" as seen by the observer [71]. Bending magnet radiation is hence often referred to as a sweeping "searchlight", resembling the headlights of an approaching train on a circular track.

As alluded to previously, one of the major advantages of synchrotron light sources is their wide range of accessible photon energies. However, synchrotrons are not able to deliver the same radiation flux over the entire range. For bending magnet radiation, a defining parameter that is commonly used to describe this behavior is the *critical photon energy*. This is the photon energy for which half of the radiated power is in higher energy photons and and the other half is in lower energy photons. This is given by

$$E_c = \frac{3e\hbar B\gamma^2}{2m_e} = 0.665 E_e^2 (\text{GeV}) B(\text{T}), \tag{3.46}$$

where B [T] is the magnetic flux density from the bending magnets, m_e is the electron rest mass and E_e is the kinetic energy of the electrons in the storage ring. The intensity flux on-axis by the bending magnet radiation has been shown by Kim to follow the relation [82]:

$$\frac{\text{photons/s}}{\text{mrad}^2 \cdot (0.1\%\text{BW})} = 1.33 \times 10^{13} E_e^2 (\text{GeV}) I(\text{A}) H_2(E/E_c), \tag{3.47}$$

where I [A] is the average current through the ring, $H_2(E/E_c)$ is a modified Bessel function defined by the photon energy normalized to E_c, and the units of relative spectral bandwidth $d\omega/\omega$ is expressed by the factor $(0.1\%\text{BW})$. The characteristic energy profile of the Bessel function is plotted in Figure 3.13a, together with the vertically integrated photon flux $G_1(E/E_c)$. From either functions it is evident that the maximum photon intensity flux is achieved near the critical photon energy. Beyond this point, the intensity falls abruptly, and already at $\sim 4E_c$ the flux is reduced by roughly an order of magnitude.

Undulator Radiation Insertion device radiation is generated when electrons are traversing a periodic magnet structure of moderate field strength, as seen in Figure 3.13b. The periodically switching direction of the magnetic field induces a switching direction of acceleration by the Lorentz force equation that causes the particle to "oscillate" in the direction transverse to its line of propagation along the circular arc. This in turn results in radiation emitted continuously by the electron as it traverses the structure. If the angular excursions are smaller than the characteristic half angle $\theta = 1/2\gamma$ of the bending magnet radiation, the device is known as an *undulator*. On the other hand, angular excursions that are larger than $1/2\gamma$ are caused by insertion devices known as *wigglers*.

In the frame of reference of the moving electron, the particle sees an approaching magnetic structure with a Lorentz contracted period given by

$$\lambda' = \frac{\lambda_u}{\gamma}, \tag{3.48}$$

Where λ_u is the period of the magnetic structure in the stationary frame of reference. This causes the electron to oscillate (in its own frame of reference) like a dipole, and consequently radiate with frequency λ' in directions $\hat{\mathbf{a}}' \cdot \sin \Theta'$ as seen previously from equation 3.43. In the frame of reference of a stationary observer, the frequency of light
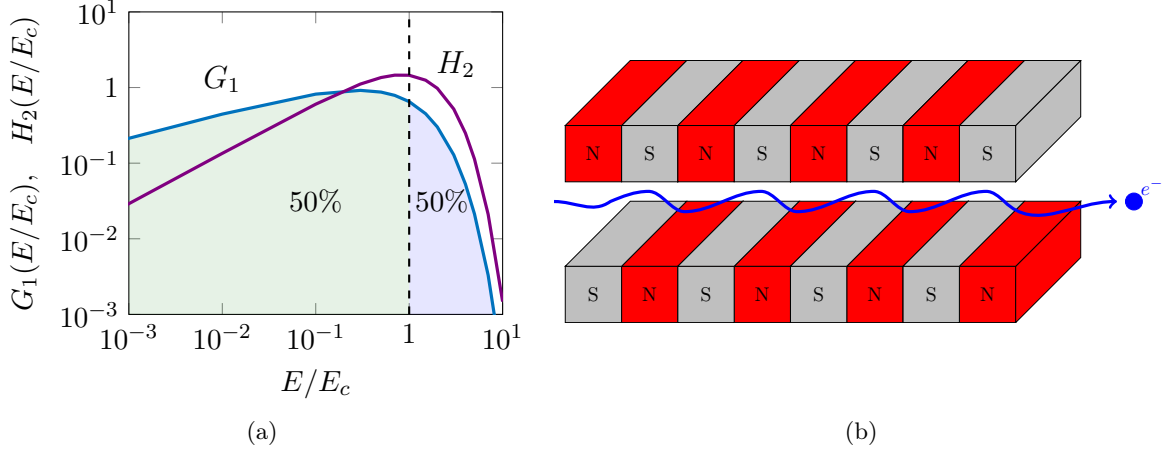
Figure 3.13.: (**a**) Functions H_2 and G_1, describing the on-axis and vertically integrated intensity flux of bending magnet radiation, respectively. Half of the irradiated power will be from photons with $E < E_c$ and the other half from higher energy photons [82]. The intensity of the beam falls abruptly for energies beyond the critical point. (**b**) A typical insertion device for generating electromagnetic radiation in the linear sections of a synchrotron. The traversing electron is accelerated by a periodically switching magnetic structure (illustrated here by opposite magnetic poles N and S) that induces angular excursions in the transverse direction to the forward propagation direction. Narrow cones of radiation are emitted at every turn. For an undulator device, this radiation adds up to a highly intense and coherent cone of half angle $1/(\gamma\sqrt{N})$ in the forward direction, where N is the number of oscillation periods.

emitted from the relativistic electron is Doppler shifted even further. When considering both time dilation and the Lorentz contraction of the emitted wavelength, the observed wavelength in the laboratory frame of reference becomes

$$\lambda = \lambda_u \gamma \left[1 - \beta + \beta \frac{\theta^2}{2} \right] = ... \approx \frac{\lambda_u}{2\gamma^2}(1 + \gamma^2\theta^2), \tag{3.49}$$

where θ is the viewing angle, off axis from the direction of the radiation in the small angle approximation.

Like for the bending magnet radiation, the undulating electron is experiencing an acceleration at normal angle to its main propagation direction. Hence the same folding of the radiation into a narrow searchlight of half angle $\theta = 1/2\gamma$, often referred to as the *natural radiation cone* of synchrotron light, is observed. According to eq. 3.49, the wavelength of the light will increase as the radiation is observed further off axis ($\theta \neq 0$). For resolving narrow features in e.g. NEXAFS or XPS spectra, a monochromator can be applied subsequently to further narrow the radiation cone. If the natural bandwidth of the monochromator is set by the number of oscillation periods N in the insertion device, then the central radiation cone θ_c will have half angle

$$\theta_c \approx \frac{1}{\gamma\sqrt{N}}. \tag{3.50}$$

The discussion can be extended to a beam of traversing electrons, for which the requirement will be that all electron excursions are confined within the half angle θ_c. By considering the electron trajectories over the periodic magnetic structure using the Lorentz force and the appropriate transformations for relativistic electrons, it becomes apparent that the undulation is retarding the "forward" velocity of the electrons in the propagation direction. This reduces the observed wavelength from what was initially suggested in eq. 3.49. Following Attwood [71], the observed wavelength in the laboratory frame of reference can be shown to be

$$\lambda = \frac{\lambda_u}{2\gamma^2}\left[1 + \frac{K^2}{2} + \gamma^2\theta^2,\right] \tag{3.51}$$

with K being the insertion device parameter:

$$K \equiv \frac{eB\lambda_u}{2\pi m_e c} \approx 0.934 \times \lambda_u(\text{cm}) \times B(\text{T}). \tag{3.52}$$

The parameter K also defines the maximum angular excursion $|\theta_{max}| \approx K/\gamma$ of the undulating electrons. The distinction between the two types of insertion devices can hence be made based on K: for large excursions ($K \gg 1$) the device is a wiggler, while for small excursions ($K \leq 1$) the device is an undulator. The flux from the central cone of an undulator is approximately [49]:

$$\frac{\text{photons/s}}{\text{mrad}^2 \cdot (0.1\%\text{BW})} \approx 1.43 \times 10^{14} NI(\text{A}) \cdot \frac{K^2}{1 + K^2/2}. \tag{3.53}$$

Although the equation for wiggler intensity is not exactly the same, this expression still states the general trend that the intensity is dependent on K. As seen from eq. 3.52, K is again dependent on the field strength B and period λ_u of the insertion device. This parameter can be changed if necessary to generate a different intensity profile for the beam. The energy of the radiation is also shown to be K dependent [49]. Note, however, that larger excursions come at the cost of beam coherence. Hence undulators are most commonly used for soft X-ray experiments requiring highly intense coherent light, yet not as intense as what can be produced by a wiggler.

3.3. Ultrahigh Vacuum

As may have become apparent to the reader by now, the ability to work under low pressure is essential to several aspects of this project. Not just in keeping surfaces and interfaces sufficiently clean during depositions or heat treatments, but also during characterization, as all the relevant techniques depend on measuring some signal of electrons either emitted from or scattered off sample surface layers. The interaction of these outgoing electrons with any residual gas molecules in the analysis system will alter their characteristic energies or obstruct their transmission altogether. As for incoming gas particles during e.g. evaporation, any interactions will affect the directionality, flux and cleanliness of the deposition. In the following, the characteristic measures of cleanliness in vacuum environments are described. The most common pumping systems and pressure regimes for work in vacuum are also summarized.

Table 3.1.: The different pressure regimes, their abbreviations, pressure ranges and corresponding mean-free paths (MFPs) of gas molecules [83].

Region name	Abbreviation	Pressure [mbar]	MFP [m]
Low vacuum	LV	300 to 1	10^{-7} to 10^{-4}
Medium vacuum	MV	1 to 10^{-3}	10^{-4} to 10^{-2}
High vacuum	HV	10^{-3} to 10^{-7}	10^{-2} to 10^3
Ultrahigh vacuum	UHV	10^{-7} to 10^{-12}	10^3 to 10^8
Extremely high vacuum	XHV	$\leq 10^{-12}$	$\geq 10^8$
Perfect vacuum		0	∞

3.3.1. Working under Vacuum

In order to achieve sufficient cleanliness and analysis signal intensity, the volume in which the wanted particles move should be essentially "interaction-free". A measure of the required pressure in the chamber can be stated from the mean-free path of molecules l derived in kinetic gas theory [84]:

$$l = \frac{k_B T}{\sqrt{2}\pi \cdot d^2 \cdot P},$$ (3.54)

where d [m] is the molecular diameter, k_B is the Boltzmann constant, T [K] is the temperature and P [Pa] is the pressure of the system. Under atmospheric conditions this distance is on the order of nanometers. At about 10^{-4} mbar it is roughly 50 cm, and if the pressure is reduced to $\sim 10^{-9}$ mbar, the mean-free path will be on the order of kilometers. Hence most experiments in surface science that require little or no interaction is performed in the pressure regime 10^{-7}-10^{-12} mbar, referred to as ultrahigh vacuum (UHV) conditions. Table 3.1 lists the different pressure regimes as defined by Eichmeier and Thumm.

The cleanliness of a vacuum chamber can be further described by the rate at which layers of contamination form on the surface of a sample contained in the system. The incidence rate of residual gas particles is related to the chamber pressure by [85]:

$$r = \frac{P}{\sqrt{2\pi m k_B T}},$$ (3.55)

with m being the molecular mass of the residual gas, in units of the atomic mass constant. At room temperature and with pressures near the upper limit of the *high vacuum* regime ($\sim 10^{-4}$ mbar, see Table 3.1), $r \approx 3.8 \times 10^{16}$ molecules cm^{-2}, corresponding to about 40 contaminant monolayers per second [85].

A slightly different convention is to define the contamination process in terms of *Langmuirs*. One Langmuir, denoted L, describes the formation of one adsorbate layer if a surface is exposed to 10^{-6} Torr for one second [86]. The measure assumes that all incoming residual gas particles will have 100% chance of sticking, and therefore it overestimates the rate at which layers of contamination will form. Nevertheless, it still serves as a decent measure of how long surfaces will stay clean under different vacuum conditions. If for instance the pressure is reduced to 10^{-10} Torr $\approx 1.33 \times 10^{-10}$ mbar, forming 1 Langmuir will take more than 2.5 hours. As typical XPS and XAS experiments can performed within the time frame of a few hours, this states why UHV conditions are commonly required for studies of relatively clean surfaces.

3.3.2. Pumping

Achieving the desired pressure in a vacuum chamber depends on having an external driving force to continuously of periodically trap or exhaust residual contaminants from the system. A multitude of different pumping systems are available, and common UHV setups typically employ more than one. In the following, four of the most common pumps are summarized by their working principles, applications and characteristic working range. More elaborate descriptions of these as well as other pump systems can be found in the texts by Hoffman and Yoshimura [87, 88].

Roughing Pump   A roughing pump is responsible for establishing the initial sub-atmospheric pressure in the vacuum system, and can typically work the pressure down to a rough vacuum of minimum of $\sim 10^{-6}$ mbar. A common type is the *rotary vane pump*, where an inflow of gas into a cavity, or *stator*, is displaced towards an exhaust by vanes attached to a rotating motor. The pump requires lubricating oil to run smoothly, and thus suffers from occasional contamination of lubricant back into the chamber, known as *hydrocarbon backflow*.

Turbo-Molecular Pump   A turbo-molecular pumps consists of several *rotor blades* inside a housing that spin at around $1000-1500$ Hz. Stationary disks, or *stator blades*, are placed in between the rotor blades. Gas molecules entering into the pump gain momentum from impacting the first rotor blade, and are sent through the transfer holes of the adjacent stator into the next rotor blade, gaining a subsequent kick in momentum. This process is continued throughout the housing, and the gas molecule is eventually sent out through the pump exhaust. Modern turbo-molecular pumps are able to bring the base pressure of a vacuum system into the UHV regime, but requires an already established fore-vacuum of $\sim 10^{-3}$ mbar, typically by a roughing pump run in succession.

Ion pump   An ion pump consists of a set of adjacent titanium plates acting as an anode and a cathode. A high potential difference is established between the plates, accelerating free electrons towards the anode that can ionize any residual gas molecules entering the pump. The ionized gas is then accelerated towards the cathode where they get buried into the titanium. An external magnetic field is also applied around the pump to accelerate the ionized particles by the Lorentz force in helical trajectories. This is done to increase the probability of interaction with other gas particles and hence further drive the ionization process. The ion pump requires an already established fore-vacuum in the high vacuum regime ($\sim 10^{-6}$ mbar) to operate efficiently. This base pressure is typically established by a set of successive turbo-molecular pumps and roughing pumps.

Titanium Sublimation Pump   A titanium sublimation pump (TSP) works by periodically spraying gaseous sublimated titanium from a resistively heated filament into the vacuum chamber. The flush of titanium coats the inside of the chamber, forming a thin, reactive layer that will absorb and react with residual gas particles as they hit the chamber walls. The reaction by-products are thus trapped near the solid interface to the vacuum. TSPs are normally applied after establishing a stable pressure in the UHV regime to further condition the gaseous environment when the chamber needs to be extra clean.

4. Experimental Setup and Procedure

The experimental work in this project was carried out in two main sessions at international synchrotron facilities. Initial attempts at heterostructure growth and associated core level studies were performed the ASTRID2 synchrotron beam line of Aarhus University in November 2017. Based on the results obtained from the first beam time, a second study incorporating energy-dependent XPS and angle-dependent NEXAFS measurements at multiple stages in the growth process were performed at the Australian Synchrotron in March 2018. This Chapter explains the experimental setups of the two beam lines, the calibration of their beam energies and how the various evaporators employed in the two experiments were constructed. A thorough explanation of every stage in the experimental procedure ranging from initial sample preparation to finished heterostructure then follows. Finally, the intricate data processing, analysis and quantification of the obtained core level signals from XPS, and angle-dependent resonance features from the NEXAFS is explained.

4.1. Experimental Setup

In the following section, an overview of the two endstations used at ASTRID2 and the Australian Synchrotron is described. Most attention is given to the latter, as the results presented in the next Chapter was mainly aquired there. Finally, an explanation is given on how the Si and Ru evaporators used in either or both experiments were built.

4.1.1. MATline End Station at ASTRID2

The initial photoemission experiments were performed at the MATline endstation of the ASTRID2 synchrotron belonging to the Department of Physics and Astronomy at Aarhus University. This is an end station directed towards low-energy surface studies of condensed matter, capable of supplying a high intensity flux of variable photon energies in the range $20 - 700\,\text{eV}$. Light is generated using a multi-pole wiggler and supplied to the end station through a Zeiss SX700 monochromator. Photoelectrons are detected using a Scienta electron energy analyzer. The high intensity flux of photons at lower energies down to $20\,\text{eV}$ makes the MATline particularly suited for low-energy photoemission spectroscopy like e.g. ARPES and UPS, or probing core levels and absorbtion edges for lighter elements.

The relatively simple end station setup contains a sample load lock connected to the main analysis chamber, allowing sample transfer using a magnetic manipulator arm. Samples are mounted into a five axis manipulator arm inside the analysis chamber, allowing movement in all three spatial directions as well as rotation around the sample surface normal and the in-plane axis. Heating to $\sim 800\,^\circ\text{C}$ is possible by indirect heating from a hot filament. Sample cooling is performed using a liquid nitrogen flow cryostat.
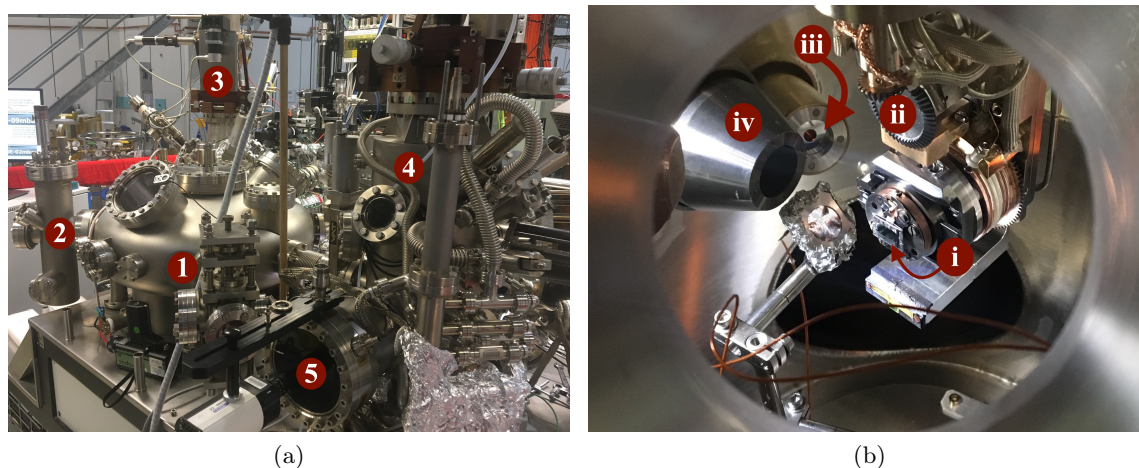
(a)   (b)

Figure 4.1.: (**a**) A partial overview of the experimental setup, showing the radial distribution chamber (1) connected to the sample storage facility (2), analysis chamber with five axis manipulator (3), and a preparatory chamber (4) with a LEED unit (5). (**b**) A sample (*i*) inside the analysis chamber, mounted on a five axis manipulator (*ii*). Incident light from the beamline (*iii*) excites photoelectrons that are detected using a SPECS Phoibos 150 hemispherical analyser (*iv*).

4.1.2. SXR End Station at the Australian Synchrotron

The experiments at the Australian Synchrotron were performed using the *Soft X-ray Spectroscopy* (SXR) end station. Being the only low energy x-ray beam line at the synchrotron, it is equipped with a variable polarization undulator that is capable of supplying light of vertical or horizontal linear polarization, or circularly polarized light of right- or left-handedness. The synchrotron beam is generated by a multi-pole wiggler, supplying high intensity photons in the energy range $90 - 2500\,\text{eV}$ through a monochromator. This makes the SXR an ideal beam line for studying core level for most elements, as well as the absorbtion edges of lighter elements typically present in organic compounds. The end station is set up for and capable of running both XPS and NEXAFS measurements.

The analysis chamber is equipped with a fully automated five axis manipulator, allowing the sample under investigation to be moved in all three spatial directions as well as rotated around the sample surface normal and the axis parallel to the sample plane. The in-plane rotational degree of freedom opens up the possibility to rotate the sample relative to the incoming beam, changing the angle of incidence to achieve angle-dependent XPS and NEXAFS measurements. The spot size of the incoming beam is $15\,\mu\text{m} \times 150\,\mu\text{m}$, and outgoing photoelectrons are detected by a SPECS Phoibos 150 hemispherical analyser. Figure 4.1b shows a snapshot of a sample mounted on the five axis manipulator inside the analysis chamber.

The main analysis chamber is connected to a *radial distribution chamber* (nicknamed UFO) by PREVAC shown in Figure 4.1a. The distribution chamber is in turn connected to a load lock, a sample storage system and a preparatory chamber. The preparatory chamber also contains a fully automated five axis manipulator similar to the one in the

analysis chamber, where samples can be heated to $\sim 1100\,°C$ by direct electron beam bombardment. The chamber also contains a LEED unit and fluorescent screen to study the surface crystallinity of samples, and has several ports available for mounting various evaporators.

4.1.3. Building Ru and Si Evaporators

Depositions at MATline and SXR were done using commercial e-beam evaporators EGCO4 and EBV40A-1 from Oxford Applied Instruments and PREVAC, respectively. In both types of evaporators a desired target material (Si and Ru) in rod form is installed into a chassis, and mounted with its opening facing towards the inside of the vacuum chamber. During deposition, a high current is run through a filament that will emit electrons thermionically. The target material is held at a high potential relative to the filament, attracting the free electrons towards the tip of the rod. Upon impact, atoms get released from the target material and diffuse into the vacuum chamber.

4.2. Sample Preparation

All samples were cut from a 2" 6H-N SiC wafer from TankeBlue Semiconductor into smaller pieces of dimensions $3\,mm \times 7\,mm$ or $10\,mm \times 10\,mm$ using a diamond saw. The smaller samples were primarily used at MATline without intensional shadow masking, while the bigger samples were used during the beam time at SXR for partial shadow masking using Ta foil. The next three subsections describe the cleaning, mounting and masking procedures performed on all the samples investigated during both beam time experiments. All samples were cleaned in two steps: a chemical cleaning step and an in-vacuum flash anneal. For the work performed at MATline, the chemical etching was carried out at the Department of Physics and Astronomy at Aarhus University. For the work at SXR, the cleanroom facilities of NTNU Nanolab and the Melbourne Centre of Nanofabrication (MCN) were used. Flash annealing was performed at both beamline endstations after loading samples into vacuum.

4.2.1. Chemical Cleaning

All cut samples were chemically etched using a modified version of the standard RCA cleaning recipe [89, 90], attempt to remove all native oxides from the sample surfaces. This was done to reduce the number of heat treatments, and possibly also temperatures, needed to achieve clean surfaces subsequently inside the vacuum system.

For both experiments samples were run by the same recipe, but using slightly different concentrations of hydrofluoric acid (HF) for the oxide removal step, as different concentrations of HF were available at the three different facilities. The samples at MATline were treated with a 10% solution of HF, while 12% HF and 10% buffered HF were employed at NTNU Nanolab and MCN, respectively, for the SXR experiments. The following recipe outlines the general chemical cleaning procedure performed at all three facilities. All samples were rinsed in deionized (DI) water and blow-dried using N_2 gas between each new chemical treatment described.

Initially, all samples were immersed in a 96% H_2SO_4 : 30% H_2O_2 (1:1) Piranha solution for 15 minutes to remove any organic residues from their surfaces. Next, dips into HF for

5 minutes were performed to remove all surface layers of native oxide. The samples were then transferred to a $70 - 80 \,^{\circ}\mathrm{C}$ solution of 25% NH_4OH : 30% H_2O_2 : DI H_2O (3:3:10) for further removal of organic contaminants for 10 minutes, leaving a thin layer of new oxide before a second 5 minute HF dip as described above. Final contaminant removal was performed by immersing the samples in an identical Piranha solution for 15 minutes, before a third and final HF dip to remove all remaining oxide and passivate the surface by hydrogen bond termination [91].

Following the final HF dip the samples were rinsed using DI water. They were then either blow dried, packaged and sealed in inert N_2 gas, or left submerged in DI water while being transported to the beamline endstation for mounting onto the appropriate sample holders.

4.2.2. Sample Mounting and Masking

Following the chemical cleaning, all 6H-SiC samples were placed with the (0001) face up on either a polished and ethanol-cleaned Ta sample plate (MATline), or an ethanol-cleaned piece of Ta foil welded onto a larger sample holder (SXR). As seen in Figure 4.2, both samples were attached by wrapping Ta wire or excess Ta foil around the sample edges and welding these towards the back support to keep the samples in place.

The flaps of the Ta foil employed at the SXR (Figure 4.2b) were left intensionally large to provide support while simultaneously covering a significant part of the underlying Si (0001) surface. In this way, the flaps would function as a *shadow mask* for the samples, allowing selective deposition of Ru and Si thin films onto the SiC substrates only in the regions not covered by the foil. The flaps were made so that they could easily be peeled back after the final oxidation step, and re-introduced to the vacuum system to run comparative XPS and NEXAFS of the previously covered and uncovered regions.

After mounting, the samples were quickly moved to their respective beamline loadlock and pumped down to high vacuum ($\sim 10^{-7}$ mbar).

4.2.3. In-Vacuum Cleaning

All samples as loaded were transferred to the preparatory chamber and heated for a second cleaning step in vacuum. This was done to remove any adsorbates or surface oxide formed during the brief exposure to ambient air while mounting onto the sample holders. At the SXR, the loaded samples were initially heated to $\sim 300 \,^{\circ}\mathrm{C}$ for $6 - 8$ hours to allow proper degassing of the sample holders. Two quick ramps to $\sim 700 \,^{\circ}\mathrm{C}$ were then performed by using direct electron beam heating to flash off any remaining oxide layers from the surface. The MATline samples were heated directly to $700 \,^{\circ}\mathrm{C}$ for 10 minutes, with a subsequent 15 minute anneal at $750 \,^{\circ}\mathrm{C}$. Longer anneal times were employed as samples were heated indirectly by means of a hot filament, thus requiring longer time to reach thermal equilibrium. The pre-flash anneal to $\sim 300 \,^{\circ}\mathrm{C}$ was skipped altogether as the MATline sample holders required less time at elevated temperature to properly degas.
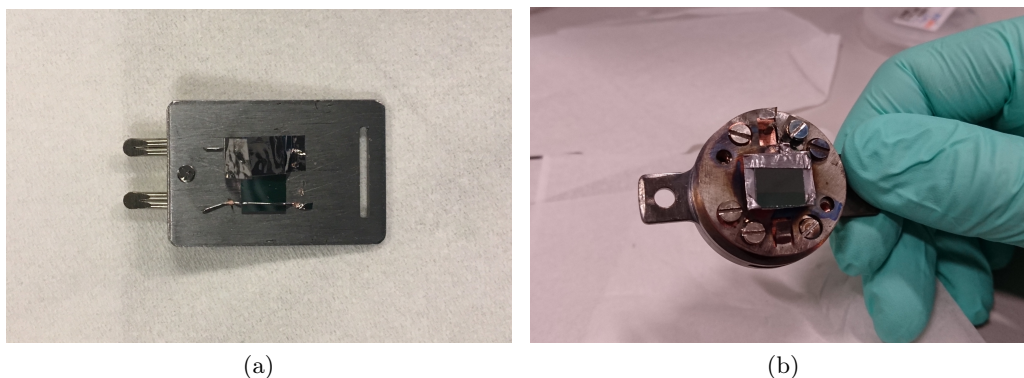
<div align="center">(a)   (b)</div>

Figure 4.2.: Chemically cleaned SiC as mounted with the (0001) face up at **(a)** MATline and **(b)** the Soft X-ray Spectroscopy (SXR) endstations. Both samples have been attached to the underlying sample plate by means of Ta wire or foil. The partial coverage of the sample edges provided by the Ta foil functions as a shadow mask during deposition of Ru and Si in the subsequent processing steps, allowing selective and patterned growth in the exposed regions.

4.3. Sample Growth and Characterization

4.3.1. Clean SiC

Following the anneals, the samples were transferred under vacuum into the analysis chamber of the beamline endstation. At MATline, several scans over narrow windows of kinetic energy were performed with photon energies corresponding to the relevant core levels. For each core level, the position of the sample relative to the detector was adjusted between each scan to optimize the signal-to-noise ratio. At SXR, the photon energy was set to $160\,\mathrm{eV}$ and the position of the sample was adjusted in situ during exposure to maximize the total signal received by the detector. After finding an optimal position, survey scans were performed in a broad kinetic energy range ($0 - 700\,\mathrm{eV}$ at MATline and $0 - 1300\,\mathrm{eV}$ at SXR) to look for possible signs of contaminants. The valence band and each of the core levels peaks Si $2p$, C $1s$ and O $1s$ were then recorded with higher precision.

4.3.2. Graphene Growth

Ru Deposition All clean samples were coated with thin layers of ruthenium under UHV. The ruthenium evaporators were typically degassed within the appropriate chamber[1] for a few hours prior to exposing the samples, with settings similar to the ones used for subsequent deposition to get rid any contaminants from the ruthenium source. This would ensure a sufficiently clean metal film once deposited. The deposition parameters for the two experiments at MATline and SXR are summarized in Table A.3 of the Appendix.

Following the Ru deposition, the samples were scanned for the relevant core levels Si $2p$, C $1s$ and O $1s$, including the new $3p$ and $3d$ core levels corresponding to ruthenium.

---

[1] At the SXR this was done in a designated preparatory chamber, while at MATline the Ru deposition was performed directly inside the main analysis chamber.

The thickness of the metal films were estimated to be in the range $0.7 - 1.5$nm, based on the intensity attenuation of the Si $2p$ signal before and after deposition.

Silicide Formation   All samples were heated to trigger the formation of ruthenium silicide and the associated liberation of carbon atoms to form top layers of graphene. The MATline samples were annealed twice for 10 minutes at $600\,°$C, then $700\,°$C, while the samples at SXR were annealed at $700\,°$C then $800\,°$C for 1 min during each stage. The MATline setup employed *indirect* proximity heating by means of a hot filament, while the SXR setup used localized heating by means of electron beam bombardment to the back side of the sample mounts. In both cases, anneals were performed to trigger silicide formation. Different anneal times and temperatures were assigned due to the different performance of the two heating systems. Using XPS, all the relevant core levels were recorded after each heat treatment to monitor any changes with increasing temperature.

For the SXR samples, NEXAFS spectra were also recorded around the carbon and silicon K-edges after the final anneal. The spectra were taken in PEY mode at multiple incidence angles ranging from grazing incidence ($\theta = 20°$) to normal incidence ($\theta = 90°$). This was done to probe the intensity of the π^* resonance in the hypothesized graphitic surface layers formed during annealing as a function of beam incidence angle[2], in order to reveal the orientation of any such layers relative to the underlying substrate.

4.3.3. Silicon Deposition and Oxidation

In an attempt to intercalate Si under any graphitic surface layers, the SXR samples were exposed to Si in the preparatory chamber while being heated to $\sim 450\,°$C. This would allow more silicon oxide to form in the subsequent oxidation step. Roughly 0.6 nm of Si was deposited on all samples by running the EBV40A-1 evaporator with filament current $I_f = 15$ A for 40 minutes. Following deposition, LEED was attempted to determine the crystalline quality of the surface layers. The samples were then transferred back to the analysis chamber to investigate any changes in the above mentioned core levels. NEXAFS was also performed once again for the K-edges of C and Si at various angles of incidence.

In the final experimental step, samples were exposed to oxygen while heated to intercalate oxygen below the graphene, forming silicon oxide with the underlying layers of Si and $\mathrm{Ru}_x\mathrm{Si}_y$. The MATline samples were heated to $460\,°$C for 1 hour under 9×10^{-7}mbar partial pressure of pure oxygen inside the analysis chamber. The SXR samples were transferred to the loadlock and heated up to $\sim 400\,°$C, before switching off the heating and allowing the samples to slowly cool down while quickly venting the loadlock to normal atmospheric air and pressure.

After oxidation, the SXR samples were taken out of the loadlock to strip back parts of the Ta foil. These were then reloaded into vacuum, and investigated again for changes in the relevant core levels and NEXAFS spectra. Scans were also performed in the regions that had previously been shadowed by Ta foil to compare with the exposed regions. The surface layer crystallinity in both regions were also investigated using LEED. The MATline samples were investigated directly using XPS, without ever being removed from the vacuum system.

---

[2]See Figure 3.8 in Section 3.1.2 for an explanation of the angle definitions.

4.4. Analysis

4.4.1. Photon Energy Calibration

In principle, a synchrotron end station should be able to supply high intensity photons with precise energy on demand within the specified energy range of the beam line. However, the mechanical gears and gear trains that drive the reflective optics selecting the desired photon energy through the monochromator are prone to some lost motion from clearing gaps between the moving parts in so-called *mechanical backlash*. This backlash adds some uncertainty to the actual spatial positioning of the optics that propagate as small yet significant offsets between the demanded photon energy and the one supplied through the monochromator [92]. Such offsets can be reduced to some extent by carefully calibrating the mechanical motion of the gearing system, but never accommodated for entirely. Hence it is customary to run additional scans recording other, yet complementary spectroscopic signal features that will allow offsets from the required photon energies to be calculated.

MATline Energy Calibrations

Each core level signal recorded at MATline was calibrated by subsequently recording the second order light peak of the same core level using the same photon energy as for the principal peak. This method exploits the fact that a certain percentage of the photon flux emitted through the monochromator will carry exactly half the wavelength, or double the energy of the desired first order light. According to equation 3.3, this means a duplicate core level signal of lower intensity will be observed at kinetic energy

$$E_K^{2nd} = E_K^{1st} + \hbar\omega.$$ (4.1)

Hence by carefully identifying common signal features in both spectra, one can extract the actual photon energy $\hbar\omega$ supplied from the kinetic energy offset between the two. The real photon energy can then be re-applied to equation 3.3 to determine the precise binding energy of the features observed in the first order spectrum.

SXR Energy Calibrations

Each core level signal recorded at the SXR was calibrated according to a linear calibration curve, established from the energy offsets of the apparent Fermi edge of the system after Ru deposition. Initially, the Fermi-dirac nature of the valence band maximum (VBM) was verified by defining a Fermi-Dirac function with $k_B T = 25.7\,\text{meV}$ thermal energy[3], and the same center point as the experimental data recorded with $\hbar\omega =100\,\text{eV}$. This function was convolved with a Gaussian profile of $FWHM_G = \left[(\Delta E_{an})^2 + (\Delta E_{\hbar\omega})^2\right]^{1/2}$ to account for any experimental broadening by the hemispherical analyser and the beamline. The convolution was performed using the `gaussfilt(<Ek>,<Intensity>,<sigma>)` function by James Conder, available through the MathWorks File Exchange. After confirming the Fermi-Dirac nature of the VBM recorded with $\hbar\omega =100\,\text{eV}$, the same process was repeated for the VBM recorded with $\hbar\omega =1254\,\text{eV}$. The energy offsets of the two edges from the requested photon energies were then used to construct a linear calibration function

$$\hbar\omega' = a \times \hbar\omega + y_0,$$ (4.2)

---

[3]As expected for a thermodynamic system at room temperature $T = 298\,\text{K}$ [72].

where $\hbar\omega'$ is the actual photon energy received from the beamline when energy $\hbar\omega$ is requested by the user, a is a proportionality constant and y_0 is a constant offset. Equation 4.2 was applied to determine the actual excitation energies for all the experimental spectra, before performing the conversion to binding energy given by equation 3.3.

For the NEXAFS measurements, energy corrections for the different absorbtion edges were performed from simultaneously recorded the absorbtion spectra of known and similar reference materials with each scan. The energy offset of the beam in each case could be figured out by comparing known features in the spectra of these reference materials to literature values. For the carbon K-absorbtion edge, this was done by simultaneously recording the spectra of a bulk graphite reference sample. After finishing the scan, the energy position the strong σ^* resonance in graphite that should be found at 291.65 eV was located in the recorded spectrum [93, 94]. The offset between the recorded σ^* resonance from the graphite film and the literature value could then subsequently be used applied to shift the K-edge in the corresponding sample absorbtion spectrum.

4.4.2. XPS Peak Profile Fitting

Core level signals were fitted using the Levenberg-Marquardt nonlinear least square method available through the Curve Fitting Toolbox$^{\text{TM}}$ in MATLAB. Each relevant peak in the data set was fitted as

$$y_0 + \sum_{i=1}^{N} \left[\Lambda_i PV(x; x_i, ...) + \lambda_i I_i S(x; x_i, \omega_i) \right]. \tag{4.3}$$

Here, the constant linear offset y_0 from the background noise of the scan window is added together with the sum of N peaks PV assigned to different signal features at energies x_i, each with an associated Shirley background S. Each peak P is either a symmetric pseudo-Voigt with parameters α and γ as described by eq. 3.22, or an asymmetric pseudo-Voigt obtained by introducing the Sigmoid from eq. 3.23 into eq. 3.22 along with the rooted sum of squares of α and γ. Λ_i is the cumulative intensity area associated with each peak without the background. The Shirley S of width ω_i is approximated by eq. 3.24 and scaled by a fraction λ_i of the maximum intensity I_i at the signal energy x_i (see Section 3.1.1 for details). All code but the regression tools available through the Curve Fitting Toolbox$^{\text{TM}}$ was written by the author.

Each relevant core level signal was initially fitted with a finite set of peaks based on previous observations in similar experiments from literature, or an educated guess of what signals should be present based on the expected chemical environment on the upper layers of the sample. For each fitting, the quality of the nonlinear least square fit was evaluated and compared to literature where available. Further adjustments, e.g. adding in extra peaks or tweaking fit parameters, were then made to improve the total curve fit to the data set.

For the peaks presented in the next Chapter, several of the peak parameters appearing in equation 4.3 had to be constrained to obtain realistic fits. The following list summarizes the most common constraints induced on the parameters of the pseudo-Voigts:

- The Gaussian widths γ_i for all peaks appearing in the same scan window was assumed to be the same and hence described by one common variable. This can be justified by the fact that the dominant contribution to the Gaussian width of each

signal comes from the photodetector[4]. All signals are received by the same detector, so they should all receive equal contributions from the equipment.

- The ratio of cumulative signal intensities Λ_i for spin-orbit coupled peaks were locked to what was expected from their relative degeneracy of spin states. These ratios are determined by the intrinsic nature of the atoms under investigation, and should not vary with the chemical environment they are present in.

- The relative position of spin-orbit coupled peaks in the intensity vs. energy spectra were coupled by a set energy separation within the precision of their derived literature values [95]. This is justified by the fact that the relative difference in energy levels arising from spin-orbit coupling is set by their response to the intrinsic magnetic pole of the same parent nucleus. Hence the energy splitting of coupled spin orbitals is intrinsic to the atomic specie, and neither this one should change with the chemical environment. The relevant ratios are given in table A.2 of Appendix A.1.

- In most cases, the Lorentzian width parameters were restricted to a lower bound of $0.2\,\mathrm{eV}$ and an upper bound of a few eV. These bounds were set to keep the broadening within what is expected from the physics of the intrinsic excitation processes of the primary spectrum for each line signal.

- Where asymmetric line shapes were expected, the offset parameter b in equation 3.23 was restricted to work within a few eV on the lower end of the kinetic energy of the line signal intensity maximum. This was to properly replicate the physics of minuscule losses to excitations in the valence band that give rise to the characteristic tail of transition metal at *lower* kinetic energies.

- In certain cases, additional restrictions had to be imposed in order to guide the fit function out of local minima towards a better overall fit. To keep the constraints reasonable such restrictions were induced in turn, and each one was carefully evaluated to whether it had produced a better overall fit. In all cases, restrictions of unrealistic physical nature were avoided.

4.4.3. Depth Profiling of Surface Layers

In order to understand the location of the different chemical species present in the samples after the heat treatments, each sample was probed with different photoexcitation energies corresponding to different IMFPs given by eq. 3.5. A compositional analysis was then performed for the C $1s$ and Ru $3d$ core levels based on the signal features observed at various depth of excitation. Two different types of compositional analysis were performed:

1. A manual deconvolution of all line signals for a few selected spectra according to the principles from Section 4.4.2.

2. A MATLAB-scripted compositional analysis that estimated the added intensity of all C $1s$ line signals versus the contributions from species of Ru $3d$.

---

[4]And radiation source for the synchrotron.

The literature values for the binding energies of the C $1s$ and Ru $3d$ core levels revealed that any Ru $3d_{3/2}$ features added from the ruthenium deposition are expected to overlap with or be found in close proximity to the C $1s$ signals [95]. As explained in Chapter 3.1.1, however, both the spacing and area ratio of the two components in the Ru $3d$ doublet is set by the intrinsic properties of the material. This fact was exploited in the manual compositional analysis by deconvolving the Ru $3d_{5/2}$ features first, and then subsequently adding metallic pseudo-Voigts with position and intensity profiles set by their counterparts to the overlapping C $1s$ and Ru $3d_{3/2}$ region.

The scripted analysis was based on the same principles and with a similar work flow to the manual analysis, but simplified to collectively consider the added contributions from Ru versus all C species. Initially, the total intensity of all components in the lower binding energy region at $E_B = 280 \pm 2\,\text{eV}$ was estimated, assuming it to be consisting of Ru $3d_{5/2}$ components only. This was done by first fitting the region with a static Shirley background [68], or a constant linear background if no intensity step was observed. Next, the cumulative intensity of the background-subtracted region was estimated by trapezoidal integration using the built-in `trapz(<Ek>,<Intensity>);` command. The same operation was then performed for a similar $\pm 2\,\text{eV}$ energy window around the combined C $1s$ and Ru $3d_{3/2}$ region at $E_B \approx 284.5\,\text{eV}$. From the estimated intensity of the first region, the amount of signal originating from species containing Ru in the second region was determined using the intrinsic area ratio of the $3d$ doublet listed in Table A.2 of the Appendix. The remainder was then crudely assumed to be coming from C $1s$ signals.

For each sample, the same analysis procedure was performed on a set of thirteen spectra recorded with different photoexcitation energies in the range $\hbar\omega = 325 - 1500$ eV using a `for` loop. Arrays containing intensities for the different components at every excitation energy were then passed to a second script for post-processing and linear regression analysis.

4.4.4. NEXAFS Analysis

All NEXAFS spectra recorded at the Australian Synchrotron were processed using the *Quick AS NEXAFS Tool* (QANT) program macro written for Igor Pro by Gann *et al.* [96]. This analysis program has been developed specifically for the SXR end station and provides instant viewing, photon flux normalization and background subtraction as well as some simple compositional analysis and peak fitting.

Intensity Flux Corrections for Synchrotron Light

As alluded to in Section 3.2.3, synchrotron beamlines suffer from non-uniform flux intensity with varying photon energy. Some of this comes from Lorentz transforming the Doppler-shifted radiation between the frame of reference of the laboratory and that of the relativistic electrons. Another source of irregularity is the build-up of contaminants inside the lens and mirror system of each endstation, particularly consisting of carbon-rich organic compounds. This will have profound consequences when the photons being transferred from the ring through the monochromator carry energies within certain "active" regions of the electromagnetic spectrum corresponding to carbon absorbtion, most notably around the K and L absorbtion edges. The transferred beam will suffer from absorbtion and scattering by these contaminants on its way to the analysis chamber, leading

to an irregular supply of photon intensity that may particularly distort any absorbtion features in the fine structure recorded during NEXAFS experiments.

One way to accommodate for beam flux irregularities is to record some measure of the incident photon flux intensity simultaneously with the NEXAFS spectra. This is typically done using a reference material that partially absorbs some percentage of the photon flux transferred from the storage ring through the x-ray optics and monochromator towards the end station. The NEXAFS analysis setup at the SXR station does this by shining the incoming beam through a biased gold mesh placed upstream from the analysis chamber between the sample and the reflective mirrors. A fraction of the incoming photons will excite electrons from the mesh by the photoelectric effect, generating a measurable current to ground I_0 that is proportional to the incoming photon flux arriving at the end station. An example of such a drain current from the reference grid, recorded in proximity of the carbon K-edge can be seen in Figure 4.3a. Given that the reference grid is sufficiently clean, each NEXAFS spectrum can be corrected for any energy-dependent flux variations of the incoming beam at the time t it was recorded, by scaling it with the simultaneously recorded I_0 spectrum from the grid. The corrected absorbtion intensity as a function of photon energy then becomes

$$\frac{I_s(t_1, \hbar\omega)}{I_0(t_1, \hbar\omega)} \approx C\big[S_{subst}^{sam}(\hbar\omega) + S_{imp}^{sam}(\hbar\omega) + S_{ads}^{sam}(\hbar\omega)\big], \tag{4.4}$$

where S_{subst}^{sam}, S_{imp}^{sam} and S_{ads}^{sam} are the signal intensities from the sample substrate, surface impurities and adsorbate layers, respectively, and C is a constant [70]. This form of intensity flux normalization is known as the *clean monitor method* [97].

It should be noted that this correction is not accurate unless the reference grid is sufficiently clean. Over time, the gold mesh will also suffer from some build-up of carbon-rich contaminants that will in turn affect its photon absorbtion, and hence the drain current I_0. This can be accounted for either by sputter cleaning the grid before any scans are performed, or by a secondary recording of the photon flux in the relevant energy regions using a calibrated photodiode. The spectral response of the photodiode is independent of any surface contaminants, as its photocurrent signal is generated in the bulk of the structure [96]. Hence it can provide a proportionate measure of the photon intensity flux transmitted through the optics of the end station. After each NEXAFS scan the photodiode is introduced in front of the beam, blocking all light transmission completely. A second spectrum of photo-induced current versus photon energy is then recorded consecutively in the same energy region as the previous NEXAFS scan, as seen in Figure 4.3b. If the beam intensity is assumed to remain unchanged with time between the two consecutive scans, the photodiode spectrum $I_{PD}(\hbar\omega)$ can be used to scale the $I_0(\hbar\omega)$ transmission function to accommodate for any carbon contamination on the gold mesh [96].

For all the NEXAFS spectra recorded at the SXR, the corresponding I_0 spectrum and photodiode current were recorded in the same photon energy regions. The spectra were then doubly normalized using the QANT macro to properly scale the intensity of near edge absorbtion features. This correction process is illustrated in Figure 4.4: Each I_0 spectrum is initially corrected for any carbon absorbtion on the gold mesh by dividing it with the corresponding photodiode current spectrum. This produces graph *ii* in the figure. Finally, all raw NEXAFS spectra (*i*) were doubly normalized through dividing them by their corresponding I_0 transmission spectrum corrected by the photodiode (*ii*), to properly scale their near edge absorbtion features, as seen in graph *iii*.
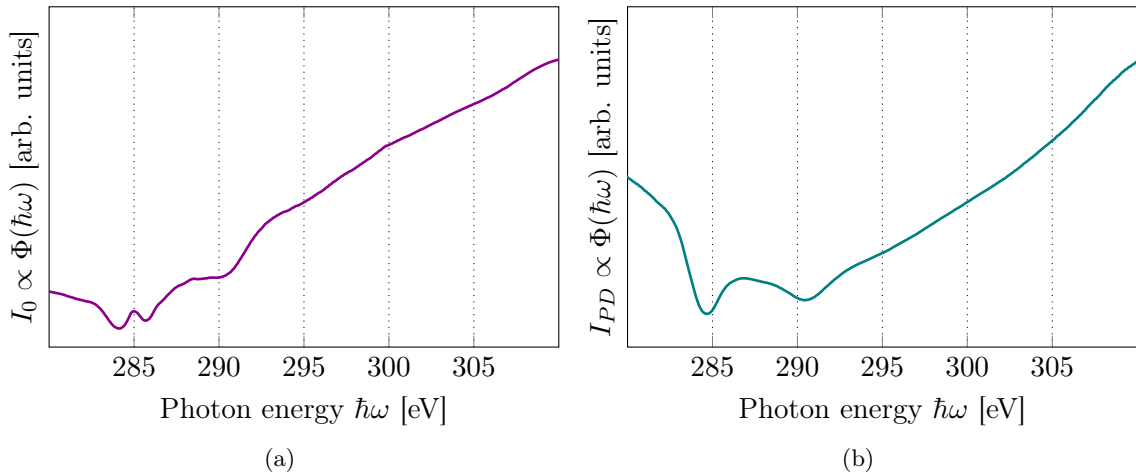
Figure 4.3.: **(a)** An example of a drain current I_0 from the semi-transparent gold mesh, recorded in the expected absorbtion region of the carbon K-edge. **(b)** Photodiode current I_{PD} recorded consecutively in the same energy region. Notice how the varying flux $\Phi(\hbar\omega)$ with energy in both spectra indicate strong absorbtion due to carbonic contamination in the beamline. The different absorbtion behavior of the two comes from additional carbonic contamination allocated on the mesh.
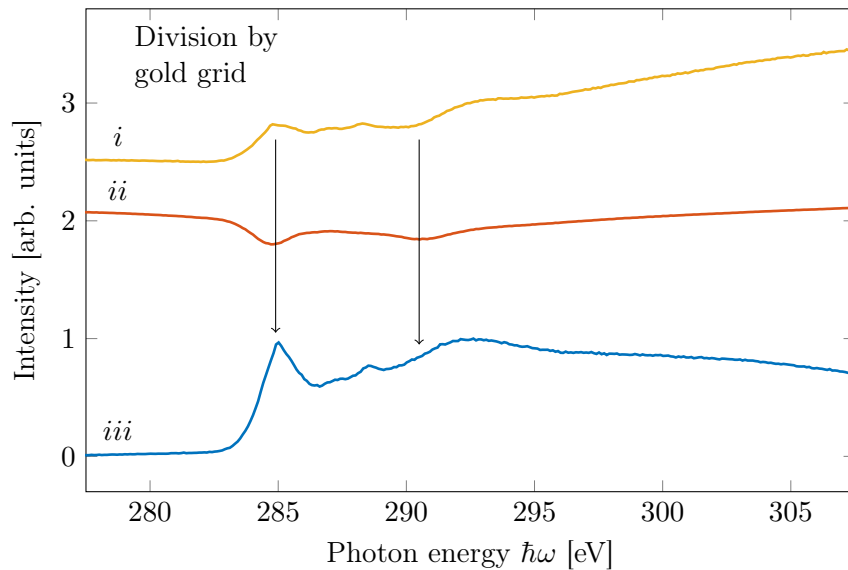
Figure 4.4.: The effects of a *clean monitor normalization* to a PEY spectrum of graphitic carbon on an SiO_2/SiC substrate around the C K-edge. Dividing the raw spectrum (i) by the contamination-corrected drain current from the gold mesh (ii) correctly scales the true resonance features of the absorbtion spectrum (iii). Note that for illustrative purposes, the scaling in the figure has been exaggerated.

5. Results and Discussion

This chapter contains the main findings from the two growth experiments carried out at the synchrotron facilities in Aarhus, Denmark and Melbourne, Australia. The data is divided into subsections assigned to each of the five main stages experiment, ranging from the initially cleaned SiC substrates to the fully finished and oxidized heterostructures.

Rather than presenting the full body of work, this chapter contains only a small, yet representative selection of data obtained at the Australian Synchrotron. This was done in an attempt to present the reader with a concise summary of the main findings and hence ease the discussion. Mainly data that is deemed to reflect the general outcome of each experimental stage is presented. Comparisons between e.g. different sample treatments are made when relevant. The scan parameters for the XPS and NEXAFS data are listed in Appendix A.4.

5.1. Clean SiC

Figures 5.1 and 5.2 contain photoemission data from the surface layers of 6H-SiC mounted with the silicon-rich (0001) plane face-up, following the chemical treatments and heating procedures described in Chapter 4.2. Except for minor variations in the level of surface oxide and adsorbate contamination, all samples prepared at both beam times revealed similar core level signals for the relevant peaks C $1s$, O $1s$ and Si $2p$. The example widescan in Figure 5.1 was taken at the SXR endstation, and chosen because of its superior signal-to-noise ratio.

The widescan reveals the expected line signals corresponding to core levels C $1s$, Si $2s$ and Si $2p$, all three with pronounced and comparable intensities. This is as expected from their stoichiometric distribution in the bulk of the sample and their roughly similar photoionization cross-sections in the kinetic energy range $900 - 1200$ eV of the observed photoemission spectrum [51, 52] (see Figure 3.3 in chapter 3.1.1). The small, yet pronounced features in the vicinity of the line signals to higher binding energies have been assigned to the generation of plasmons as photoelectrons escape the sample into vacuum.

The spectrum also reveals some level of oxygen and sodium contamination from the presence of the O $1s$ and Na $1s$ signals and their corresponding Auger peaks. The former is not surprising, and may well originate from the exposure to air before loading the sample(s) into vacuum. This would lead to the formation of a few atomic layers of surface oxide under ambient conditions of temperature, pressure and humidity, despite what would appear as sufficient chemical cleaning beforehand[1]. The subsequent flash anneals to $700\,°C$ were performed in an attempt to remove some of the native oxide layers formed due to air exposure during mounting. However, a full removal of all traces of oxide would require a

---

[1]Raider *et al.* found that ~ 1 hr of air exposure in laboratory conditions resulted in $2 - 3$ Å of silicon oxide on HF-etched silicon surfaces [98]
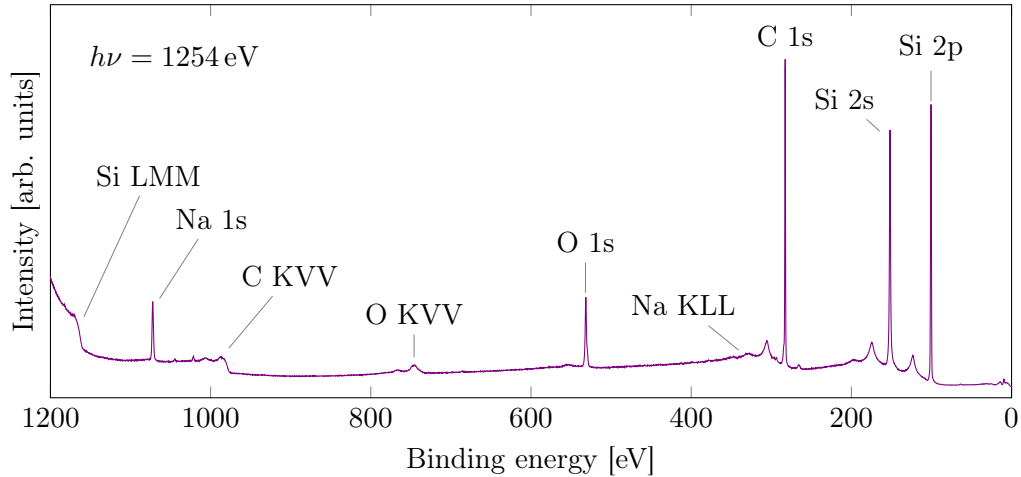
Figure 5.1.: Widescan of a 6H-SiC sample studied at the Australian Synchrotron. Scan was performed after chemical RCA cleaning, an overight anneal at $\sim 320\,°C$ and two flash anneals to $700\,°C$. The relevant core level and Auger peaks have been denoted.

sample temperature of $\sim 1050\,°C$ [99], and was avoided as this could trigger an unwanted $(6\sqrt{3} \times 6\sqrt{3})\text{R}30°$ reconstruction of the 6H-SiC(0001) surface [100, 101].

The presence of sodium is more surprising, but likely to originate from residual contamination left in the vacuum system of the experimental setup. Later investigations by the beamline scientists at SXR revealed that the previous user had made extensive use of Na evaporation in the same prep chamber as where the SiC samples were annealed. This is likely to have resulted in some traces of sodium left in the chamber that may well have adsorbed onto the samples following the flash anneals. Note that the intensities of the oxygen and sodium line signals relative to those of carbon and silicon are somewhat deceiving, and cannot be directly translated into relative levels of contamination as the cross-sections of O $1s$ and Na $1s$ are roughly $3\times$ and $8\times$ that of C $1s$, respectively, at photon energy $1254\,\text{eV}$ [51].

Figure 5.2 contains the core level signals of O $1s$, C $1s$ ad Si $2p$, deconvolved to reveal the contribution of the various chemical states present to the overall line signal. Each core level was recorded with a different photon energy, yet corresponding to the same kinetic energy $E_k \approx 60\,\text{eV}$ for outgoing photoelectrons based on their approximate binding energies stated in literature [95]. According to equation 3.5, this E_k corresponds to an inelastic mean-free path of $4.5 - 5$ Å, meaning that the signal received is from the topmost $7 - 12$ atomic layers of the sample[2]. The reader should note that from here on, the majority of all core levels presented will be with excitation energies corresponding to this set of layers. The exception is the set of scans presented in subsection 5.3.3, where higher excitations are made use of to probe deeper structures in the samples.

The Si $2p$ spectrum reveals one central feature around $101\,\text{eV}$, with an asymmetric tail towards higher binding energies. The core level can be resolved into four doublets, where

---

[2]Based on the interlayer distance $\delta \approx 2.52$ Å between consecutive layers of Si in 6H-SiC along the [0001] stacking direction [102], and assuming a cut-off when the intensity is reduced to $1/e^3 \approx 5\%$ according to eq. 3.25. This stacking was shown in figure 2.4 of Chapter 2.4
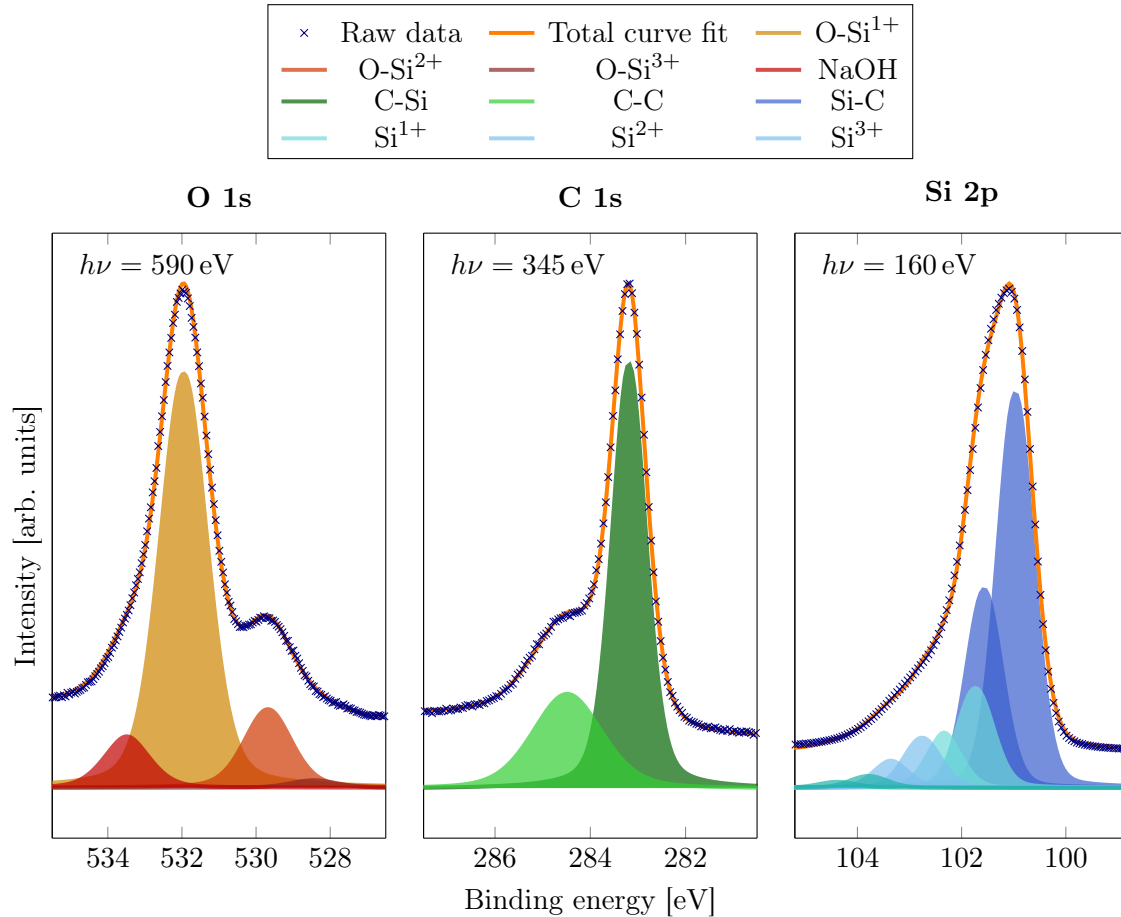
Figure 5.2.: Deconvolved photoemission spectra for core level signals O 1s, C 1s and Si 2p, coming from the Si-rich (0001) face of a chemically cleaned and flash-annealed 6H-SiC sample. The excitation energies of the probe correspond to signals received from the topmost $7 - 12$ atomic layers of the sample.

each pair corresponds to a different chemical state in silicon. Each doublet has been fitted with an intrinsic energy separation of 0.6 eV [103], and an intensity area ratio of 1 : 2 as expected for the spin-orbit-splitting of spin-up and spin-down states in the 2p orbital (see Appendix A.1). The 2$p_{3/2}$ signal of the main component is found at binding energy 101.0 eV, roughly 0.6 eV lower than what is expected for SiC in the bulk [104]. However, similar line signals were observed by Qin *et al.* in ~ 5 nm thin films of SiC, suggesting it to be silicon bonding to carbon in the surface layers of the sample [105]. The other three doublets are found at binding energies +0.8 eV, +1.8 eV and +2.8 eV relative to the Si-C signal. This is roughly what is expected for intermediate oxide states of Si atoms each bonding to one, two and three oxygen atoms (Si^{1+}, Si^{2+} and Si^{3+}), respectively [106, 107].

The C 1s spectrum is deconvolved into two components: one main component at binding energy 283.2 eV and a smaller, broader component at 284.5 eV. The former is shifted towards lower binding energy by 0.4 eV relative to the bulk component of pure SiC [108], but the same behavior has been observed before in n-doped 6H-SiC samples and attributed to a Fermi level pinning above the top of the valence band [109, 110]. The same binding

energy was also observed by Qin in the previously mentioned 5 nm thin films of SiC. The component at 284.5 eV sits in the viscinity of where neutral graphite or graphene weakly interacting with an underlying substrate ($\sim$284.4 eV) is expected to appear in later stages of the experiment [41, 108]. However, the preceding anneals to 700 °C should be insufficient to trigger any graphitization from the pure substrate, as the $(6\sqrt{3} \times 6\sqrt{3})$R30° surface reconstruction is first observed at temperatures > 1000 °C [104]. It should, however, be sufficient to remove organic contamination from the surface [111]. Hence the signal is assumed to come from non-stoichiometric carbon in the crystal near the (0001) surface plane reconstructively bonding with itself due to the broken symmetry or imperfections in the crystal.

The O 1s signal is deconvolved into four components with a central feature at 531.9 eV. Based on the likeliness of surface oxides indicated by the Si 2p spectrum, this feature and the tail of two components at lower binding energies 529.7 eV and 528.4 eV are assigned to O bonding with Si^{1+}, Si^{2+} and Si^{3+}, respectively. Note how the relative chemical shifts of the different sub-oxide forms is consistent with what is expected from increasing levels of oxidation (see Chapter 3.1.1). The fourth feature at 533.5 eV is assumed to be an oxidized form of the sodium residues visible in the widescan. The binding energy of the feature is found within 0.2 eV of what is expected for NaOH [112], which may have formed from interaction with oxygen following the flash anneals in an insufficiently clean vacuum environment.

5.2. Ruthenium Deposition

Following the deposition of ruthenium, several new features that can be related to the core levels and Auger decays of the deposited metal become visible in the survey scan [95]. All preexisting features from the clean SiC are collectively attenuated, suggesting that the metal is situated in a layer on top of the substrate. An example widescan taken with $\hbar\omega = 1254$ eV after deposition of 1.5 nm Ru is shown in Figure 5.3. The thicknesses of the Ru layers deposited were estimated to be 0.7, 0.9 and 1.5 nm using eq. 3.25 and the relative intensities of the Si 2p signals before and after deposition.

Figure 5.4 shows some of the core level signals obtained for C 1s, Ru 3d and Si 2p. For Ru thicknesses of 0.7 nm and 1.5 nm, the intensities of the Si 2p spectra were reduced to $\sim 20\%$ and $\sim 4\%$, respectively, of their original signals. No new components were visible in Si 2p spectrum, but the intensities of the sub-oxides relative to the Si-C signal increased with deposition. This suggests that more oxide was formed and that the deposition may have been prone to some contamination from the e-beam source. The presence of more oxygen was confirmed from an increase in the relative intensity of O 1s to Si 2p between the widescans in Figures 5.1 and 5.3. Seen also is a collective shift of -0.4 eV towards lower binding energies for all components in the Si 2p spectrum. This is likely to be an artifact of charge doping from the electron-rich transition metal on top of the substrate. The same shifts and attenuation where observed in the data from both the MATline and SXR experiments.

The spectra for C 1s and Ru 3d reveal several new features related to both the metal and new chemical species of carbon. The signal at binding energy 280.0 eV for the thick layer sample matches the literature value for the 3$d_{5/2}$ component of clean bulk Ru [113]. An equivalent signal is located at 280.15 eV for the sample with the thinner 0.7 nm Ru
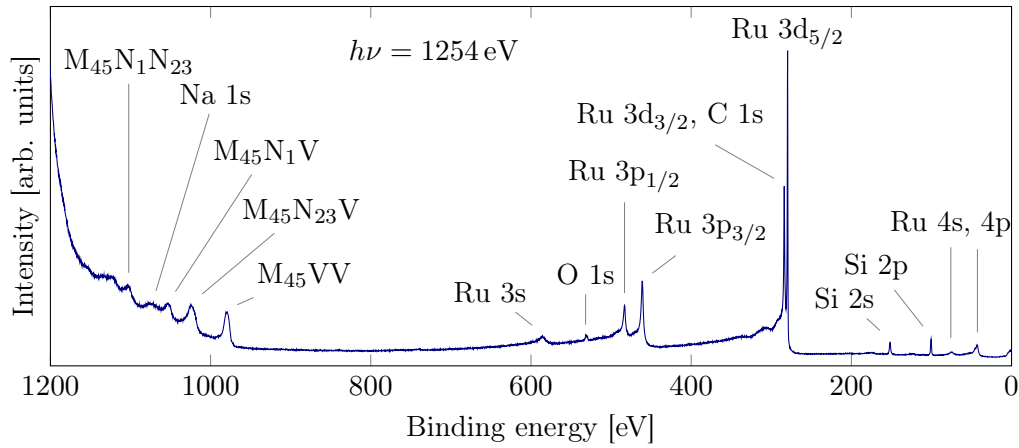
Figure 5.3.: Widescan of a 6H-SiC sample after deposition of 1.5 nm Ru. The intensities of the preexisting features from Figure 5.1 have been greatly reduced, and visible are new core level and Auger components originating from the Ru.
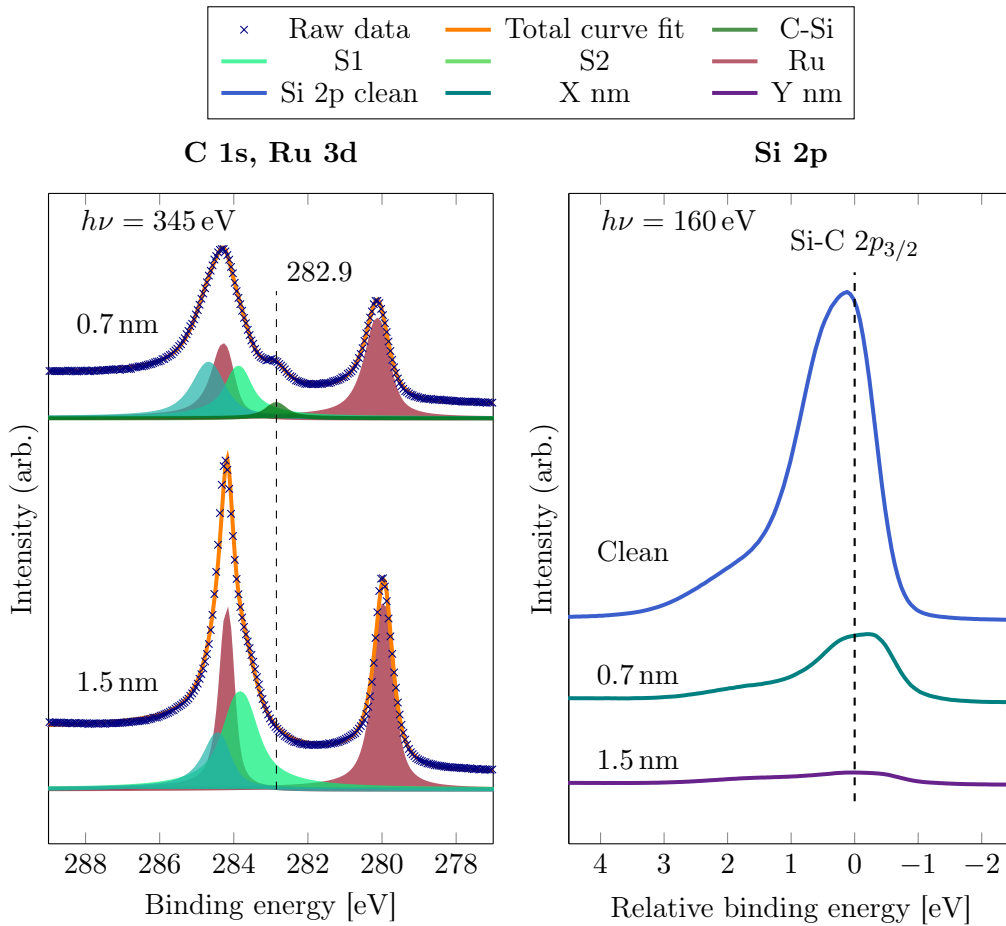

Figure 5.4.: Deconvolved photoemission spectra for core level signals C $1s$ and Ru $3d$ (left), and the intensity attenuation of the Si $2p$ signal (right) following the deposition of 0.7 nm and 1.5 nm of ruthenium.

layer. For the former and latter, the $3d_{3/2}$ component of the doublet is located at $+4.23\,\text{eV}$ and $+4.17\,\text{eV}$, respectively. This is within the range of observed Ru $3d$ splittings found in literature [95, 114–116]. Both doublets have been fitted using the asymmetric pseudo-Voigt approximation to the Mahan function outlined by Schmid *et al.* [59], and with a $3:2$ intensity area coupling according to the relative degeneracy of the $3d_{5/2}$ to the $3d_{3/2}$ orbital states (see Appendix A.1). The $3d_{3/2}$ component of the ruthenium doublet is seen to overlap with the preexisting C $1s$ features from the substrate. A strongly attenuated bulk SiC component can be observed shifted to binding energy $282.9\,\text{eV}$ in the $0.7\,\text{nm}$ sample, while for the $1.5\,\text{nm}$ sample this feature can no longer be resolved. The previously observed C-C component at $284.5\,\text{eV}$ is clearly also buried under the Ru in both samples.

Two new carbonic line signals S1 and S2 also appear at at higher binding energies relative to C-Si: $+1.0\,\text{eV}$ for S1 and $+1.6\text{-}1.8\,\text{eV}$ for S2, respectively. Based on their intensities relative to the substrate C signal, these are likely to be related to the formation of the SiC/Ru interface. In some works, the S2 peak has been interpreted as C-C bonding in an Si-depleted interfacial region of SiC [104, 109, 110]. Features with similar energy offsets from bulk C-Si as the ones described have also been observed in reconstructions of the Si-rich top layer for epitaxial few-layer graphene grown on 6H-SiC(0001) [108, 117]. As previously pointed out, no surface reconstruction is expected for the samples when subjected to temperatures $< 1000\,^\circ\text{C}$. However, ruthenium, like many other transition metals, has proven to be a highly reactive reducing agent even at room temperature [118, 119], and may well have absorbed or bonded with some of the top-layer Si, or even the C in the second atomic layer from the substrate. This would give rise to intermixed interfaces with compositional gradients perpendicular to the growth direction of the metal film. Ruthenium is known to readily bond with carbon, as seen in organic complex molecules, where its $3d_{5/2}$ core level is observed to shift by $0.1 - 0.9$ eV towards higher binding energies [120]. Pasquali *et al.* also reported that the binding energy of Ru on n-type Si(001) substrates decreases with increasing thickness of the overlying Ru up to about $15-20$ monolayers (MLs), where the topmost layers of the film become essentially metallic [121]. If the overlying Ru film is donating electrons by forming Ru-Si or Ru-C bonds in the interface region, this could well explain the $+0.15\,\text{eV}$ binding energy of the $0.7\,\text{nm}$ thin Ru layer relative to the thicker, and hence more bulk-like, $1.5\,\text{nm}$ Ru layer.

5.3. Silicide Formation and Graphene Growth

5.3.1. 700°C Anneal

Following the anneals to $700\,^\circ\text{C}$, new resonance features appear near the absorption edge of C $1s$. Figure 5.5 shows the intensity- and energy-normalized NEXAFS spectra for two samples with initial Ru thicknesses $0.7\,\text{nm}$ and $1.5\,\text{nm}$ at grazing $(\theta = 20^\circ)$ and normal $(\theta = 90^\circ)$ incidence of the linearly polarized photoexcitation beam at SXR. The two distinct resonance features located at energies $285.5\,\text{eV}$ and $291.7\,\text{eV}$ correspond well with the expected resonances for the $1s \to \pi^*$ and $1s \to \sigma^*$ transitions characteristic for sp^2 hybridized C atoms [73, 122]. The fact that neither features could be resolved at the previous stages of the experiment suggests that new layers of graphitic carbon have been formed as result of the heat treatment. The resonance intensity of the transition to the unoccupied π^* states also increases drastically as the angle of incidence θ for the incoming
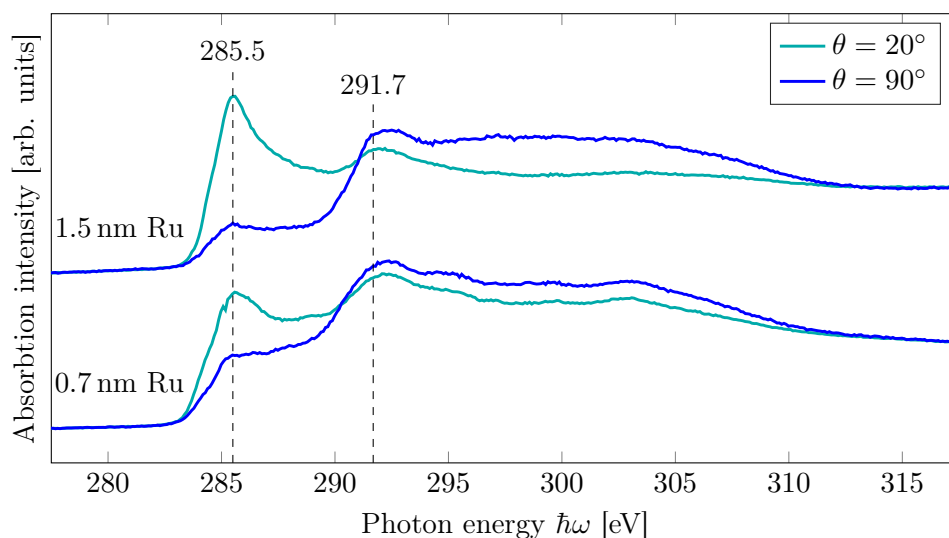
Figure 5.5.: X-ray absorbtion in the viscinity of the carbon K-edge for samples covered with 1.5 nm (top) and 0.7 nm Ru (bottom) following 1 minute at 700 °C. Resonance features at 285.5 eV and 291.7 eV, corresponding to the C 1s π^* and σ^* transitions, respectively, are visible for both samples. The π^* resonance intensity increases as the incoming radiation moves to grazing incidence (20°).

radiation is moved to grazing incidence. The resonance is strongest when the dominant field vector $\mathcal{E}_{||}$ of the linearly polarized beam ($\mathcal{E}_{||} \gg \mathcal{E}_\perp$) is roughly parallel to the sample surface normal. Hence the graphitic layers must have a vector **O** for the transition that is almost parallel to $\mathcal{E}_{||}$ in this configuration (see Figure 3.8 for an explanation of the experimental geometry). This indicates that the layers of sp^2 carbon are more or less parallel to the basal plane of the substrate.

Silicon Core Levels

Figure 5.6 shows the deconvolved Si $2p$, C $1s$ and Ru $3d$ core levels for the samples initially coated with 0.7 nm and 1.5 nm ruthenium after a 1 minute flash anneal to 700 °C. Several new features have appeared at binding energies lower than the familiar Si-C signal at 101.0 eV. The total intensity of the Si $2p$ region when subtracting the background has also increased with the anneal. As no new material was added to the system externally, this suggests that Si atoms from the bulk substrate have been liberated and diffused into the surface layers probed by any outgoing photoelectrons with $\lambda = 4.5 - 5$ Å. This is supported by how the fractional intensity of stoichiometric SiC signal changes from $\sim 48.4\%$ to $\sim 5.6\%$ with annealing for the sample coated with 1.5 nm Ru. A clear broadening is observed for the Ru $3d_{5/2}$ signal, indicating that the chemical environment of the Ru atoms in the top layers has changed.

The lower binding energy Si $2p$ components appear in an energy range that is commonly associated with different stochiometries of ruthenium silicide [41, 103]. The new signal can be deconvolved into three components, assumed to represent three different phases of ruthenium silicide that are stable at room temperature. All three components have been fitted with symmetric pseudo-Voigts of area ratio 2 : 1 between the $2p_{3/2}$ and $2p_{3/2}$

Table 5.1.: Experimentally determined binding energies and fit parameters for the new core level features in Figure 5.6.

Peak	E_B (1.5 nm / 0.7 nm) [eV]	Doublet sep. (1.5 nm / 0.7 nm) [eV]
Si1 $2p_{3/2}$	99.1 / 99.3	0.6 / 0.6
Si2 $2p_{3/2}$	99.6 / 99.9	0.6 / 0.6
Si3 $2p_{3/2}$	100.5 / 100.6	0.6 / 0.6
Ru1 $3d_{5/2}$	279.7 / 279.9	4.2 / 4.1
Ru2 $3d_{5/2}$	279.5 / 279.7	4.1 / 4.2
Ru3 $3d_{5/2}$	279.4 / 279.6	4.1 / 4.2
Ru4 $3d_{5/2}$	280.6 / 280.6	4.2 / 4.2
C (sp^2) $1s$	284.3 / 284.3	N/A
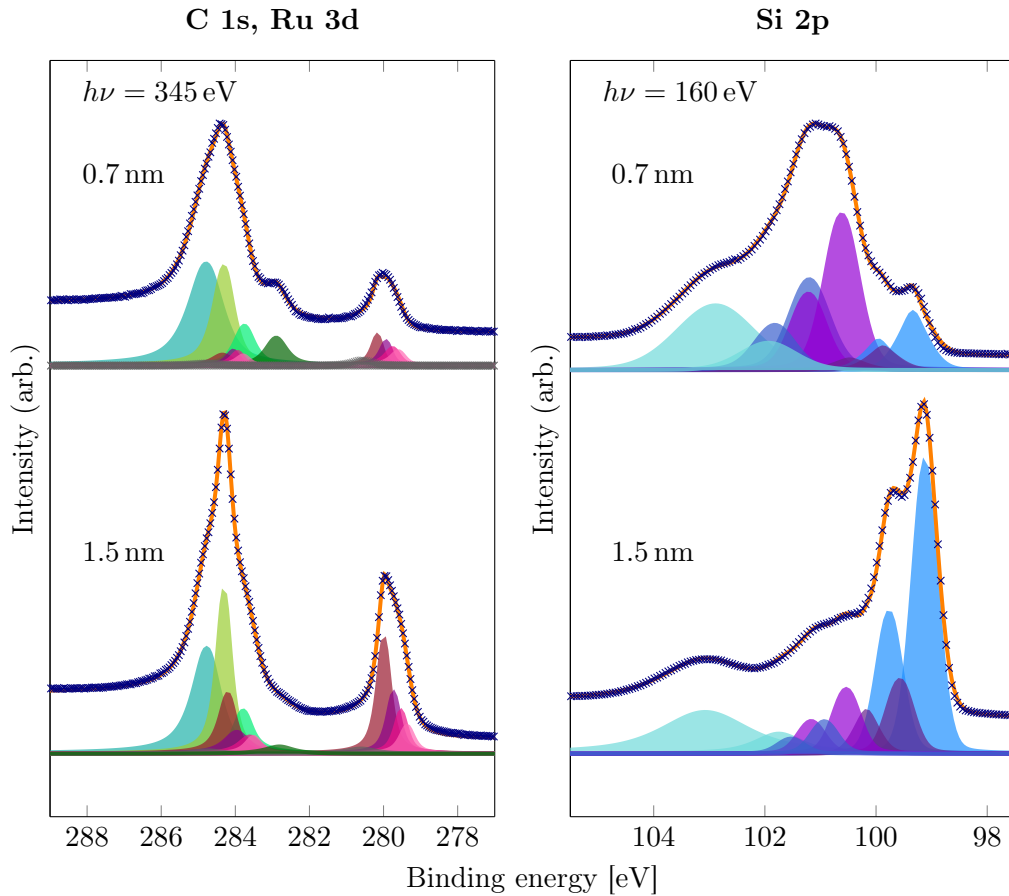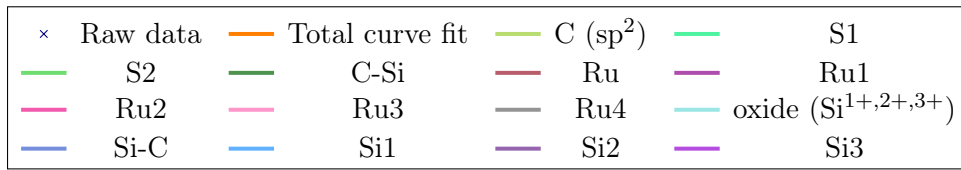
Figure 5.6.: Deconvolved C $1s$ and Ru $3d$ signal after the thermal treatment to 700 °C for 1 min. New features triggered by the anneal are now visible for both samples.

components, and a fixed splitting of 0.6 eV that is commonly observed for Si2p in silicide phases [103, 123]. The formation of epitaxial ruthenium silicides has previously been reported under high vacuum for temperatures starting at 300 °C, with thermally stable silicides forming around 700 °C [121, 124]. Several stoichiometric phases are expected to occur with heat treatment: Lizzit *et al.* reported two distinguishable phases from the core level spectra of both Si 2p and Ru 3d, while Chang and Chou identified three different phases by means of electron diffraction and transmission electron microscopy (TEM) [41, 124]. However, as addressed by Jelenković *et al.*, the data about the binding energies of specific silicide phases is very limited . The same group made attempts to identify the binding energies related to Ru$_2$Si$_3$, which was expected to be the most stable phase formed at elevated temperatures above 600 °C [123, 124]. The identified Ru$_2$Si$_3$ phase, as confirmed by TEM measurements, was found at binding energy $E_B = 99.4$ eV, which is closest to the component denoted as Si1 in this experiment. The binding energies of all new components in Figure 5.6 and their doublet separations (where applicable) have been summarized in Table 5.1.

Carbon and Ruthenium Core Levels

Based on the new features seen in the Si 2p spectrum, three new doublets of Ru: Ru1, Ru2 and Ru3, were fitted to the C 1s + Ru 3d spectrum after annealing. These are situated at lower binding energies relative to the preexisting Ru doublet identified after metalization (see Figure 5.4). Note that similar features were resolved from the Ru 3d by Lizzit, with binding energies matching those of Ru1 and Ru3 in the 1.5 nm sample. Some metallic Ru is still seen in both samples, with a highest amount in the sample previously coated with a thicker 1.5 nm layer. If the 1 minute anneal to 700 °C is enough to produce a finite amount of silicide, then more metallic ruthenium should be observed in the thick layer sample after the same heat treatment.

A fourth additional feature is detected at higher binding energy $+0.6$ eV relative to the metallic Ru 3$d_{5/2}$ signal. This small signal is expected to come from tiny amounts of RuO$_2$ near the surface of the sample [125]. The presence of more oxygen after annealing can also be confirmed from the increase to 2.7× intensity for the silicon oxide peaks. All five ruthenium doublets have been fitted according to the asymmetric pseudo-Voigt approximation (see Chapter 3.1.1), with fixed intrinsic area ratio 3 : 2 between the 3$d_{5/2}$ and 3$d_{3/2}$ component of each doublet. Energy separations within each pair has been allowed to drift within the $4.1 - 4.2$ eV window found in literature [95, 123]. The binding energies and peak separations are summarized in Table 5.1.

The C 1s + Ru 3d spectra in Figures 5.4 and 5.6 reveal that the heat treatment has caused a shift of signal intensity towards the higher binding energy region associated with C 1s and Ru 3$d_{3/2}$. The added intensity to this region cannot be accounted for by the Ru 3$d_{3/2}$ signals alone for two reasons. First of all, the Ru 3$d_{3/2}$ signals are coupled in intensity to the lower binding energy Ru 3$d_{5/2}$ signals, set by the relative degeneracy of the quantum mechanical spin states. Second, the added Ru 3$d_{5/2}$ signal in both samples have decreased with the anneal. Hence any added intensity to the C 1s and Ru 3$d_{3/2}$ region must come from the appearance of new core level signals, or an intensity increase of the preexisting C 1s signals. Deconvolving the region reveals five Ru 3$d_{3/2}$ peaks as expected, and the familiar carbon peaks S1, S2 and C-Si the same binding energies as before. Note that a faint bulk signal is now also observed for the 1.5 nm sample. In

addition, both samples appear to have one new, sharp and slightly asymmetric carbon component at 284.3 eV. The binding energy of this peak is 0.1 eV lower than what is expected for sp^2 hybridized carbon in neutral graphite [108], or weakly interacting few-layer graphene (FLG) as observed by Lizzit [41]. This is in accordance with the presence of graphitic carbon already indicated by the strong σ^* and π^* resonances in the NEXAFS spectra of Figure 5.5. The new sp^2 component thus indicates the liberation of C atoms and subsequent graphitization from transition metal silicide formation, hypothesized in Chapter 2.4 and observed previously by Cooil *et al.* when annealing Fe films on 6H-SiC [36]. Notice also how the relative intensity of the S2 peak to the S1 peak has increased with annealing. Based on the hypothesized origin of the S2 peak in section 5.2, this may well be coming from further consumption of substrate Si atoms in forming the new silicides.

5.3.2. 800°C Anneal

Subsequent heat treatment of the 1.5 nm layer sample leads to even stronger resonance intensities for the characteristic $1s \rightarrow \pi^*$ and $1s \rightarrow \sigma^*$ transitions in the vicinity of the carbon K-edge. Figure 5.7 shows the angularly resolved NEXAFS spectra for the 1.5 nm layer sample after a second anneal to 800 °C for 1 minute. Steps of $\Delta\theta = 10°$ ranging from grazing (20°) to normal (90°) incidence of the beam has been included to clearly illustrate the angular dependence of the two resonance features. The π^* resonance is shifted to 285.4 eV with the second anneal. As the electric field of the linearly polarized beam aligns with the surface normal of the sample, a sharper and more pronounced resonance than before the second anneal can be observed. This suggests that a higher density of unoccupied states with π character is now present and accessible in the sample. A similar behavior is seen for the σ^* resonance at 291.7 eV as the angle θ is increased towards normal incidence. The transition is in fact more visible than before even at 20°. This suggests that not only the DOS of π states, but also σ states in the sample has increased. Note, however, that the π^* resonance is still the dominating transition, as seen from the beam configuration where $\mathcal{E}_{||}$ aligns with $\hat{\mathbf{n}}$ at grazing incidence. All these three features point to an increase in the number of sp^2 hybridized carbon, in layers parallel to the basal plane of the sample [73].

As for the C $1s$ and Ru $3d$ core levels, Figure 5.8 reveals that all line signals except the S1 component and the one assumed to be sp^2 carbon are collectively attenuated. The former has in fact increased to $\sim 1.4\times$ intensity with the anneal, while the latter has increased to $\sim 4\times$ intensity and shifted by 0.1 eV towards lower binding energy. A similar development of the sp^2 line signal during epitaxial growth of graphene on SiC was reported by Emtsev *et al.* for an increasing number of graphitic monolayers [108]. The relative intensity of the carbonic components S1 and S2 has also changed: S1 is now the dominant phase fo the two. This suggests that parts of the S2 phase have either been buried, lost or transformed into one of the other two phases of carbon. The fact that the intensities of the π^*, σ^* and sp^2 components increase, as opposed to most of the other core level signals in the region, suggests that new layers of graphitic carbon might be forming at the surface of the sample.

The total intensity of the Ru signal has decreased to $\sim 14\%$ after the second anneal. The relative intensities of the metallic Ru to the three silicide phases is also less. This suggests that more of the metal has reacted with Si to form silicides. Note that the relative
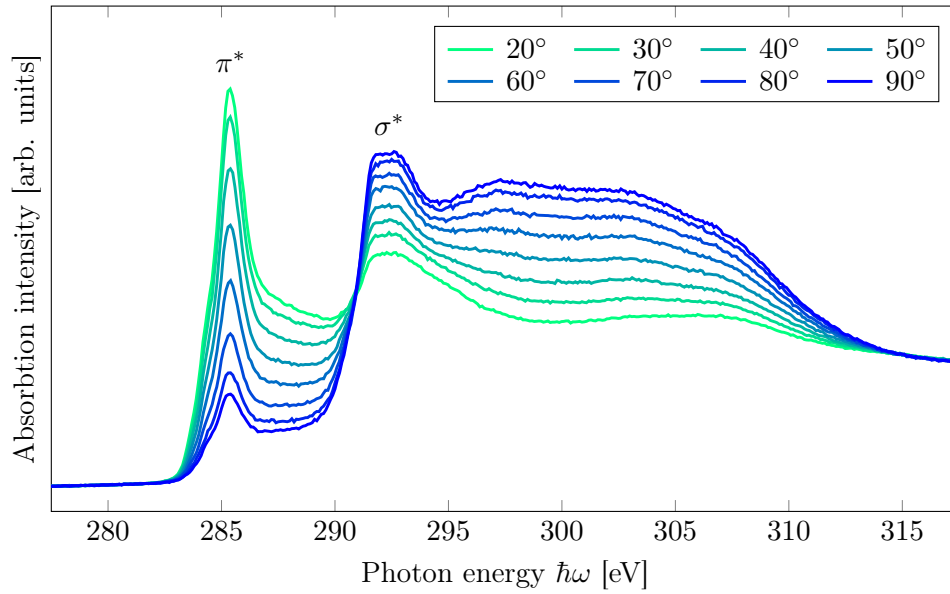
Figure 5.7.: X-ray absorbtion in the viscinity of the carbon K-edge for a 6H-SiC sample, covered in 1.5 nm Ru and annealed to 700 °C, then 800 °C for 1 minute each.
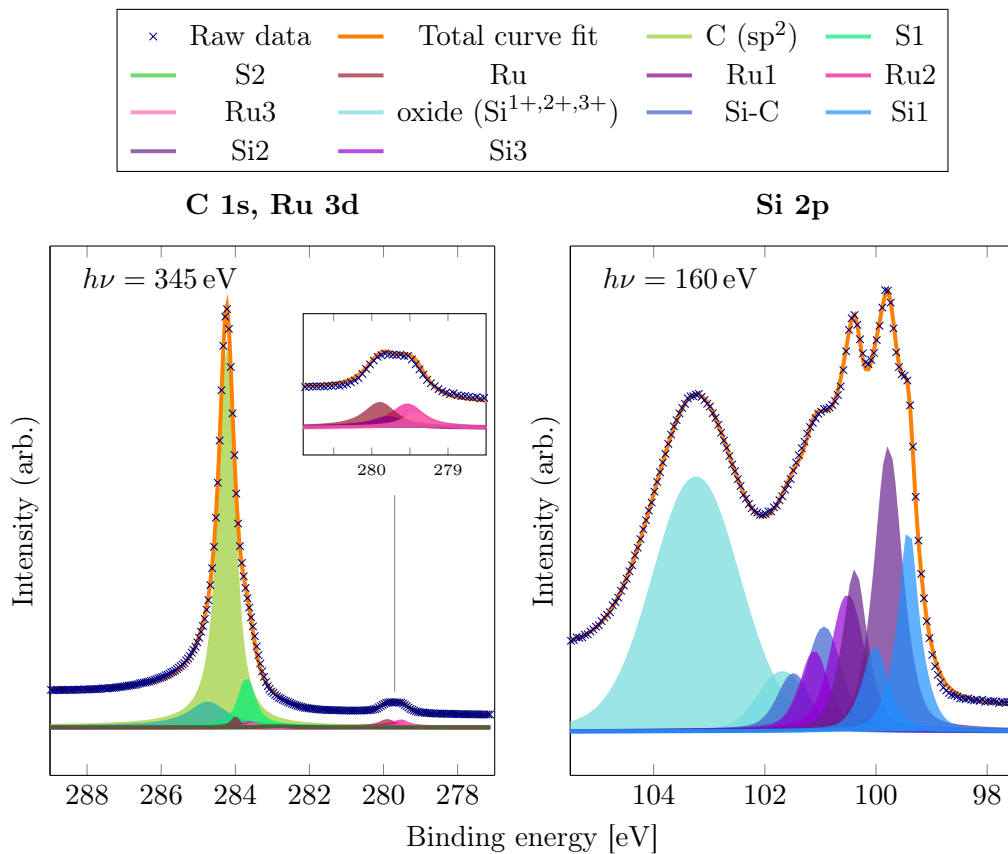

Figure 5.8.: Deconvolved C 1s, Ru 3d and Si 2p signal for the 1.5 nm Ru layer sample, after a second thermal treatment to 800 °C for 1 minute.

intensities of the silicides have also changed, with Ru1 no longer being the dominant phase of the three. The previously observed Ru4 signal assumed to be coming from RuO_2 can no longer be distinguished.

The Si $2p$ region reveals a redistribution of intensity between the previously observed components from Figure 5.6. The Si-C and oxide signals are attenuated by approximately the same amount $(10 - 14\%)$, with their intensity ratio staying roughly the same. This suggests that little or no new silicon oxide has been formed during the anneal. The weight of the oxide signal, however, has shifted towards the higher oxidation states (Si^{2+}, Si^{3+}). A more drastic change is seen in the silicide phases: not only is the lower binding energy component Si1 no longer the dominant phase, but the total intensity of the silicide phases is down to only 36% of their original intensity after the first anneal. The significant loss of silicide intensity compared to the other components in both the Ru $3d$ and Si $2p$ regions suggests that the silicides might be dissolving with subsequent annealing. As $800\,°C$ is well below the evaporation temperature of Ru in the system [126], the metal is assumed to be diffusing *into* the substrate with the second anneal, getting increasingly buried under top layers of stoichiometric SiC.

5.3.3. Depth Analysis of Surface Layers

The observed changes between the NEXAFS spectra in Figures 5.5 and 5.7, as well as between the core levels in Figures 5.6 and 5.8 suggest that layers of graphitic sp^2 carbon form near the surface of the samples when annealed to $700 - 800\,°C$. In order to better understand the composition of chemical species in the topmost layers, the samples initially coated with $0.7\,nm$ and $1.5\,nm$ Ru were probed with varying photon energies $\hbar\omega$ in the range $325 - 1500\,eV$. By eq. 3.5, this corresponds to an inelastic mean-free path in the range $\lambda = 0.43 - 1.88\,nm$, which would give signal from the topmost $5 - 20$ atomic layers[3].

Figure 5.9a shows the deconvolved C $1s$ and Ru $3d$ core levels of the $1.5\,nm$ layer sample, probed with four different photon energies in the specified range. The spectra reveal that the intensity of the sp^2 carbon drops drastically as deeper layers of the sample are getting probed: at $345\,eV$ ($1.4\,nm$ depth), the ratio $I_{sp^2}/I_{\sum Ru} \approx 0.41$, but drops to 0.12 already at $465\,eV$ ($2.2\,nm$ depth)[4]. At higher photon energies the peak is barely distinguishable from the background. In other words, the intensity ratio changes in favor of the ruthenium as the probing depth of the region is increased. This suggests that more layers of ruthenium species are added into the probed volume of the sample, while the level of sp^2 carbon stays relatively constant. That analysis would be consistent with the earlier indications from the NEXAFS and core levels in Figures 5.7 and 5.8 that the graphitic layers are situated near the surface. The S1 and S2 signals experience similar exponential decays for increasing excitation energies. Note that the S1 signal is attenuated twice as strongly as S2 moving to $465\,eV$, suggesting that the S1 peak might be from layers closer to the surface than the S2 peak.

---

[3]Setting the intensity "cut-off" at $1/e^3 \approx 5\%$ as before, and using the mean interlayer spacings of 6H-SiC, Ru(0001) and highly ordered graphite [102, 127, 128].

[4]Note that the flux of the beamline is not uniform in the selected photon energy range, and so comparing the intensities of the same features recorded with different excitation energies is not immediately straightforward. The flux is, however, expected to stay roughly constant within the $\Delta E_B \approx 10\,eV$ window of each scan at a given excitation energy. This allows line signals within the same scan region to be compared. Variations in the relative cross-section of C $1s$ and Ru $3d$ for $\hbar\omega < 500\,eV$ (see Figure 3.3) may, however, overstate the changes between scans using different photoexcitation energies.

(a)

(b)
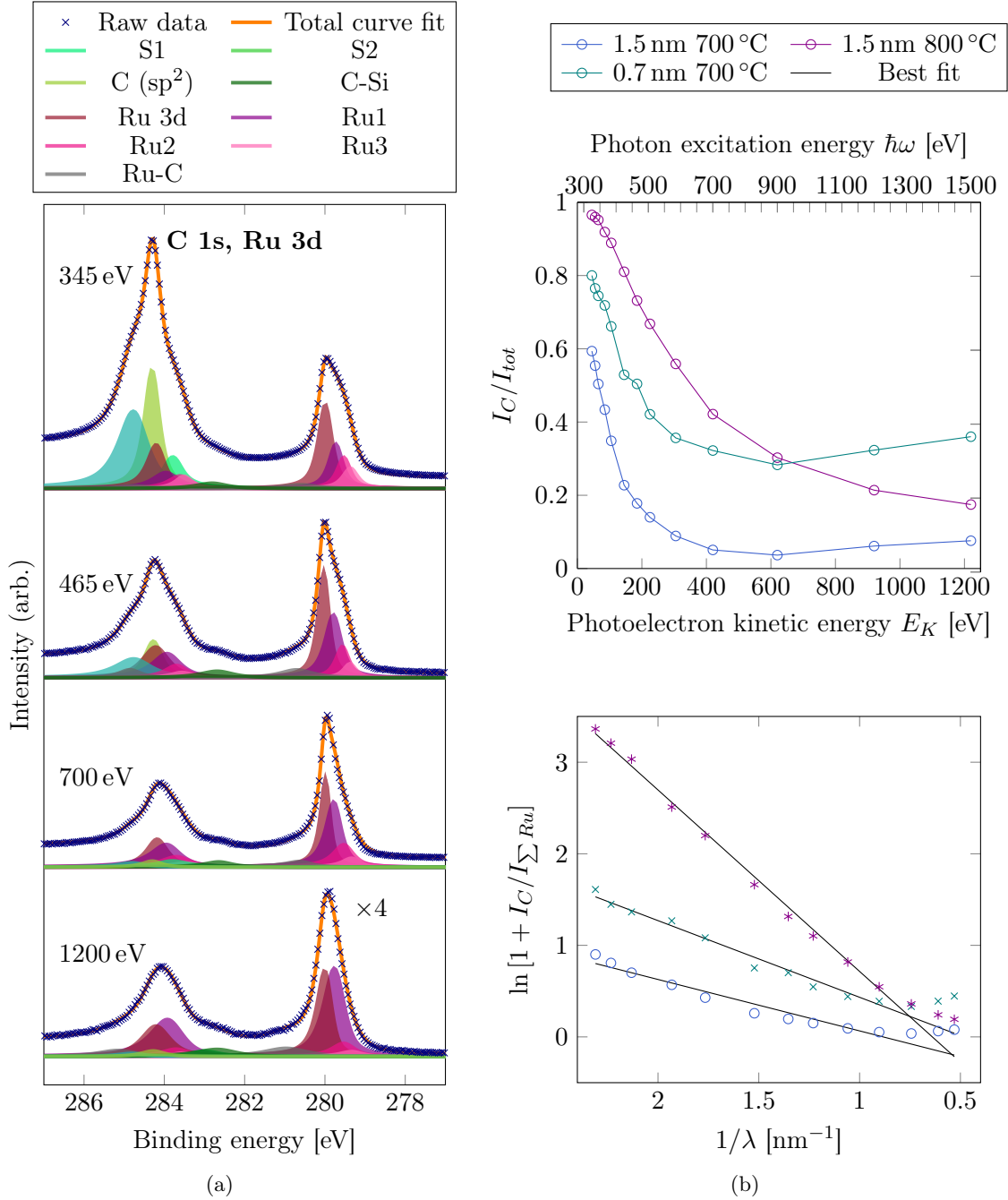
Figure 5.9.: **(a)** Deconvolved spectra for a 1.5 nm layer Ru on 6H-SiC after heating for 1 minute to 700 °C by direct e-beam bombardment to the sample holder. The distribution of core level signals is shown for various excitation energies $\hbar\omega$. **(b)** Intensity of C 1s signal I_C relative to I_{tot} for the C 1s + Ru 3d region vs. photoexcitation energy (top), and the reciprocal IMFP vs. the natural logarithm of $\left[1 + I_C/I_{\sum Ru}\right]$ (bottom), as described in eq. 3.29. The topmost plot also states the kinetic energy of outgoing photoelectrons, referenced to the Ru 3$d_{5/2}$ signal at $E_B = 280.0$ eV.

To better understand the spatial location of different carbon species in the two samples, the collective C $1s$ intensity as a fraction of the background-subtracted total intensity was probed in the overlapping C $1s$ and Ru $3d$ region. The topmost panel in Figure 5.9b shows the fractional intensity of C $1s$ signal as a function of kinetic energy E_K for outgoing photoelectrons, referenced to the binding energy $E_B = 280.0\,\text{eV}$ of metallic Ru $3d_{5/2}$ [95]. The different C $1s$ intensities were determined by estimating and subsequently subtracting all Ru $3d$ doublets form the total intensity recorded in each region (see Chapter 4.4.3).

The intensity plots after 1 minute at $700\,°\text{C}$ immediately reveal very different ratios of carbon to ruthenium in the topmost 5-8 atomic layers ($\hbar\omega = 325\,\text{eV}$) of the two samples. After a subsequent anneal to $800\,°\text{C}$ for 1 minute, the $1.5\,\text{nm}$ layer sample at the same excitation energy gives I_C/I_{tot} close to unity. As seen from Figure 3.3 in Chapter 3.1.1, the photoionization cross-section of Ru $3d$ at $\hbar\omega = 325\,\text{eV}$ is $\sim 3\times$ that of C $1s$. Assuming the photon flux of the beamline is constant over the energy window of core level region, equation 3.19 can be used to find an expression for the fractional density of carbon in the top 5-8 atomic layers:

$$\frac{I_C}{I_{tot}} \approx \frac{n_C}{(n_C + 3n_{Ru})} = \frac{n'_C}{(1 + 2n'_{Ru})}. \tag{5.1}$$

Here, n_C and n_{Ru} are the atomic number densities [nm^{-3}] of carbon and ruthenium, respectively, while n'_C and n'_{Ru} are fractions of the total atomic number density ($n_C + n_{Ru}$) in the layers. Returning to the data, this means that after 1 minute at $700\,°\text{C}$, carbon makes up $> 60\%$ and $> 80\%$ of all atomic species in the $1.5\,\text{nm}$ and $0.7\,\text{nm}$ samples, respectively. With a second flash anneal to $800\,°\text{C}$, close to everything in the topmost layers of the $1.5\,\text{nm}$ sample is carbonic.

The fact that the fractional I_C signal after 1 minute at $700\,°\text{C}$ is higher for the $0.7\,\text{nm}$ sample than the $1.5\,\text{nm}$ sample may at this point seem somewhat counter-intuitive: The formation of graphitic carbon is after all limited by the amount of Ru present in the system (eq. 2.17). However, the analysis presented in Figure 5.9 does not distinguish between sp^2 carbon and carbon in other bonding configurations, like e.g. C-Si from the substrate or components S1 and S2 seen in Figure 5.6. Hence the higher fractional intensity of carbon in the $0.7\,\text{nm}$ sample may well be understood from the fact that fewer atomic layers of Ru will be present after the thinner $0.7\,\text{nm}$ deposition.

All three data sets reveal an exponential decay of the C $1s$ signal for increasing probing depths. This suggests that the Ru $3d$ signal relative to the C $1s$ signal is increasing, as seen for the $1.5\,\text{nm}$ sample in Figure 5.9a. Any signal from preexisting Ru-rich species already in the volume probed by the excitation source are expected to increase exponentially with increasing IMFP λ, according to Beer-Lambert's law (eq. 3.25). Furthermore, additional new layers entering the probing volume as λ increases will of course also contribute to the overall intensity. The decreasing relative intensity of carbon signal for increasing photoexcitation energies up to $\hbar\omega \approx 900\,\text{eV}$ ($E_K \approx 620\,\text{eV}$) therefore suggests that a finite amount of carbon is present in the topmost 15 layers of the sample[5]. A similar behavior is seen for the thinner $0.7\,\text{nm}$ layer sample, although the trend is not equally strong. Note that the rate of decay is somewhat overstated for the first couple of data points in each graph, as the relative cross-section of Ru $3d$ to that of C $1s$ is increasing up to $\hbar\omega \approx 500\,\text{eV}$.

---

[5]$\lambda \approx 1.34\,\text{nm}$, corresponding to signal coming from up to $\sim 4\,\text{nm}$ below the surface.

Table 5.2.: Experimental thicknesses [nm] for the C 1*s* overlayers, estimated from the gradient of the best-fit lines described by eq. 3.29 over the IMFP range assumed to be representing a simple two-layer system. The equivalent number of monolayers (MLs) for Van der Waals bonded graphite and covalently bonded graphene layers in AA stacking has also been included, based on their literature values.

Data set	C 1*s* Thickness [nm]	MLs (VdW / AA)
0.7 nm 700 °C	0.84 nm	2.5 / 5.4
1.5 nm 700 °C	0.56 nm	1.7 / 3.6
1.5 nm 800 °C	1.98 nm	5.9 / 12.7

At photoexcitation energies beyond 900 eV, the data sets for both samples treated at 700 °C for 1 minute change trend: both show a faint linear increase with increasing $\hbar\omega$[6]. This could be an indication that atomic layers below the transition metal silicides are now being probed, i.e. that photoelectrons are being excited from unreacted layers of the SiC substrate. This would explain the increasing ratio of I_C to I_{tot}: there would be a finite amount of Ru in the excited volume, while more C 1*s* signal would be added in with increasing λ. In comparison, the fractional I_C signal from the sample undergone *two* heat treatments decays over the entire photoexcitation range. This behavior is consistent with the indications from Chapter 5.3.2 that the silicides might be dissolving with subsequent heating, and that Ru atoms are diffusing further into the substrate.

The bottom panel of Figure 5.9 shows the natural logarithm of I_{tot} in each scan region divided by the intensity sum $I_{\sum Ru}$ of the Ru species present[7], as a function of reciprocal inelastic mean-free path $1/\lambda$. Based on the hypothesis of having graphitic carbon layers situated on top of silicides, the plots were generated to investigate the linear relationship expressed by equation 3.29 in the simple two layer system approximation. The last two data points beyond $1/\lambda \approx 0.744$ were omitted from the regression, based on the preceding analysis suggesting that in this energy range, the system could no longer be described by two layers only.

Up to $1/\lambda \approx 0.744$ ($E_K \approx 620$ eV), all three data sets show the expected linearity with $1/\lambda$. Notice the different gradients of the best-fit lines for the 1.5 nm Ru layer sample before and after the second 1 min anneal to 800 °C. According to equation 3.29 this gradient should equal the thickness d of the overlayer. The higher gradient therefore suggests that more carbon has been formed near the surface with the second anneal. Similarly, the gradient for the thinner 0.7 nm Ru layer sample after 1 minute at 700 °C suggests a thicker overlayer than for the one coated with 1.5 nm Ru. This behavior has already been discussed from the different I_C/I_{tot} ratios seen in the top panel of Figure 5.9, and explained by the inability to distinguish surface carbon from e.g. C-Si bonds in the substrate.

Table 5.2 summarizes the thicknesses d estimated from the different gradients in nanometers, and in monolayers bonded by Van der Waals forces versus the more closely spaced AA stacking configuration [129]. Note again that these estimates tend to overstate the

---

[6]Note, however, that more data points in this energy region would be needed to properly verify the trend.

[7]$I_{\sum Ru}$ is assumed to equal $I_{tot} - I_C$ in the approximation.

thickness of any carbonic surface species, as all C $1s$ signal is simply assumed to come from the surface. The trends presented in Figure 5.9 and Table 5.2 therefore only provide a crude estimate of the overlayer thicknesses. A more sophisticated model is needed to properly verify which sample has produced the most graphitic carbon at what stage in the anneal process. Nonetheless, the analysis is still very instructive: it verifies that the majority of carbon signal in the samples after annealing is coming from layers near the surface.

Returning to Figure 5.9a, the energy series for the Ru $3d_{5/2}$ peak of the 1.5 nm sample shows a redistribution of intensity between the three phases of silicide with increasing IMFP λ. Notably, the Ru2 and Ru3 signals get strongly attenuated at higher photon energies. This suggests that a finite amount of these phases are found in layers near the surface of the sample. The Ru1 phase, however, seems to extend throughout the probed volume, increasing steadily in intensity relative to both Ru2, Ru3, and the metallic Ru signal. Minuscule amounts of Ru4 (RuO_2) can also be distinguished, but the location of the phase in the sample is not easily determined for signals with this intensity.

5.4. Deposition of Silicon

The results and discussion in Sections 5.3.1−5.3.3 indicate that graphitic carbon layers form at the surface of Ru covered 6H-SiC samples with short heat treatments to 700 and 800 °C. In the next experimental step, graphitized samples were exposed to gaseous silicon while being held at ~ 450 °C, with the intention of intercalating the silicon below the carbon surface layers.

Figure 5.10a shows the NEXAFS from two samples at grazing incidence, before and after depositing approximately 0.6 nm of silicon on each. If the deposition had chemically altered the graphitic carbon layers somehow, the NEXAFS would be expected to show some loss of intensity or definition for the characteristic π^* and σ^* resonances. Quite the contrary: the resonance features in the absorption spectrum of the 1.5 nm Ru layer sample appear to be equally strong after Si deposition, and stronger for the 0.7 nm sample. This confirms that the sp^2 carbon layers have not been damaged during deposition.

Figure 5.10b shows the LEED pattern of a sample from SXR after depositing 0.7 nm Ru, annealing to 700 °C for 1 minute and subsequently adding 0.6 nm Si. The pattern was recorded with incident electron energy 160 eV, and reveals a hexagonal reciprocal lattice structure with bright and defined diffraction spots. This confirms that the surface layers exhibit a highly ordered, crystalline honeycomb structure as commonly seen for 6H-SiC and highly ordered graphene or graphite [104, 130]. Using equation 3.41 from chapter 3.1.3, the lattice parameter a of the hexagonal pattern was estimated to (2.8 ± 0.1) Å. This is roughly 14% higher than what is expected for graphene [131], and 10% lower than the lattice parameter of 6H-SiC [132]. Note, however, that the intrinsic surface sensitivity of LEED measurements rule out the possibility of seeing SiC at the surface when 1.3 nm of different material has been deposited on top. There is also some uncertainty in the actual working distance to the LEED screen. For the calculations, this was simply assumed to match the one stated in the manual of the LEED system. However, a misalignment of a few millimeters is enough to cause the +0.4 Å offset from the graphene lattice parameter. The chemical specie at the surface can therefore not be determined from the diffraction pattern alone. But based on the previous observations from the C $1s$ core level and the
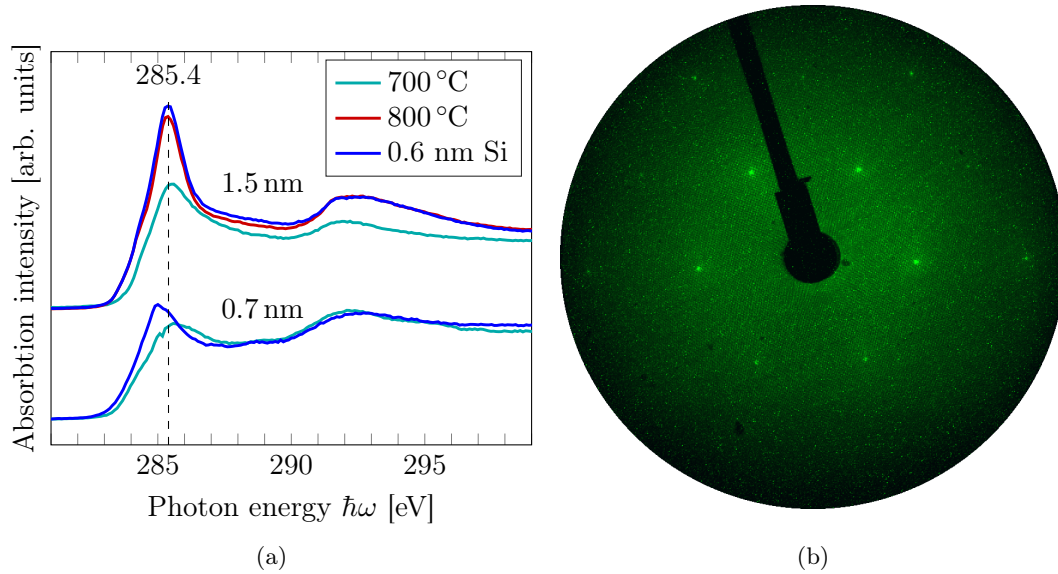
Figure 5.10.: **(a)** The NEXAFS spectra for the samples initially coated with 1.5 nm and 0.7 nm Ru in the vicinity of the carbon K-edge, prior to and after Si deposition **(b)** LEED spectra for the 0.7 nm sample, recorded with incoming electron energy 160 eV.

carbon K-edge NEXAFS, it is likely to be one form of graphitic carbon.

Figure 5.11 shows the deconvolved Si $2p$ core levels from the sample with the 1.5 nm Ru layer, and the C $1s$ and Ru $3d$ core levels from the 0.7 nm Ru layer sample. Similar results with only minor variations in the preexisting features were seen for the Si $2p$ spectrum of both samples. The differences between the two samples in the C $1s$ and Ru $3d$ region are discussed below.

In the C $1s$ and Ru $3d$ region, the deposition seems to bury several of the preexisting features: both the ruthenium, the silicides and the substrate are attenuated by $\sim 50\%$. The intensity of the sp^2 carbon, on the other hand, has increased by 2.5×, and the S2 component can no longer be distinguished. Notably, the added intensity of S1, S2 and C sp^2 before and after deposition stays roughly the same: only 4% is lost in the process. This offset may easily be accounted for by random errors in the experiment caused by e.g bad alignment of the sample holder as it was transferred in an out of the analysis chamber. Overall, the strong preservation of carbon signal intensity suggests that the Si atoms are intercalated below any graphitic surface layers, forming little or no clusters on top of it. Examining the redistribution of intensity between these three carbon components gives further insight into the chemistry the system. First, the magnitude of the added intensity to the carbon sp^2 after Si deposition is $\sim 0.9\times$ the lost intensity from the S2 component. The intensity of the S1 component, on the other hand, stays roughly the same. This suggests that most of the S2 component might have been converted into graphitic carbon during the 40 minutes the sample was kept elevated at $\sim 450\,°C$. A 0.1 eV shift of the C sp^2 signal to lower binding energy, similar to what was seen for the 1.5 nm Ru layer sample
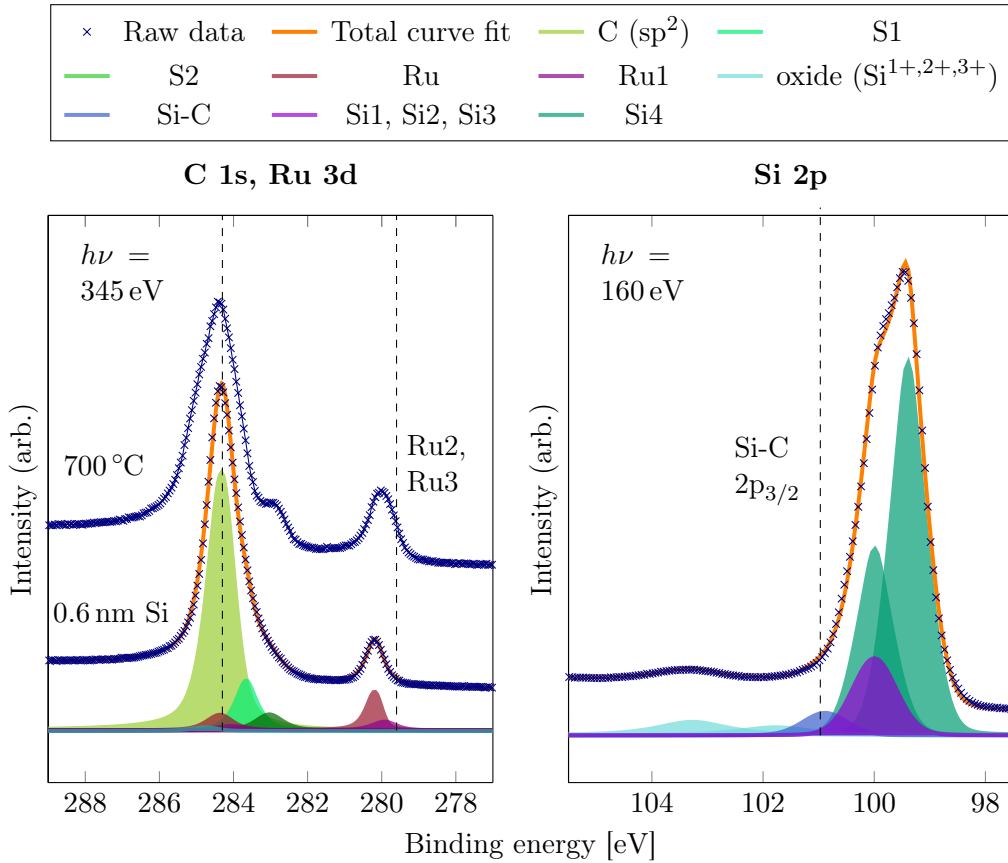
Figure 5.11.: Deconvolved C $1s$, Ru $3d$ and Si $2p$ spectra after deposition of 0.6 nm Si. The ruthenium, silicide and substrate components have been buried under new layers of Si. The S2 signal has disappeared, but the remaining surface carbon signals are unaffected by the deposition.

with subsequent annealing[8], can also be observed. The intensity of the S1 component is unchanged with the deposition, and therefore it is assumed to be situated in the topmost layers of the sample.

The C $1s$ and Ru $3d$ core levels after Si deposition for the sample that was initially covered with 1.5 nm Ru showed several similarities to what is seen in Figure 5.11. All ruthenium components were attenuated, and the S2 component could no longer be distinguished. On the other hand, the intensity of the S1 component was reduced by $\sim 40\%$, and the C sp^2 by $\sim 8\%$. This indicates that the sample's S1 component might be dissolving or getting buried by the new material, while the graphitic carbon may be getting small clusters of Si forming on top of it. The reason behind the different behavior of the two samples is not clearly understood, as both Si depositions were performed for similar durations with similar fluxes from the same target. Note, however, that the different thermal treatments of the samples beforehand is assumed to have resulted in different thicknesses of graphitic carbon near the surface (see discussion in Section 5.3.3). This would mean that the deposited Si would need to diffuse a further distance to properly intercalate under

---

[8]and hence increasing graphitization, based on the analysis in Section 5.3.2.

the carbon surface layers of the 1.5 nm sample than for the 0.7 nm sample. This may well have resulted in some different rates and levels of intercalation between the two samples.

Turning the attention to the Si $2p$ region, a new prominent feature assumed to be coming from the deposited silicon is observed at binding energy 99.4 eV[9]. The signal has been fitted with a symmetric pseudo-Voigt, having peak separation 0.6 eV like all other Si $2p$ signals in previous spectra. Note how the new feature overlaps with the region where the three silicide phases Si1, Si2 and Si3 were previously observed (see Figure 5.8). It is therefore not obvious whether this feature is pure Si or yet a new phase of silicide, judging by its binding energy alone [113]. Based on the observed attenuation of the silicides in the C $1s$ and Ru $3d$ region of both samples[10], however, the signal is be assumed to be from more or less pure Si.

Similar to what was seen for the C-Si and ruthenium signals, the preexisting features in the Si $2p$ region also get attenuated by the deposition. Note, however, that the substrate, oxides and silicides experience different degrees of attenuation: the Si-C signal is attenuated less than the others. Assuming that the oxide and silicide layers were situated on top of the pristine substrate before the deposition, this behavior is unexpected. A possible explanation could be that the prolonged annealing at $\sim 450\,°C$ has caused some of the newly added silicon to bond with carbon near the surface. This would then result in a line signal (and thus added intensity) at similar binding energy to the crystalline SiC in both core level regions that cannot easily be distinguished.

5.5. Oxidation of Silicon-Rich Layers

In the final experimental step, all samples were exposed to molecular oxygen while heated in an attempt to oxidize the silicon deposited in the previous step. Figure 5.12 shows the C $1s$ NEXAFS for the sample initially coated with 1.5 nm ruthenium and then 0.6 nm silicon, after being exposed to oxygen at atmospheric pressure and left to cool down under ambient conditions for about 30 minutes. The absorption intensities of the π^* and σ^* resonances are almost unchanged, and the same angular dependence that were observed after both preceding experimental steps is still visible. At grazing incidence ($\theta = 20°$), a new feature can be observed at about 288 eV, between the absorption intensities of the π^* and σ^* resonances. From the expected inertness of graphitic carbon in few-layer configurations[11], the feature is likely to come from some sort of carbonic contamination, possibly left on the surface of the sample after its prolonged exposure to ambient conditions. A similar feature has been reported previously to be coming from a σ^* transition in residues of organic species rich with C-H bonds [73, 134].

NEXAFS spectra were also recorded in the regions that had been intentionally shadowed by Ta foil throughout the experiment. This was done in order to determine whether graphitic formation had occurred only in the regions that had been directly exposed to Ru prior to the heat treatments. Figure 5.13 shows the carbon K-edge NEXAFS recorded at grazing incidence in both the shadowed and unshadowed regions over the same photon energy range. A snapshot of the sample showing the spatial location of the beam spot

---

[9]As referenced to the $2p_{3/2}$ component of the doublet.

[10]Comparing Figure 5.6 with the spectra in Figures 5.8 and 5.11.

[11]e.g. graphene, which has proven to be chemically inert at high temperatures ($> 1500\,°C$) where other forms of carbon would readily react chemically with surrounding species [133].
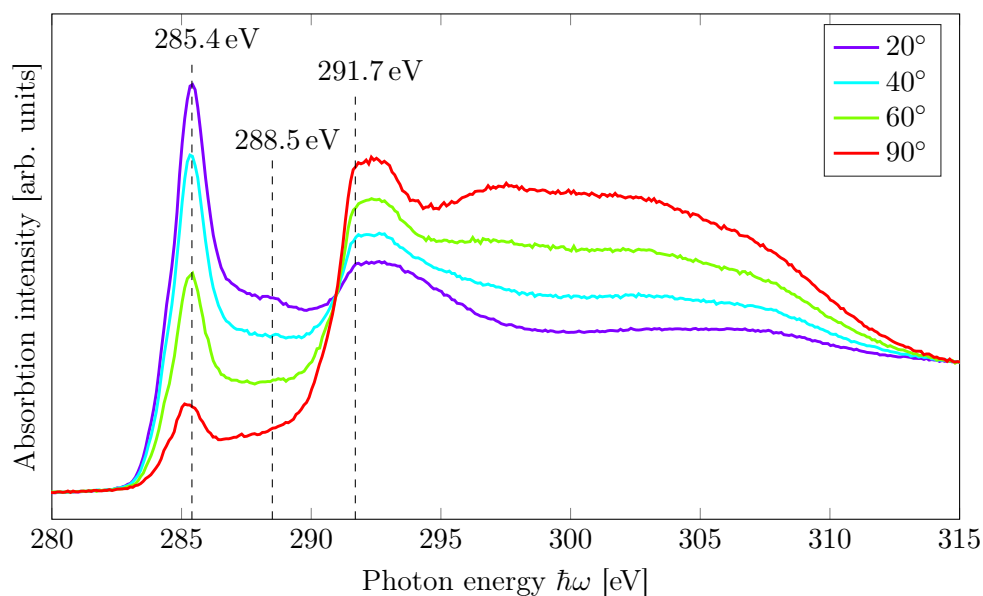
Figure 5.12.: X-ray absorbtion in the viscinity of the carbon K-edge, after final oxida-
tion for a sample initially coated with 1.5 nm Ru. The strong π^* and σ^*
resonances are almost unchanged with the formation of silicon oxide layers
underneath. A new faint resoance feature can be observed at 288.5 eV.
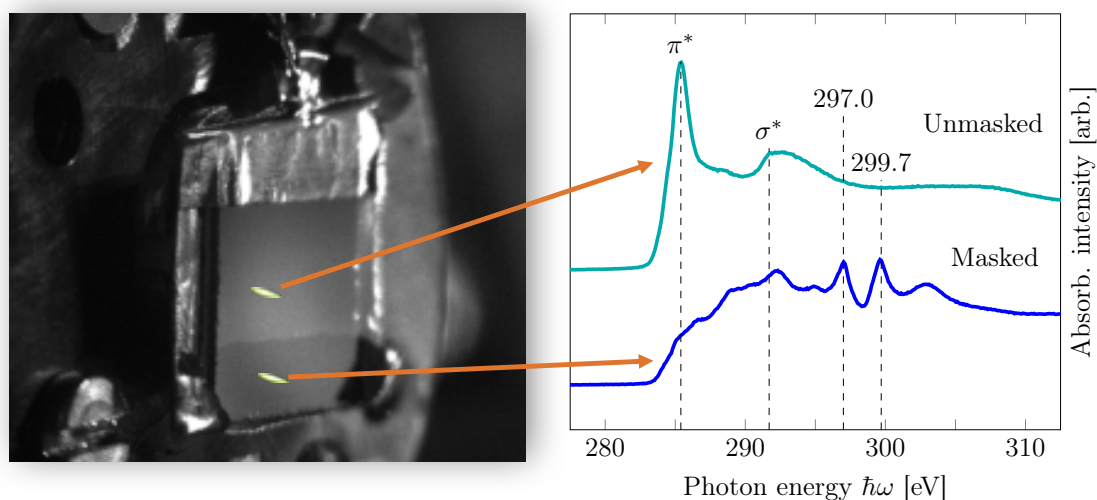
Figure 5.13.: (**Left**) A spapshot of the 1.5 nm sample in its scan position , after peeling
back the lower strip of Ta foil and reloading it into vacuum. A photo of the
beam spot on an yttrium aliminium garnet (YAG) crystal has been overlaid
with the sample picture in the two scan locations used. Notice the distinct
shadowing effect on the lower half of the sample visible from the earlier
ruthenium deposition. (**Right**) The recorded NEXAFS spectra from the
two regions marked on the sample image. No strong π^* resonance is visible
in the spectra recorded from the previously shadow masked region. Two new
and distinct features are, however, visible at 297.0 eV and 299.7 eV.
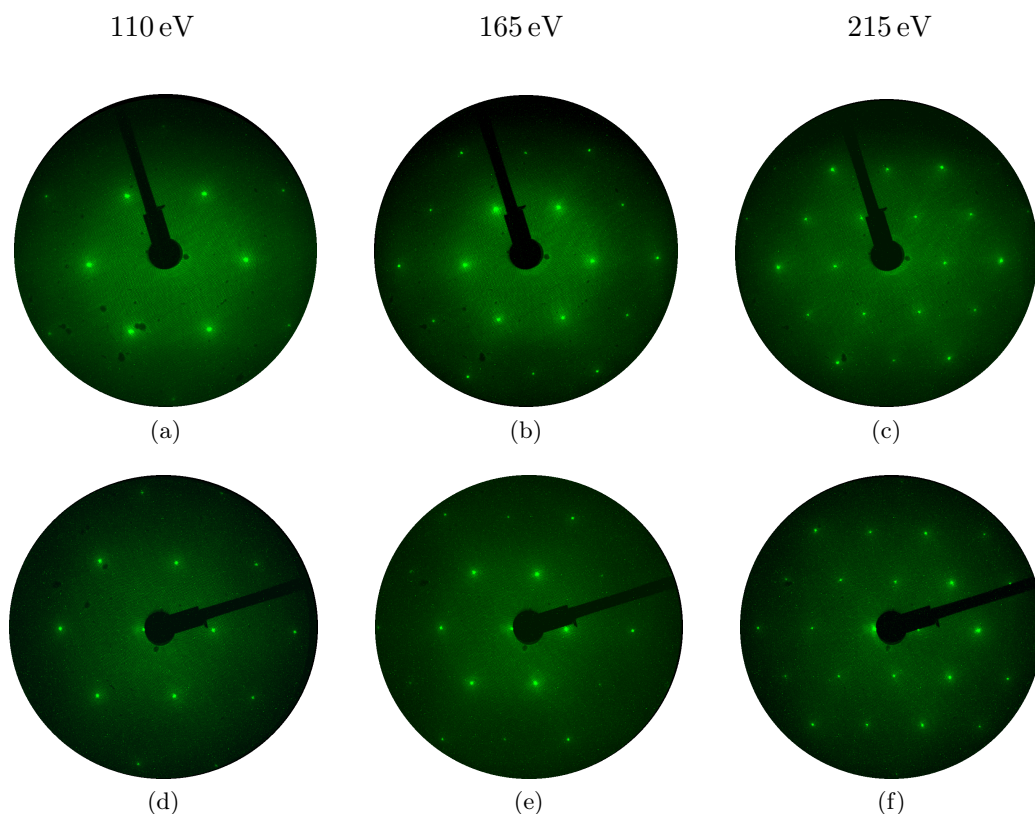
Figure 5.14.: LEED patters for the 0.7 nm sample (**a-c**) and the 1.5 nm sample (**d-f**), taken with incoming electron energies 110 eV, 165 eV and 215 eV. Similar LEED patters can be observed for both samples, with a lattice parameter $a \approx 2.4\,\text{Å}$ close to what is expected for graphene. Note that the samples appear to have been mounted with a 90° rotation relative to one another.

during the recording of either spectra has also been included. The spectrum from the unshadowed region was already shown in Figure 5.12, exhibiting strong resonances for the $1s \to \pi^*$ and $1s \to \sigma^*$ transitions that are characteristic for graphitic sp^2 carbon. The absorption spectrum from the shadowed region is remarkably different. First of all, no π^* resonance can be observed whatsoever near the carbon K-edge. A feature that is somewhat similar to a σ^* resonance can be observed at 292.2 eV, but the missing π^* means this one is not coming from sp^2 carbon in layers parallel to the surface. Comparing the spectrum to the one expected for 6H-SiC(0001) at grazing incidence ($\theta = 20°$) reveals that most of its resonance features are coming from carbon layers in the substrate [122]. However, two prominent features found at 297.0 eV and 299.7 eV were previously not observed in the NEXAFS for clean SiC. The resonances must therefore be coming from some carbon-containing specie near the surface. These are not known resonances for sp^2 carbon, and therefore assumed to be coming from contaminating residues left on the Ta foil before it was overlaid with the sample to form the shadow mask [135].

Figure 5.14 shows LEED patterns from two samples, obtained in the unshadowed regions that were directly exposed to silicon and oxygen after the formation of sp^2 carbon. One sample was initially coated with 0.7 nm ruthenium and the other with 1.5 nm ruthenium.
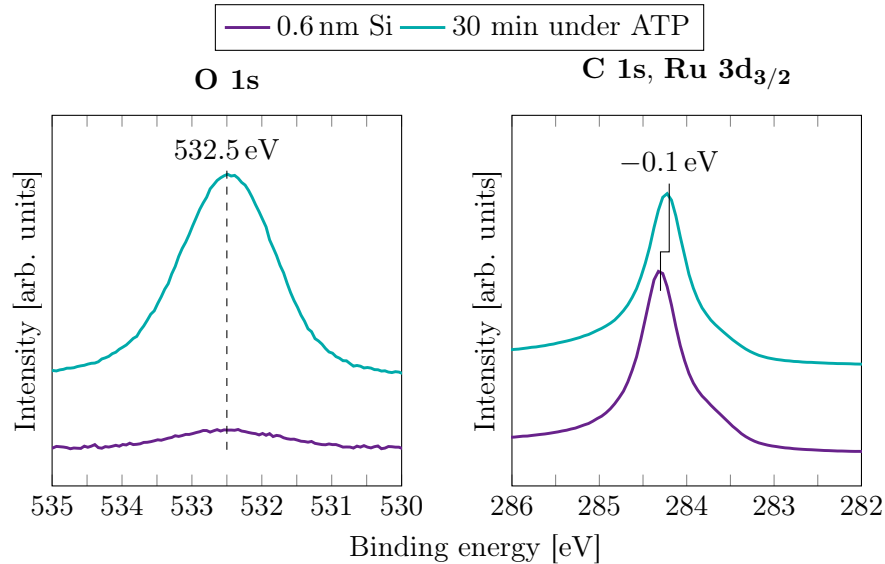
Figure 5.15.: The O 1s and C 1s core levels of an SiC sample after exposure to oxygen at atmospheric temperature and pressure (ATP) for 30 minutes. The sample was initially coated with 1.5 nm Ru, thermally treated to trigger graphene growth, and had 0.6 nm Si intercalated under the graphene layers before oxidation. The increase in O 1s signal intensity verifies the presence of oxygen in the surface layers. The intensity of the C 1s level is roughly unchanged, but shifted by 0.1 eV towards lower binding energy.

The patterns were recorded with incoming electron energies 110 eV, 165 eV and 215 eV. All six diffraction patterns reveal a hexagonal reciprocal lattice structure, reminiscent of the honeycomb structure that is expected for graphene and highly ordered pyrolytic graphite (HOPG)[12]. Similar dot spacings can be observed for patters recorded with the same energies on either sample. Furthermore, the real space lattice parameter a of both samples match roughly with the one estimated from the pattern in Figure 5.10b. This indicates that the same material is still present at the surface after oxidation. Based on the threefold symmetry of hexagonal patterns, the quadratic SiC samples are revealed to have been mounted with a 90° rotation relative to one another at the beginning of the experiment.

Figure 5.15 shows the change in the line signals of the O 1s and combined C 1s and Ru $3d_{3/2}$ regions with the exposure to atmospheric oxygen. The spectra have been taken from the sample initially coated with 1.5 nm Ru, but similar results were seen for both of the samples prepared at the SXR[13]. The O 1s region reveals an apparent increase in the level of oxygen present on the sample after exposure. A seemingly symmetric feature is now visible with binding energy about 532.5 eV, roughly +0.6 eV higher than the dominant feature observed for the clean sample in Figure 5.2. The signal intensity in the C 1s and Ru $3d_{3/2}$ region appear to be roughly unchanged with the oxidation, except for a slight

---

[12]See Figure 2.1a in Chapter 2.

[13]Both samples were heated to ~ 400 °C prior to the exposure, but the heating was turned off as the loadlock was vented. Judging by the thermostat, the temperature of the samples had sunk to ~ 350 °C by the time the loadlock reached atmospheric pressure.
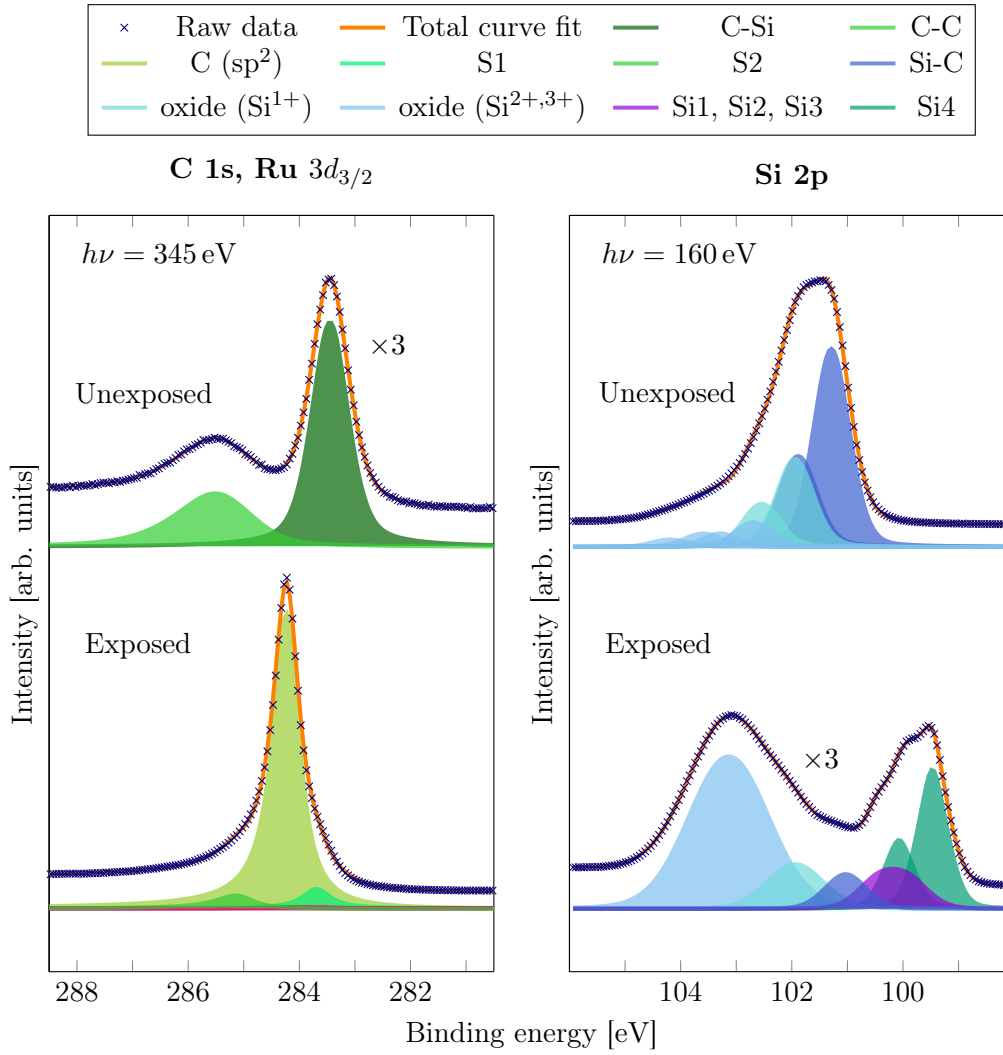
Figure 5.16.: Deconvolved C 1s, Ru 3d and Si 2p core levels after exposing the 1.5 nm Ru layer sample to oxygen at atmospheric pressure for about 30 minutes. The spectra for both the regions covered and uncovered by the Ta foil throughout the experiment has been recorded.

0.1 eV down shift in binding energy of the peak maximum. Similar shifts were reported by Larciprete *et al.* for intercalation of O$_2$ under epitaxial graphene on Ir(111), and was attributed to charge transfer from the graphene to the electronegative oxygen, leading to hole-doped graphene [136].

Figure 5.16 shows the deconvolved C 1s, Ru 3$d_{3/2}$ and Si 2p core levels in the same region of the sample as the oxidized spectra shown Figure 5.15. For comparison, the same core levels but from the region previously shadowed by Ta foil have also been included. The Si 2p spectrum from the exposed region show a strong attenuation of the intercalated Si relative to the substrate and silicide peaks. The opposite is seen for the relative intensity of the sub-oxides, having increased significantly. The intensity of the added sub-oxide signal relative to the Si4 signal has also changed from $\sim 0.1 \times I_{Si4}$ to $\sim 2.3 \times I_{Si4}$ with

the oxidation. This suggests that a large portion of the intercalated Si has oxidized while being exposed to atmosphere. This matches with the increased presence of oxygen seen from Figure 5.15. The relative intensity ratio of the two oxide peaks Si^{1+} and $Si^{2+,3+}$ before and after exposure indicates that mostly higher oxidation states have been favored in the reaction.

The C 1s spectrum shows that the intensity of the carbon sp^2 signal is reduced by only 4% during oxygen intercalation. This suggests that the chemical nature of the graphitic carbon at the surface is more or less unaffected by the exposure to atmosphere, as already indicated from the NEXAFS and expected for inert graphene layers [133]. The Ru signals can no longer be distinguished under the overlying layers of graphitic carbon and silicon oxide[14]. A new feature is however observed at binding energy 285.2 eV, +0.4 eV from where S2 was seen previously. This somewhat resembles the observed line signal at 285.5 eV in the unexposed region. The binding energies of the two signals match roughly with the expected binding energy for sp^3 hybridized carbon bonding to carbon in organic residues [137, 138]. The presence of hydrocarbons was also previously indicated by the resonance feature at 288.5 eV in the NEXAFS spectra of Figure 5.12.

C 1s and Si 2p recorded in the previously shadowed region of the sample bear a striking resemblance to the ones from the clean substrate seen in Figure 5.2. Notably, neither show any indications of graphitic carbon, ruthenium nor silicides being present. This suggests that no graphitic surface layers were formed in the regions that were unexposed to the depositions of Ru and Si.

---

[14]Like in all earlier fits, the amount of Ru $3d_{3/2}$ in the region was determined by first fitting the Ru $3d_{5/2}$ region. Subsequently, features with the appropriate intensity $(2/3) \times I_{Ru_{5/2}}$ were added to the Ru $3d_{3/2}$ region with position fixed by the spin-orbit splitting of Ru [95, 114].

6. Conclusions

This final chapter summarizes the experimental outcomes presented in the previous chapter, and evaluates them against the two main aims of the project:

1. To selectively grow high-quality, epitaxial few-layer graphene, mediated from bulk SiC at lower process temperatures using a transition metal,

2. To effectively decouple the grown carbon layers from the underlying substrate, so that they can behave as freestanding graphene.

The Chapter is ended with some concluding remarks on the overall success of the project, with a few pointers to what further work may improve, complement or enrich the results.

6.1. Graphene Growth

As discussed in Chapters 5.3.1-5.3.3, all samples processed during both the beam times indicate the formation of graphite or graphene from thermally treating Ru on 6H-SiC. The core level analysis reveals signs of C sp^2 that grows readily with subsequent heat treatments: both with equal duration at higher temperatures, and also for longer durations at lower temperatures[1]. Samples prepared at the SXR with different initial thicknesses of Ru also showed prominent and similar angle dependencies in their carbon $1s$ absorption spectra. From the absorption recorded at grazing incidence ($\theta = 20°$), all seem to indicate the formation of sp^2 hybridized carbon in atomic layers that are parallel to the basal plane of their underlying substrates. Stronger resonances, particularly for the $1s \rightarrow \pi^*$ transition, were seen from the samples coated with the thickest layers of Ru. LEED patterns revealing a highly ordered, hexagonal crystal phase at the surface of the sample, reminiscent of what would be expected from graphene, was also observed in the final stages of the SXR experiments.

6.1.1. Formation of Uniform Graphitic Layers

The results from Chapters 5.3.1 and 5.3.2 showed that different amounts of graphitic carbon was observed for different samples at the two beam times. Notably, less graphitic carbon seems to have been produced for the samples that were covered with relatively thin layers of Ru, as compared to the ones with thicker layers under the same processing conditions (see for instance the C sp^2 signals in Figure 5.6). By re-examining the expected reaction mechanism from Chapter 2 (eq. 2.17), the amount of ruthenium present in the system appear to be limiting the amount of graphene that can be produced. One C atom is liberated per Si atom that reacts with an Ru atom, and there will be an apparent surplus of SiC to Ru in the material system. This makes the thickness of the deposited

---

[1]The former was seen from the sample treated at 700 °C, then 800 °C for 1 minute each. The latter was seen from the 0.7 nm Ru layer sample after 40 minutes at ∼ 450 °C during Si deposition.

metal film the obvious limiting factor, if all other process parameters are assumed equal. If the amount of ruthenium is then insufficient to form uniform layers across the sample surface, this could lead to poor wetting of the surface that would result in clustered metal features, and thus mediation of carbon only in selected areas. Possible indications of this were seen for samples coated with 0.7 nm and 0.9 nm Ru prepared at SXR and MATline, respectively: distinct LEED patters reminiscent of that of graphene were visible only in certain regions. On the contrary, samples coated with 1.5 nm Ru showed LEED patterns with similar orientation, intensity and sharpness throughout the region unshadowed to incoming Ru during the metalization step.

The apparent dependence on Ru thickness may in some cases be regarded as an obvious caveat to the growth procedure. For instance, its usefulness may be limited for applications where uniform layers of graphene are needed, like in e.g. wafer-scale production of electronic devices requiring photolithographic post-processing. On the other hand, if the thickness of Ru needed to produce a finite amount of graphitic carbon is well understood, the behavior can potentially be exploited to create tunable thicknesses of graphene down to a number of desired monolayers (MLs). This would, however, require a thorough understanding of the different stochiometries of ruthenium silicides being formed during annealing, and how they vary with process parameters like e.g. temperature and time[2].

For the results presented in this project, longer anneal times at the same specified temperature were required to produce visible graphene signals in the XPS at MATline than at SXR. This is assumed to be an indication of variability in the realized growth conditions between the two experiments. Most likely, it is a product of the different anneal setups used at the different endstations. Where the samples prepared at SXR were heated by *direct* and highly intense electron beam bombardment to the sample holders with almost instantaneous heat transfer, the samples at MATline were all heated *indirectly* by means of a hot filament in the proximity of the sample(s). In hindsight, the ones prepared at MATline are assumed to have experienced a weaker heat gradient and hence a slower rise in temperature than what was achieved at the SXR. For similar durations of annealing, this would lead to less time spent while elevated to, or beyond the *critical temperature* to initiate and drive the growth procedure. Note that this temperature has not yet been determined exactly, but is expected to be observed $> 600\,°C$ based on the results in Chapter 5.

6.1.2. Location and Thickness of Graphene Growth

The depth analysis in Chpt. 5.3.3 indicates that the layers of sp^2 carbon formed from the reaction of ruthenium with the SiC substrate are situated at the surface of the sample. This was seen from both the manually deconvolved spectra and the scripted analysis in Figure 5.9b, as deeper layers of the samples were getting probed. By considering the probing volume of the samples as a simple two-layer system, the thickness of the different graphitic layers were estimated from the gradient of the best-fit lines in Figure 5.9b. These were expected to follow the linearity expressed in equation 3.29. By assuming the surface layers to be weakly bonding, the gradients suggested that 2-6 monolayers layers of sp^2 carbon was formed from the heat treatments.

---

[2]Note again that the ratio of Si to Ru in each configuration one may realise from this growth procedure will liberate a different number of C atoms.

The reader should be aware that the best-fit lines are ideal for estimating these thicknesses, as they will be less prone to random experimental errors than the data points from the individual spectra. Any offsets from the actual thicknesses of the surface layers will be predominantly from *systematic* errors in the simple two-layer model described by eq. 3.29, or in the scripted analysis.

The former of the two will contribute some inaccuracies from the assumptions used to simplify equation 3.28. Namely, these are: the precise ordering of the system in adjacent layers of different species, and the assumption that both have similar cross-sections and atomic number densities. The latter is clearly not true in this case, as Ru has a significantly different density and cross-section in the energy range used than both C and Si [126].

As for any systematic errors in the scripted analysis, a notable example is how the same $8\,\text{eV}$ energy window is considered for all samples over the full range of photoexcitation energies $\hbar\omega$. This was done to be consistently considering the same range of binding energies throughout the analysis. In practice, however, there is an obvious caveat to this: very intense or broad signal features may well have tails reaching outside the data window. This is expected to be most significant for probing depths where the asymmetric Ru $3d$ features are dominating the intensity received, i.e. in the upper half of the photoexcitation energy range (see Figure 5.9b). If the tails of the Ru signals are getting cut off by the $\pm 2\,\text{eV}$ windows centered around each of the two intensity maxima at $\sim 280\,\text{eV}$ and $\sim 284\,\text{eV}$, this would then understate the amount of ruthenium present, which in turn would overstate the fractional intensity of the C $1s$ signal and the thickness of the overlayer given by eq. 3.29.

In order to determine the lateral distribution of the graphitic overlayers, the Ta film was peeled back after oxidation to reveal areas that had be shadowed during Ru deposition. XPS and NEXAFS was then performed both in the shadowed and unshadowed regions. Both techniques show no visible traces of sp^2 carbon nor ruthenium under where the foil was located previously. This not only proves the effectiveness of the Ta foil as a contact shadow mask, but more importantly: it states the ruthenium's vital role in liberating carbon from the SiC bulk for the process temperatures that were used. If the growth of graphitic carbon layers really is restricted to where the ruthenium is located, this opens up the possibility to selectively pattern and grow graphene in desired regions of the substrate surface. Combined with the relatively low processing temperature $< 900\,°\text{C}$, this makes the demonstrated growth process more experimentally viable for integration with existing VLSI processing. Many interesting applications in semiconductor electronics, like the hypothesized graphene-based radiation sensors and transistors that were outlined in Chapter 2, would then be one step closer to large-scale industrial realization.

Note that the precision of the Ru patterning has not yet been properly tested. At the time of writing this is beyond the current scope of the project. The use of Ta strips for shadow masking in this work was only intended to demonstrate that graphene *can* be selectively grown in patterned regions of Ru on SiC in a proof-of-principle fashion. The crude mask design is not at all assumed to be optimized, and may well have allowed Ru to creep some distance under the mask during deposition. Hence the limit to what line widths and feature geometries can be realized from the proposed growth mechanism and shadow masking procedure is yet to be investigated.

6.2. Silicon Deposition and Oxidation

From the strong indications that few-layer sp^2 carbon were formed with the $600 - 800\,°\text{C}$ anneals, attempts were made to decouple the surface carbon from the underlying substrate. This was done by exposing the samples to Si with the intention of intercalating the new material beneath the existing carbon surface layers. Subsequent exposure to atmosphere was expected to oxidize the underlying layers, and hence form transfer-free graphene on insulator in the final stage. This would then leave the surface layers electrically decoupled from the growth substrate and behaving like few-layer graphene in its free-standing form.

The presence of added silicon is easily verified from the Si $2p$ core level after deposition. More importantly though, both the C $1s$ NEXAFS and core levels indicate that the graphene layers are largely unaffected by the addition. NEXAFS from one sample even reveals sharper and stronger resonance features after Si deposition. The intensity of carbon sp^2 from the C $1s$ core level region is at worst reduced by 8%, which is far less than what would be expected from full monolayer Si growth on top[3]. Small errors of $< 10\%$ can easily be disregarded as minor experimental errors in e.g. sample alignment of the focus of the beam. The persistent quality of the graphitic layers with deposition hence suggests that the silicon gets intercalated without making patches on top of it. This is in accordance with what was reported by Lizzit *et al.* [41]. Note, however, that as opposed to the graphene growth, the intercalation of Si was tested for the first time at the SXR beam time. Though seemingly unproblematic, the process has still not been extensively investigated. To minimize the impact of unknown variables, the Si deposition in these experiments were made to replicate that of Lizzit's as closely as possible. There may well be ways to optimize the intercalation process with regard to e.g. Si flux and elevation temperature for the sample during deposition.

Like for the Si intercalation, no significant changes were observed in the carbon K-edge NEXAFS nor C sp^2 core level as the samples were exposed to oxygen at atmospheric pressure. Note that the presence of oxygen in the sample surface layers after exposure is verified by the strongly increased signal intensity of the O $1s$ region. This indicates that the surface carbon is practically inert to the oxygen exposure: a known feature that is characteristic for few-layer graphene [133]. The crystallinity of the surface layers also appear to be unchanged with the oxidation. This can be seen from comparing the LEED patterns before and after the final experimental step.

The deconvolved Si $2p$ core levels reveal that the majority of the previously added Si has turned into fresh layers of silicon oxides. This is verified by the relative intensity increase of the Si$^{2+,3+}$ signal to the signal from the added Si, and to that of the substrate. Note that similar levels of oxidation were seen for samples with different thicknesses of overlayer graphene. This suggests that oxygen diffused equally well through the graphene layers, more or less independent of their thicknesses. Also, it shows that the amount of oxide formed is largely dictated by parameters of the oxidation process that are not related to the overlayer: namely the amount of Si present, the pressure of oxygen and the temperature of the substrate during oxide formation. All of these variables where kept as equal as possible for the different samples at each beam time.

Note that the deconvolved Si $2p$ spectrum shows that there are still unreacted Si present

---

[3]This an be easily seen from the now familiar Beer Lambert's law in equation 3.25, using the relatively short inelastic mean-free paths $\lambda = 4.5 - 5$ Å that were employed in the experiment.

after the 30 minutes the sample was left under atmospheric pressure and temperature. While these layers are expected to stay unreacted when the samples are kept under vacuum, a higher degree of oxidation with time is not at all unlikely if they are instead left outside the vacuum system under standard laboratory conditions of temperature and pressure [98].

6.3. Final Remarks

The experimental results and analysis presented in this project demonstrate that few layers of graphitic carbon, assumed to be graphene, grow epitaxially from 6H-SiC(0001) at temperatures $600 - 800\,°C$, when mediated by thin layers of the transition metal ruthenium. The thicknesses of grown films were in the range $0.6 - 2.0$ nm, and have been shown to vary with the temperature and duration of annealing, and the thickness of transition metal deposited. Compared to epitaxial growth of graphene on clean SiC(0001), the metal-mediated growth holds the advantage of greater control over the thickness of graphene films formed, as the amount of liberated carbon is effectively limited by the total amount of Ru present.

The reaction of Ru with SiC leads to the formation of several different phases of Ru_xSi_y appearing along with the graphene formation. The relative amounts of the different silicide phases also varies with the thickness of the Ru overlayer. The exact chemical nature of these silicides have not yet been determined, as this would require further investigations using e.g. TEM to determine the spatial distribution and inter-planar distance of each phase. Nonetheless, the total amount of graphene formed seems to be ultimately linked to the total amount of Ru, rather than the relative amounts of the different silicides.

Selective growth of graphene layers in the desired regions of the substrate surface has been verified using spatially resolved XPS and NEXAFS. This was done by running comparative scans in regions previously exposed and unexposed to ruthenium through shadow masks. Similar behavior has, to the author's knowledge, not yet been reported in literature. In-situ patterning during growth has the advantage of eliminating subsequent use of photolithography that may easily contaminate or dope the graphene layers when forming electronic devices.

Silicon was demonstrated to effectively penetrate and intercalate under epitaxial graphene layers at $\sim 450\,°C$. This is consistent with what has been reported in literature previously. Oxygen was also shown to diffuse through the graphene and react with the underlying silicon. This led to the formation of insulating silicon oxide that lifted the graphene off of the conducting substrate and silicide layers, leaving it in essentially freestanding form at the surface. This method has the advantage of not needing to transfer the graphene onto a separate insulator, as is widely practiced for other forms of graphene production aimed at industrial applications. Instead, the insulating and supporting matrix is formed directly underneath, eliminating any damage dealt to the graphene from the exfoiliation process. The synthesis route presented here is thus expected to be superior to other methods for producing graphene on insulator on semiconductor. Not just from its straightforward growth process, but also from its relatively low processing temperatures that makes it potentially compatible with existing VLSI process runs in semiconductor device manufacturing.

The reader should note that while the synthesis and decoupling of graphene from 6H-

SiC has now been verified, further investigations are needed to fully determine the quality of the graphene on insulator produced. For instance, Raman spectroscopy can be used to determine both graphene thickness and quality [139, 140]. Initial Raman measurements have been attempted, but the results so far have been inconclusive, due to difficulties in resolving critical resonance features from the spectrum of the underlying SiC substrate. Similar attempts on epitaxial graphene from SiC found in literature clearly state the requirement of significant statistical accuracy, and the subtraction of an equally precise background spectrum to resolve the graphene peaks [141]. Hence Raman is assumed to be obtainable for the samples presented here, although this will require greater precision than what has been obtained at the time of writing.

Furthermore, any interactions of the graphene with the underlying layers have not yet been properly studied. Such interactions, like e.g. charge transfer between the graphene and the underlying layers, or a breaking of its sub-lattice symmetry, are expected to have significant implications on transport properties and its semi-metal performance [142, 143]. The electronic structure of the material could be understood from mapping of the band structure using angle-resolved photoelectron spectroscopy (APRES), or the local density of states around the Fermi level using scanning tunneling spectroscopy (STS).

Finally, the use of four-point probing would help determine the macroscopic transport properties of the graphene layers. Knowledge of these properties will be crucial for any later development and testing of a prototype graphene-based radiation sensor, as the mobility of the channel must be known to accurately interpret conductivity fluctuations from radiation by-products.

A. Appendix

A.1. Orbital Notation

Table A.1.: Electron orbitals for the first three atomic core levels, with their corresponding quantum numbers for orbital angular momentum l, spin s and total angular momentum j. Each orbital spin configuration has also been listed in both spectroscopic and X-ray nomenclature.

Quantum numbers				Spectroscopic notation	X-ray notation
n	l	s	$j = l + s$		
1	0	$\pm 1/2$	1/2	$1s_{1/2}$	K
2	0	$\pm 1/2$	1/2	$2s_{1/2}$	L_1
2	1	$-1/2$	1/2	$2p_{1/2}$	L_2
2	1	$+1/2$	3/2	$2p_{3/2}$	L_3
3	0	$\pm 1/2$	1/2	$3s_{1/2}$	M_1
3	1	$-1/2$	1/2	$3p_{1/2}$	M_2
3	1	$+1/2$	3/2	$3p_{3/2}$	M_3
3	2	$-1/2$	3/2	$3d_{3/2}$	M_4
3	2	$+1/2$	5/2	$3d_{5/2}$	M_5

Table A.2.: Intensity area ratios in an XPS spectrum for core level signals from orbitals s, p, d and f with different spin configurations $\pm 1/2$.

Orbital	l	s	$j = l + s$		Area ratio
s	0	$\pm 1/2$	1/2		N/A
p	1	$\pm 1/2$	1/2	3/2	1:2
d	2	$\pm 1/2$	3/2	5/2	2:3
f	3	$\pm 1/2$	5/2	7/2	3:4

A.2. Selection Rules

For processes involving absorbtion or emission of photons, the allowed transitions between the available quantum mechanical states are determined by so-called *selection rules* of the time-dependent perturbation. These rules can be derived by examining the matrix element, or *dipole element* of specific transitions (the bracket term in eq. 3.9). Using the commutation relations of the angular momentum operators $\hat{L}^2$ and $\hat{L}_z$ with the spatial operators $\hat{x}$, $\hat{y}$ and $\hat{z}$, the following two selection rules for state transitions involving absorbtion or emission of a photon can be derived[1]:

Selection rule #1   No transitions occur unless

$$\Delta l = \pm 1. \tag{A.1}$$

Selection rule #2   No transitions occur unless

$$\Delta m = \pm 1, \text{or } 0. \tag{A.2}$$

Figure A.1 shows the allowed decay scheme between the first four Bohr levels in a hydrogen-like atom.

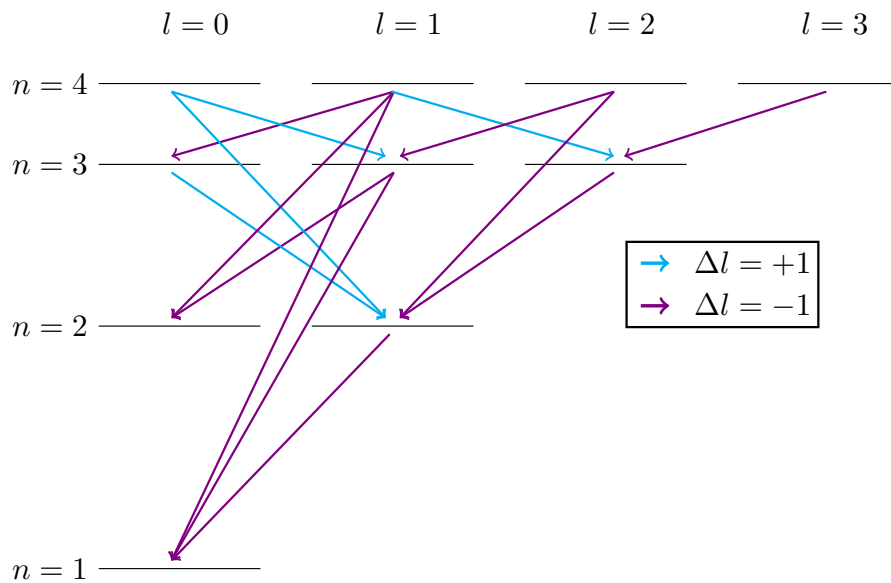Figure A.1.: Schematic of the allowed decays between the different orbitals of the first four Bohr levels in a hydrogen-like atom. Note that the direction of the arrows can easily be reversed to describe the allowed excitation between core levels upon absorbtion instead of emission of a photon with spin 1.

---

[1]A step-by-step derivation can by found in the introductory text by D. J. Griffiths [15].

A.3. Ruthenium Deposition Parameters

Table A.3.: Evaporator power supplies, deposition parameters and achieved Ru thicknesses for the experiments performed at the MATline and SXR endstations. Notice the big difference in deposition times and filament current needed between the evaporators in the two experiments to achieve similar thicknesses and deposition rates. This is most likely a product of unintensional variability in the evaporators being built, as well as the performance of their different power supplies.

Parameter	MATline	SXR (thin/thick)
Evaporator power supply	EGCO4	EBV40A-PS
Achieved Ru thickness [nm]	0.9	0.7/1.5
Deposition time [min]	20	15/30
Voltage [kV]	1.97	1.50
Filament current [A]	4.39	1.94
Emission current [mA]	32	32

A.4. XPS Scan Parameters

Table A.4.: The relevant scan parameters from the XPS measurements performed in March 2018 at the Soft X-ray (SXR) endstation of the Australian Synchrotron. All scans were done in fixed analyzer transmission mode using a PHOIBOS HSA3500 150 hemispherical analyzer at normal emission angle. E_p denotes the pass energy of the analyzer, and ΔE the energy step between each recorded intensity.

Figure	Region	Photon energy [eV]	E_p [eV]	Dwell time [s]	ΔE [eV]
5.1	Widescan	1254	20	0.1	0.2
5.2	O $1s$	590	5	0.1	0.05
5.2	C $1s$	345	5	0.1	0.05
5.2	Si $2p$	160	5	0.1	0.05
5.3	Widescan	1254	20	0.1	0.2
5.4	C $1s$, Ru $3d$	345	5	0.1	0.05
5.4	Si $2p$	160	5	0.1	0.05
5.6	C $1s$, Ru $3d$	345	5	0.1	0.05
5.6	Si $2p$	160	5	0.1	0.05
5.8	C $1s$, Ru $3d$	345	5	0.1	0.05
5.8	Si $2p$	160	5	0.1	0.05
5.9a	C $1s$, Ru $3d$	345	5	0.1	0.05
5.9a	C $1s$, Ru $3d$	465	5	0.1	0.05
5.9a	C $1s$, Ru $3d$	700	5	0.1	0.05
5.9a	C $1s$, Ru $3d$	1200	5	0.1	0.05
5.11	C $1s$, Ru $3d$	345	5	0.1	0.05
5.11	Si $2p$	160	5	0.1	0.05
5.15	O $1s$	590	5	0.1	0.05
5.15	C $1s$, Ru $3d$	345	5	0.1	0.05
5.16	C $1s$, Ru $3d$	345	5	0.1	0.05
5.16	C $1s$, Ru $3d$	345	5	0.1	0.05
5.16	Si $2p$	160	5	0.1	0.05
5.16	Si $2p$	160	5	0.1	0.05

A.5. NEXAFS Scan Parameters

Table A.5.: The relevant scan parameters from the NEXAFS measurements performed at the SXR. All scans were done in fixed analyzer mode using a hemispherical analyzer at normal emission angle. E_p denotes the pass energy of the analyzer, and ΔE the energy step between each recorded intensity. The full energy range for each scan has also been included.

Figure	Region	Photon energy range [eV]	E_p [eV]	ΔE [eV]
5.5	C $1s$, Ru $3d$	$375 - 320$	5	0.1
5.7	C $1s$, Ru $3d$	$375 - 320$	5	0.1
5.10a	C $1s$, Ru $3d$	$375 - 320$	5	0.1
5.12	C $1s$, Ru $3d$	$375 - 320$	5	0.1
5.13	C $1s$, Ru $3d$	$375 - 320$	5	0.1

Bibliography

[1] Kostya S Novoselov et al. "Electric field effect in atomically thin carbon films". In: *science* 306.5696 (2004), pp. 666–669.

[2] Michael Foxe et al. "Detection of ionizing radiation using graphene field effect transistors". In: *Nuclear Science Symposium Conference Record (NSS/MIC), 2009 IEEE*. IEEE. 2009, pp. 90–95.

[3] Neeraj Mishra et al. "Graphene growth on silicon carbide: A review". In: *physica status solidi (a)* 213.9 (2016), pp. 2277–2289.

[4] F Schedin et al. "Detection of individual gas molecules adsorbed on graphene". In: *Nature materials* 6.9 (2007), pp. 652–655.

[5] Michael Foxe et al. "Graphene field-effect transistors on undoped semiconductor substrates for radiation detection". In: *IEEE Transactions on Nanotechnology* 11.3 (2012), pp. 581–587.

[6] John C. Angus and Cliff C. Hayman. "Low-Pressure, Metastable Growth of Diamond and "Diamondlike" Phases". In: *Science* 241.4868 (Aug. 1988), p. 913.

[7] Arthur P. Ramirez. "Superconductivity in alkali-doped C60". In: *Physica C: Superconductivity and its Applications* 514.Supplement C (2015), pp. 166–172. ISSN: 0921-4534. DOI: `https://doi.org/10.1016/j.physc.2015.02.014`.

[8] C. Dupas and M. Lahmani. *Nanoscience: Nanotechnologies and Nanophysics*. Springer Berlin Heidelberg, 2007. ISBN: 9783540286172.

[9] Min-Feng Yu et al. "Strength and Breaking Mechanism of Multiwalled Carbon Nanotubes Under Tensile Load". In: *Science* 287.5453 (2000), pp. 637–640. ISSN: 0036-8075. DOI: `10.1126/science.287.5453.637`.

[10] Philip Richard Wallace. "The band theory of graphite". In: *Physical Review* 71.9 (1947), p. 622.

[11] IA Ovid'ko. "Mechanical properties of graphene". In: *Rev. Adv. Mater. Sci* 34.1 (2013), pp. 1–11.

[12] Alexander A Balandin. "Thermal properties of graphene and nanostructured carbon materials". In: *Nature materials* 10.8 (2011), pp. 569–581.

[13] J. N. Fuchs and M. O. Goerbig. "Introduction to the physical properties of graphene". In: *Lecture notes*. Jean-Nöel Fuchs and Mark Oliver Goerbig, 2008.

[14] G Grosso and G. P. P. Parravicini. *Solid State Physics*. Elsevier LTD, Oxford, 2013.

[15] D.J. Griffiths. *Introduction to Quantum Mechanics*. Cambridge University Press, 2016. ISBN: 9781107179868.

[16] Riichiro Saito, Gene Dresselhaus, and Mildred S Dresselhaus. *Physical properties of carbon nanotubes*. World Scientific, 1998.

[17] Mikhail I Katsnelson. "Graphene: carbon in two dimensions". In: *Materials today* 10.1 (2007), pp. 20–27.

[18] CWJ Beenakker. "Colloquium: Andreev reflection and Klein tunneling in graphene". In: *Reviews of Modern Physics* 80.4 (2008), p. 1337.

[19] Kirill I Bolotin et al. "Ultrahigh electron mobility in suspended graphene". In: *Solid State Communications* 146.9 (2008), pp. 351–355.

[20] E Pallecchi et al. "High Electron Mobility in Epitaxial Graphene on 4H-SiC (0001) via post-growth annealing under hydrogen". In: *Scientific reports* 4 (2014).

[21] EH Hwang and S Das Sarma. "Acoustic phonon scattering limited carrier mobility in two-dimensional extrinsic graphene". In: *Physical Review B* 77.11 (2008), p. 115449.

[22] C. Kittel. *Introduction to Solid State Physics*. Wiley, 2004. ISBN: 9780471415268.

[23] G.F. Knoll. *Radiation Detection and Measurement*. John Wiley & Sons, 2010. ISBN: 9780470131480.

[24] Yu-Ming Lin et al. "Dual-gate graphene FETs with $f\_\{T\}$ of 50 GHz". In: *IEEE Electron Device Letters* 31.1 (2010), pp. 68–70.

[25] Lei Liao et al. "High-speed graphene transistors with a self-aligned nanowire gate". In: *Nature* 467.7313 (2010), pp. 305–308.

[26] Choon-Ming Seah, Siang-Piao Chai, and Abdul Rahman Mohamed. "Mechanisms of graphene growth by chemical vapour deposition on transition metals". In: *Carbon* 70 (2014), pp. 1–21.

[27] Sukang Bae et al. "Roll-to-roll production of 30-inch graphene films for transparent electrodes". In: *Nature nanotechnology* 5.8 (2010), pp. 574–578.

[28] Ariel Ismach et al. "Direct chemical vapor deposition of graphene on dielectric surfaces". In: *Nano letters* 10.5 (2010), pp. 1542–1548.

[29] Hailong Zhou et al. "Chemical vapour deposition growth of large single crystals of monolayer and bilayer graphene". In: *Nature communications* 4 (2013).

[30] R.C. Jaeger, G.W. Neudeck, and R.F. Pierret. *Introduction to Microelectronic Fabrication*. 2nd ed. Vol. 5. Prentice Hall, 2002.

[31] Walt A De Heer et al. "Large area and structured epitaxial graphene produced by confinement controlled sublimation of silicon carbide". In: *Proceedings of the National Academy of Sciences* 108.41 (2011), pp. 16900–16905.

[32] Jiyang Fan and Paul K Chu. "General properties of bulk SiC". In: *Silicon Carbide Nanostructures*. Springer, 2014, pp. 7–114.

[33] François Varchon et al. "Electronic structure of epitaxial graphene layers on SiC: effect of the substrate". In: *Physical review letters* 99.12 (2007), p. 126805.

[34] Ming Ruan et al. "Epitaxial graphene on silicon carbide: Introduction to structured graphene". In: *MRS bulletin* 37.12 (2012), pp. 1138–1147.

[35] Nishtha Srivastava et al. "Comparison of graphene formation on C-face and Si-face SiC {0001} surfaces". In: *Physical Review B* 82.23 (2010), p. 235406.

[36] SP Cooil et al. "Iron-mediated growth of epitaxial graphene on SiC and diamond". In: *Carbon* 50.14 (2012), pp. 5099–5105.

[37] Zhen-Yu Juang et al. "Synthesis of graphene on silicon carbide substrates at low temperature". In: *Carbon* 47.8 (2009), pp. 2026–2031.

[38] Petr Macháč et al. "Graphene preparation by annealing of Co/SiC structure". In: *Applied Surface Science* 320 (2014), pp. 544–551.

[39] Cun Li et al. "Preparation of single-and few-layer graphene sheets using Co deposition on SiC substrate". In: *Journal of Nanomaterials* 2011 (2011), p. 44.

[40] Kinnock V Munthali et al. "Solid state reaction of ruthenium with 6H-SiC under vacuum annealing and the impact on the electrical performance of its Schottky contact for high temperature operating SiC-based diodes". In: *Brazilian Journal of Physics* 44.6 (2014), pp. 739–745.

[41] Silvano Lizzit et al. "Transfer-free electrical insulation of epitaxial graphene from its metal substrate". In: *Nano letters* 12.9 (2012), pp. 4503–4507.

[42] S Roy et al. "SIMS, RBS and glancing incidence X-ray diffraction studies of thermally annealed Ru/β-SiC interfaces". In: *Applied surface science* 211.1 (2003), pp. 300–307.

[43] Albert Einstein. "Über einen die Erzeugung und Verwandlung des Lichtes betreffenden heuristischen Gesichtspunkt". In: *Annalen der Physik* 322.6 (1905), pp. 132–148.

[44] MP Seah, IS Gilmore, and SJ Spencer. "XPS: binding energy calibration of electron spectrometers 4—assessment of effects for different x-ray sources, analyser resolutions, angles of emission and overall uncertainties". In: *Surface and interface analysis* 26.9 (1998), pp. 617–641.

[45] Andrea Damascelli. "Probing the electronic structure of complex systems by ARPES". In: *Physica Scripta* 2004.T109 (2004), p. 61.

[46] Stephan Hüfner. *Photoelectron Spectroscopy: Principles and Applications*. Springer Science & Business Media, 2013.

[47] D.S. Saxon. *Elementary Quantum Mechanics*. Dover books on physics. Dover Publications, Incorporated, 2012. ISBN: 9780486485966.

[48] P. Hofmann. *Surface Physics: An Introduction*. Philip Hofmann, 2013. ISBN: 9788799609031.

[49] Jens Als-Nielsen and Des McMorrow. *Elements of Modern X-ray Physics*. John Wiley & Sons, Inc., 2011. ISBN: 9781119998365. DOI: 10.1002/9781119998365.ch2.

[50] M Pl Seah and WA Dench. "Quantitative electron spectroscopy of surfaces: A standard data base for electron inelastic mean free paths in solids". In: *Surface and interface analysis* 1.1 (1979), pp. 2–11.

[51] JJ Yeh and I Lindau. "Atomic subshell photoionization cross sections and asymmetry parameters". In: *Atomic data and nuclear data tables* 32.1 (1985), pp. 1–155.

[52] JJ Yeh. *Atomic calculation of photoionization cross-sections and asymmetry parameters*. Gordon & Breach Science Publ.; AT&T Bell Laboratories, 1993.

[53] John F. Watts and John Wolstenholme. "The Electron Spectrum: Qualitative and Quantitative Interpretation". In: *An Introduction to Surface Analysis by XPS and AES*. John Wiley & Sons, Ltd, 2005, pp. 59–77. ISBN: 9780470867938. DOI: 10.1002/0470867930.ch3.

[54] Siegfried Hofmann. *Auger- and X-Ray Photoelectron Spectroscopy in Materials Science: A User-Oriented Guide*. Springer Berlin Heidelberg, 2013. ISBN: 978-3-642-27381-0.

[55] DP Woodruff, TA Delchar, and JE Rowe. "Modern Techniques of Surface Science". In: *Physics Today* 41 (1988), p. 90.

[56] Specs. *PHOIBOS hemispherical energy analyser series*. SPECS, 2008.

[57] J.J. Sakurai and J. Napolitano. *Modern Quantum Mechanics*. Addison-Wesley, 2011. ISBN: 9780805382914.

[58] F. Allegretti and P.S. Deimel. *Electron Spectroscopy of Surfaces: Elemental and Chemical Analysis with X-ray Photoelectron Spectroscopy*. Technical University of Munich. URL: https://www.ph.tum.de/academics/org/labs/fopra/docs/userguide-35.en.pdf.

[59] Martin Schmid, Hans-Peter Steinrück, and J Michael Gottfried. "A new asymmetric Pseudo-Voigt function for more efficient fitting of XPS lines". In: *Surface and Interface Analysis* 46.8 (2014), pp. 505–511.

[60] Eric W. Weisstein. *Full Width at Half Maximum*. URL: http://mathworld.wolfram.com/FullWidthatHalfMaximum.html (visited on 06/02/2018).

[61] B.D. Ratner and D.G Castner. "Electron Spectroscopy for Chemical Analysis". In: *Surface Analysis — The Principal Techniques*. Ed. by J.C. Vickerman. J. Wiley & Sons, Ltd., 1997. Chap. 4.

[62] P Thompson, DE Cox, and JB Hastings. "Rietveld refinement of Debye–Scherrer synchrotron X-ray data from Al2O3". In: *Journal of Applied Crystallography* 20.2 (1987), pp. 79–83.

[63] T Ida, M Ando, and H Toraya. "Extended pseudo-Voigt function for approximating the Voigt profile". In: *Journal of Applied Crystallography* 33.6 (2000), pp. 1311–1316.

[64] R Hesse, P Streubel, and R Szargan. "Product or sum: comparative tests of Voigt, and product or sum of Gaussian and Lorentzian functions in the fitting of synthetic Voigt-based X-ray photoelectron spectra". In: *Surface and Interface Analysis* 39.5 (2007), pp. 381–391.

[65] Sunjic Doniach and M Sunjic. "Many-electron singularity in X-ray photoemission and X-ray line spectra from metals". In: *Journal of Physics C: Solid State Physics* 3.2 (1970), p. 285.

[66] Gerald D Mahan. "Collective excitations in x-ray spectra of metals". In: *Physical Review B* 11.12 (1975), p. 4814.

[67] GK Wertheim and LR Walker. "Many-body effects in transition metals: role of the density of states". In: *Journal of Physics F: Metal Physics* 6.12 (1976), p. 2297.

[68]   D. A. Shirley. "High-Resolution X-Ray Photoemission Spectrum of the Valence Bands of Gold". In: *Phys. Rev. B* 5 (12 June 1972), pp. 4709–4714. DOI: `10.1103/PhysRevB.5.4709`.

[69]   A Herrera-Gomez et al. "Practical methods for background subtraction in photoemission spectra". In: *Surface and Interface Analysis* 46.10-11 (2014), pp. 897–905.

[70]   Joachim Stöhr. *NEXAFS spectroscopy*. Vol. 25. Springer Science & Business Media, 2013.

[71]   David Attwood and Anne Sakdinawat. *X-rays and extreme ultraviolet radiation: principles and applications*. Cambridge university press, 2017.

[72]   P. Atkins and J. de Paula. *Atkins' Physical Chemistry*. OUP Oxford, 2010. ISBN: 9780199543373.

[73]   D. Pacilé et al. "Near-Edge X-Ray Absorption Fine-Structure Investigation of Graphene". In: *Phys. Rev. Lett.* 101 (6 Aug. 2008), p. 066806. DOI: `10.1103/PhysRevLett.101.066806`.

[74]   Fei Song et al. "Direct measurement of electrical conductance through a self-assembled molecular layer". In: *Nature nanotechnology* 4.6 (2009), p. 373.

[75]   Georg Hahner. "Near edge X-ray absorption fine structure spectroscopy as a tool to probe electronic and structural properties of thin organic films and liquids". In: *Chem. Soc. Rev.* 35 (12 2006), pp. 1244–1255. DOI: `10.1039/B509853J`.

[76]   J. Stöhr and D. A. Outka. "Determination of molecular orientations on surfaces from the angular dependence of near-edge x-ray-absorption fine-structure spectra". In: *Phys. Rev. B* 36 (15 Nov. 1987), pp. 7891–7905. DOI: `10.1103/PhysRevB.36.7891`.

[77]   Manfred Otto Krause. "Atomic radiative and radiationless yields for K and L shells". In: *Journal of physical and chemical reference data* 8.2 (1979), pp. 307–327.

[78]   Philip Willmott. *An Introduction to Synchrotron Radiation: Techniques and Applications*. John Wiley & Sons, 2011.

[79]   Australian Synchrotron. *What is a Synchrotron?* 2018. URL: `http://www.synchrotron.org.au/synchrotron-science/what-is-a-synchrotron` (visited on 06/02/2018).

[80]   D.J. Griffiths. *Introduction to Electrodynamics*. Pearson Education, 2014. ISBN: 9780321972101.

[81]   Richard Phillips Feynman, Robert B Leighton, and Matthew Sands. *The Feynman Lectures on Physics, Vol. 2: Mainly Electromagnetism and Matter*. Addison-Wesley, 1979. Chap. 26.1–26.4.

[82]   K. J. Kim. "Characteristics of synchrotron radiation". In: *AIP Conf. Proc.* 184 (1989), pp. 565–632. DOI: `10.1063/1.38046`.

[83]   Joseph A Eichmeier and Manfred Thumm. *Vacuum electronics: components and devices*. Springer Science & Business Media, 2008.

[84]   Richard P Feynman, Robert B Leighton, and Matthew Sands. *The Feynman Lectures on Physics, Vol. I: Mainly Mechanics, Radiation, and Heat.* Vol. 1. Addison-Wesley, 1979. Chap. 43.

[85]   JW Matthews. *Epitaxial growth.* Elsevier, 2012.

[86]   JW Niemantsverdriet. *Concepts of modern catalysis and kinetics.* John Wiley & Sons, 2006.

[87]   Dorothy Hoffman, Bawa Singh, and John H Thomas III. *Handbook of vacuum science and technology.* Academic Press, 1997.

[88]   Nagamitsu Yoshimura. "Outgassing". In: *Vacuum Technology.* Springer, 2008, pp. 123–174.

[89]   Richard N. Tauber Stanley Wolf. *Silicon Processing for the VLSI Era: Process Technology.* 2nd. Vol. Vol. 1. Lattice Press, 1999. ISBN: 0961672161,9780961672164.

[90]   Werner Kern. "The evolution of silicon wafer cleaning technology". In: *Journal of the Electrochemical Society* 137.6 (1990), pp. 1887–1892.

[91]   T Takahagi et al. "The formation of hydrogen passivated silicon single-crystal surfaces using ultraviolet cleaning and HF etching". In: *Journal of applied physics* 64.7 (1988), pp. 3516–3521.

[92]   Geoffrey V Marr. *Handbook on Synchrotron Radiation: Vacuum Ultraviolet and Soft X-ray Processes.* Vol. 2. Elsevier, 2013.

[93]   DG McCulloch and R Brydson. "Carbon K-shell near-edge structure calculations for graphite using the multiple-scattering approach". In: *Journal of Physics: Condensed Matter* 8.21 (1996), p. 3835.

[94]   Ram P Gandhiraman et al. "X-ray absorption study of graphene oxide and transition metal oxide nanocomposites". In: *The Journal of Physical Chemistry C* 118.32 (2014), pp. 18706–18712.

[95]   C. D. Wanger et al. *Handbook of X-ray Photoelectron Spectroscopy.* Perkin-Elmer Corp., Physical Electronics Division, Eden Prairie, Minnesota, USA, 1979.

[96]   Eliot Gann et al. "*Quick AS NEXAFS Tool* (*QANT*): a program for NEXAFS loading and analysis developed at the Australian Synchrotron". In: *Journal of Synchrotron Radiation* 23.1 (Jan. 2016), pp. 374–380. DOI: 10.1107/S1600577515018688.

[97]   B Watts, L Thomsen, and PC Dastoor. "Methods in carbon K-edge NEXAFS: experiment and analysis". In: *Journal of Electron Spectroscopy and Related Phenomena* 151.2 (2006), pp. 105–120.

[98]   SI Raider, R Flitsch, and MJ Palmer. "Oxide growth on etched silicon in air at room temperature". In: *Journal of the Electrochemical Society* 122.3 (1975), pp. 413–418.

[99]   A Seubert et al. "In situ surface phases and silicon-adatom geometry of the (2×2) C structure on 6H-SiC $(000\bar{1})$". In: *Surface science* 454 (2000), pp. 45–48.

[100]   I. Forbeaux, J.-M. Themlin, and J.-M. Debever. "Heteroepitaxial graphite on $6H-$SiC(0001) : Interface formation through conduction-band electronic structure". In: *Phys. Rev. B* 58 (24 Dec. 1998), pp. 16396–16406. DOI: 10.1103/PhysRevB.58.16396.

[101]   U Starke and C Riedl. "Epitaxial graphene on SiC (0001) and: from surface reconstructions to carbon electronics". In: *Journal of Physics: Condensed Matter* 21.13 (2009), p. 134016.

[102]   Gian Carlo Capitani, Simonpietro Di Pierro, and Gioacchino Tempesta. "The 6 H-SiC structure model: Further refinement from SCXRD data from a terrestrial moissanite". In: *American Mineralogist* 92.2-3 (2007), pp. 403–407.

[103]   ZH Lu et al. "Photoemission studies of silicon on the Ru (001) surface". In: *Applied physics letters* 58.2 (1991), pp. 161–163.

[104]   E Rollings et al. "Synthesis and characterization of atomically thin graphite films on a silicon carbide substrate". In: *Journal of Physics and Chemistry of Solids* 67.9-10 (2006), pp. 2172–2177.

[105]   Guoting Qin et al. "Highly stable, protein resistant thin films on SiC-modified silicon substrates". In: *Chemical Communications* 46.19 (2010), pp. 3289–3291.

[106]   G Hollinger and FJ Himpsel. "Probing the transition layer at the SiO2-Si interface using core level photoemission". In: *Applied Physics Letters* 44.1 (1984), pp. 93–95.

[107]   Heiji Watanabe et al. "Synchrotron x-ray photoelectron spectroscopy study on thermally grown SiO2/4H-SiC (0001) interface and its correlation with electrical properties". In: *Applied Physics Letters* 99.2 (2011), p. 021907.

[108]   KV Emtsev et al. "Interaction, growth, and ordering of epitaxial graphene on SiC {0001} surfaces: A comparative photoelectron spectroscopy study". In: *Physical Review B* 77.15 (2008), p. 155303.

[109]   LI Johansson et al. "Electronic structure of 6H-SiC (0001)". In: *Physical Review B* 53.20 (1996), p. 13803.

[110]   L Simon et al. "X-ray spectroscopy of the oxidation of 6H-SiC (0001)". In: *Physical Review B* 60.8 (1999), p. 5673.

[111]   Ronald A Crowson et al. "Preparation of phosphate samples for oxygen isotope analysis". In: *Analytical chemistry* 63.20 (1991), pp. 2397–2400.

[112]   A Barrie and FJ Street. "An Auger and X-ray photoelectron spectroscopic study of sodium metal and sodium oxide". In: *Journal of Electron Spectroscopy and Related Phenomena* 7.1 (1975), pp. 1–31.

[113]   Gwyn P Williams. "X-ray data booklet". In: *X-ray data booklet* (2009).

[114]   David J Morgan. "Resolving ruthenium: XPS studies of common ruthenium materials". In: *Surface and Interface Analysis* 47.11 (2015), pp. 1072–1079.

[115]   Guangming Liu et al. "Electronic properties and interface characterization of phthalocyanine and Ru-polypyridine dyes on TiO2 surface". In: *Surface science* 539.1-3 (2003), pp. 37–48.

[116]   Bingyu Lin et al. "Effect of carbon and chlorine on the performance of carbon-covered alumina supported Ru catalyst for ammonia synthesis". In: *Catalysis Communications* 12.15 (2011), pp. 1452–1457.

[117]   Myriano H Oliveira Jr et al. "Formation of high-quality quasi-free-standing bilayer graphene on SiC (0 0 0 1) by oxygen intercalation upon annealing in air". In: *Carbon* 52 (2013), pp. 83–89.

[118] Masamichi Ogasawara et al. "Characterization and reactivity of an unprecedented unsaturated zero-valent ruthenium species: Isolable, yet highly reactive". In: *Journal of the American Chemical Society* 118.42 (1996), pp. 10189–10199.

[119] C Calandra, Olmes Bisi, and G Ottaviani. "Electronic properties on silicon-transition metal interface compounds". In: *Surface Science Reports* 4.5-6 (1985), pp. 271–364.

[120] Paul G Gassman and Charles H Winter. "Preparation, electrochemical oxidation, and XPS studies of unsymmetrical ruthenocenes bearing the pentamethylcyclopentadienyl ligand". In: *Journal of the American Chemical Society* 110.18 (1988), pp. 6130–6135.

[121] Luca Pasquali et al. "Formation and distribution of compounds at the Ru–Si (001) ultrathin film interface". In: *Journal of Applied Physics* 105.4 (2009), p. 044304.

[122] Ki-jeong Kim et al. "Temperature dependent structural changes of graphene layers on 6H-SiC (0001) surfaces". In: *Journal of Physics: Condensed Matter* 20.22 (2008), p. 225017.

[123] Emil V Jelenković et al. "XPS and TEM study of deposited and Ru–Si solid state reaction grown ruthenium silicides on silicon". In: *Materials Science in Semiconductor Processing* 40 (2015), pp. 817–821.

[124] YS Chang and ML Chou. "Formation and structure of epitaxial ruthenium silicides on (111) Si". In: *Journal of Applied Physics* 68.5 (1990), pp. 2411–2414.

[125] Ho Yeung H Chan, Christos G Takoudis, and Michael J Weaver. "High-pressure oxidation of ruthenium as probed by surface-enhanced Raman and X-ray photoelectron spectroscopies". In: *Journal of Catalysis* 172.2 (1997), pp. 336–345.

[126] NN Greenwood and A Earnshaw. *Chemistry of the Elements 2nd Edition*. Butterworth-Heinemann, 1997.

[127] Catherine Stampfl and Matthias Scheffler. "Theoretical study of O adlayers on Ru (0001)". In: *Physical Review B* 54.4 (1996), p. 2868.

[128] Sandip Niyogi et al. "Solution properties of graphite and graphene". In: *Journal of the American Chemical Society* 128.24 (2006), pp. 7720–7721.

[129] PL De Andres, Rafael Ramirez, and José A Vergés. "Strong covalent bonding between two graphene layers". In: *Physical Review B* 77.4 (2008), p. 045403.

[130] I Forbeaux, Jean-Marc Themlin, and J.-M Debever. "Heteroepitaxial graphite on 6H-SiC(0001): Interface formation through conduction-band electronic structure". In: 58 (Dec. 1998), pp. 1456495–16406.

[131] Taisuke Ohta et al. "Controlling the electronic structure of bilayer graphene". In: *Science* 313.5789 (2006), pp. 951–954.

[132] I Forbeaux, J-M Themlin, and J-M Debever. "Heteroepitaxial graphite on 6 H-SiC (0001): Interface formation through conduction-band electronic structure". In: *Physical Review B* 58.24 (1998), p. 16396.

[133] Shanshan Chen et al. "Oxidation resistance of graphene-coated Cu and Cu/Ni alloy". In: *ACS nano* 5.2 (2011), pp. 1321–1327.

[134] J Kikuma et al. "Surface analysis of CVD carbon using NEXAFS, XPS and TEM". In: *Journal of electron spectroscopy and related phenomena* 88 (1998), pp. 919–925.

[135]   V Pérez-Dieste et al. "Thermal decomposition of surfactant coatings on Co and Ni nanocrystals". In: *Applied physics letters* 83.24 (2003), pp. 5053–5055.

[136]   Rosanna Larciprete et al. "Oxygen switching of the epitaxial graphene–metal interaction". In: *Acs Nano* 6.11 (2012), pp. 9551–9558.

[137]   Baljit Singh et al. "Pt based nanocomposites (mono/bi/tri-metallic) decorated using different carbon supports for methanol electro-oxidation in acidic and basic media". In: *Nanoscale* 3.8 (2011), pp. 3334–3349.

[138]   Neeraj Dwivedi et al. "Understanding the role of nitrogen in plasma-assisted surface modification of magnetic recording media with and without ultrathin carbon overcoats". In: *Scientific reports* 5 (2015), p. 7772.

[139]   Andrea C Ferrari. "Raman spectroscopy of graphene and graphite: disorder, electron–phonon coupling, doping and nonadiabatic effects". In: *Solid state communications* 143.1 (2007), pp. 47–57.

[140]   LM Malard et al. "Raman spectroscopy in graphene". In: *Physics Reports* 473.5 (2009), pp. 51–87.

[141]   J Röhrl et al. "Raman spectra of epitaxial graphene on SiC (0001)". In: *Applied Physics Letters* 92.20 (2008), p. 201918.

[142]   S Yi Zhou et al. "Substrate-induced bandgap opening in epitaxial graphene". In: *Nature materials* 6.10 (2007), p. 770.

[143]   SY Zhou et al. "Metal to insulator transition in epitaxial graphene induced by molecular doping". In: *Physical review letters* 101.8 (2008), p. 086402.